



TECHNISCHE  
UNIVERSITÄT  
WIEN  
Vienna | Austria

DIPLOMARBEIT

DEVELOPMENT OF A SPIN CHOPPING SYSTEM  
FOR THE NEUTRON SPIN ECHO  
INTERFEROMETER AT THE ATOMINSTITUT'S  
WHITE BEAMLIN

zur Erlangung des akademischen Grades

Diplom-Ingenieur

im Rahmen des Studiums

Technische Physik

eingereicht von

Simon Hack

Matrikelnummer 01425322

ausgeführt am Atominstitut  
der Fakultät für Physik der Technischen Universität Wien

Betreuung

Betreuer: Privatdoz. Dipl.-Ing. Dr. Stephan Sponar

Mitwirkung: Ass.-Prof. Dipl.-Ing. Dr. Yuji Hasegawa

Mitwirkung: Niels Geerits, M.Sc.

---

Ort, Datum

---

Simon Hack

---

Stephan Sponar





## Abstract

This thesis focuses on the design, implementation and testing of two different approaches towards broadband neutron spin flipping to be applied in a spin echo small angle neutron scattering instrument. The first approach utilises time dependent amplitudes of an oscillating magnetic field, but requires a pulsed beam, which in this case was realized by spin chopping. Time-of-flight measurements showed that the resulting pulsed beam had a low signal-to-noise ratio and thus this approach was not followed up. For the second approach a pulsed beam is not required and the neutron spin is flipped with an adiabatic radio frequency (RF) flipper. On the one hand this device is capable of achieving high flip efficiencies for a broad range of neutron wavelengths, but on the other hand has high electrical power requirements. Measurements of the flip efficiency of a single flipper yielded a maximum of  $\epsilon = 0.9231(15)$  at an RF frequency  $f = 1$  MHz. Primarily, the performance was limited by heat generated in the RF flipper and cables, which may be counteracted by a special cooling system.

## Kurzzusammenfassung

Das Design, die Implementierung und das Testen von zwei verschiedenen Ansätzen für breitbandiges Neutronenspinflipping, die in einem Spin-Echo-Kleinwinkelstreuungsinstrument angewendet werden sollen, wurden in dieser Diplomarbeit untersucht. Der erste Ansatz nutzt zeitabhängige Amplituden des oszillierenden Magnetfeldes, erfordert jedoch einen gepulsten Strahl, der in diesem Fall durch ein Spin-Choppingsystem erzeugt wird. Flugzeitmessungen ergaben, dass der resultierende gepulste Strahl nur ein geringes Signal-Rausch-Verhältnis aufweist, weshalb dieser Ansatz nicht weiterverfolgt wurde. Für den zweiten Ansatz wird kein gepulster Strahl benötigt und der Neutronenspin wird mit Hilfe eines adiabatischen Flippers im Hochfrequenzbereich (RF) geflippt. Mit dieser Methode lassen sich einerseits hohe Flip-Effizienzen für einen breiten Bereich von Neutronenwellenlängen erzielen, andererseits ist jedoch der elektrische Leistungsbedarf sehr hoch. Messungen der Flip-Effizienz eines einzelnen Flippers ergaben einen Maximalwert von  $\epsilon = 0,9231(15)$  bei einer RF-Frequenz von  $f = 1$  MHz. In erster Linie wurde die Leistungsfähigkeit durch die im RF-Flipper und in den Kabeln erzeugte Wärme beschränkt. Dem kann man mit einem speziellen Kühlsystem entgegenwirken.

# Contents

<b>1</b>	<b>Introduction</b>	<b>8</b>
<b>2</b>	<b>Neutron Optics</b>	<b>10</b>
2.1	Properties of Neutrons . . . . .	10
2.2	Neutrons in Magnetic Fields . . . . .	11
2.2.1	Geometric Frequency and Adiabaticity Parameter . . . . .	17
2.3	Neutron Spin Flipper . . . . .	17
2.3.1	Adiabatic Static Spin Rotators . . . . .	18
2.3.2	Resonant RF Spin Flipper . . . . .	18
2.3.3	Adiabatic RF Spin Flipper . . . . .	23
2.3.4	Time Dependent RF Amplitude . . . . .	27
2.4	Reflection and Supermirrors . . . . .	28
2.5	Neutron Source and Counting Statistics . . . . .	30
2.6	Detector . . . . .	33
<b>3</b>	<b>Spin Echo</b>	<b>34</b>
3.1	Neutron Spin Echo (NSE) . . . . .	34
3.1.1	Classical Model: Larmor Precession . . . . .	34
3.1.2	Semi-Classical Approach . . . . .	37
3.2	Neutron Resonant Spin Echo (NRSE) . . . . .	40
3.2.1	Semi Classical Approach . . . . .	43
3.3	Spin Echo Small Angle Neutron Scattering (SESANS) . . . . .	45
3.3.1	Semi-Classical Approach . . . . .	48
<b>4</b>	<b>Spin Chopping System</b>	<b>51</b>
4.1	Experimental Setup and Preparation . . . . .	51
4.2	Results . . . . .	59
4.3	Discussion . . . . .	64
<b>5</b>	<b>Development of an adiabatic RF spin flipper coil</b>	<b>66</b>
5.1	Experimental Setup and Preparation . . . . .	66
5.2	Results . . . . .	78

5.3 Discussion . . . . .	85
<b>6 Outlook</b>	<b>87</b>
<b>7 Conclusion</b>	<b>89</b>





# Chapter 1

## Introduction

Since neutrons are spin- $\frac{1}{2}$  particles they possess a magnetic moment, which can couple to a magnetic field. This coupling results in Larmor precession, which is exploited at a neutron spin echo spectrometer (NSE). If a polarized polychromatic neutron beam passes through a magnetic field region, the neutrons exhibit different precession angles by the end of the field region depending on their velocity. These can be viewed as individual clocks, keeping track of the time period each neutron spends inside the magnetic field. By adding a second field of same strength but in opposing direction all spins counterrotate and the initial polarization is restored. In case of a scattering experiment, a sample is placed between the field regions. With this aforementioned method of time-keeping, spin echo instruments are capable of determining small energy changes during inelastic scattering processes by measuring the polarization of the scattered beam.

The concept of spin echo with polarized neutrons (NSE) was first proposed by Mezei in 1972 [Mez72]. The Larmor angle of the precession and furthermore the energy resolution are enhanced by the length of the region and the strength of the field. Additionally, the resolution is not limited by the wavelength spread of the incoming beam. Another unique feature of an NSE is the fact that the measured signal is already proportional to the Fourier transform of the scattering function, the so-called intermediate scattering function  $F(\vec{q}, \tau)$ , where  $\vec{q}$  is the momentum transfer and  $\tau$  the spin echo time. Latter quantity also describes the maximal time difference two physical states of the scatter can still be correlated by an NSE. In 1987 Gähler and Golub generalised this method to a more sophisticated neutron spectrometer [GG87]. At a neutron resonant spin echo (NRSE) instrument, Larmor precession is replaced by zero field precession induced by dynamical magnetic resonant RF flipper. In this case the spin of a neutron is rotated by absorption or emission of a photon from the oscillating RF field. This process changes the total energy of the neutron and leads to zero field precession, a precession of the spin in a region of zero magnetic field. The combination of small angle neutron scattering and spin echo (SESANS) was contrived by Rekveldt in 1996 [Rek96]. At these instruments the measured signal is also sensitive to a momentum transfer  $\vec{q}$  from the

neutrons to the scatterer. This is achieved by tilted magnetic field regions with respect to the beam direction. This has the consequence that the neutrons' path length within the field and the precession angle at the end of the field range become dependent on the momentum change, thus influencing the measured polarization. Furthermore, the semi-classical description of a SESANS instrument highlights the spatial splitting of the spin eigenstates perpendicular to the beam, enabling manipulation of only one state similar to an interferometer experiment. Moreover, the momentum transfer resolution is not limited by the beam divergence. At the white neutron beam line at the Atominstitut (ATI) in Vienna a SESANS instrument utilizing zero field precession is currently being developed.

The thesis is divided into four chapters. The first one is about the theory of neutron optics more particularly the interaction of the neutron spin with static and time dependent magnetic fields and how this interaction can be used to manipulate the spin. The second chapter is a theoretical description of the spin echo phenomenon, with the goal to provide the knowledge for understanding NSE, NRSE and SESANS and the experimental setup at the ATI white beam line. In addition, it will also investigate the trajectories of the individual spin eigenstates through the instrument to gain deeper insight into the topic. The third chapter discusses the first experimental approach of spin chopping. The setup is described from both an electrical engineering and a neutron optical point of view. The recorded TOF spectra are presented and analysed. The fourth chapter deals with the second experimental approach, where an adiabatic RF flipper was used to flip the neutron spin. First, the experimental prerequisite is discussed, followed by the experimental data from which the flip efficiency was calculated. For different setups the changes in efficiency were compared. Finally, a short outlook on the further procedure is given. It discusses possibilities to ensure long-term operation and how to increase the flip efficiency of the adiabatic RF flipper further.

## Chapter 2

# Neutron Optics

### 2.1 Properties of Neutrons

The neutron was discovered by James Chadwick in 1932 [Cha32]. It is part of the atoms nucleus, thus subjected to all four fundamental forces and carries no electric charge, explaining its name. Even though high precision measurements to find limits on the neutron electric dipole moment (nEDM) is an ongoing research field (e.g. [Bak+11]). Nowadays we even know the neutrons subatomic structure, which is made up of two down quarks and one up quark. Neutrons are also subjected to the weak force leading to a half-life time for free neutrons (i.e neutrons not bound in a nucleus) of  $\tau = 890 \text{ s} \approx 15 \text{ min}$ , after which it decays into a proton, an electron and an electron antineutrino. Furthermore neutrons are fermions, carrying spin- $\frac{1}{2}$ . A magnetic moment  $\mu_n$  is coupled to the neutrons spin with a magnitude of  $\mu_n = -1.913 \mu_N$ , where  $\mu_N = 5.051 \times 10^{-27} \text{ J/T}$  is the nuclear magneton. Additionally, the gyromagnetic ratio  $\gamma = \frac{2\mu}{\hbar}$  ( $\gamma = 1.83011 \times 10^8 \text{ T/s}$ ) is often used to describe the ratio between the magnetic moment and the spin of the neutron. This shows that neutrons can interact with magnetic fields. Moreover spin manipulations induced by static and/or time dependent magnetic fields are possible and will be discussed in detail in section 2.2.

Finally, neutrons have a mass of  $m = 1.6275 \cdot 10^{-27} \text{ kg}$  and are therefore subjected to gravity, which forces the neutron on a slightly curved trajectory through an typical neutron experimental setup. The effects of gravity and the free neutron lifetime can be neglected in most neutron experiments, especially at the white beam setup in Vienna. Louis de Broglie proposed in 1923 that it is possible assign wave character to all matter particles. With his famous relation

$$\lambda = \frac{h}{p} = \frac{h}{mv} = \frac{h}{\sqrt{2mE_{kin}}} \quad (2.1)$$

with  $\lambda$  the wavelength of the particle,  $h$  the Planck constant,  $p$  the momentum,  $v$  the group velocity and  $E_{kin}$  the kinetic energy. This wave behaviour also gives rise to the expression *Neutron Optics*. One can categorize neutrons according to their energy

	energy [eV]	wavelength [Å]	velocity [m/s]
ultra cold	$< 10^{-5}$	$> 92$	$> 44$
cold	$10^{-5} - 10^{-3}$	$92 - 9.2$	$44 - 443$
thermal	$10^{-3} - 0.5$	$9.2 - 0.4$	$443 - 10^4$
hot	$> 0.5$	$< 0.4$	$> 10^4$

Table 2.1: Classification of neutrons according to their energy. Neutrons at the white beam line Vienna ATI are thermal.

and wavelength, see table (2.1). Thermal neutrons have energies in the order of the thermal energy at room temperature ( $T \approx 300$  K), thus the name of the category.

## 2.2 Neutrons in Magnetic Fields

To describe the dynamics of a neutron in a magnetic field, we start from the Schrödinger equation

$$i\hbar \frac{\partial}{\partial t} \psi = \hat{H} \psi \quad (2.2)$$

where the derivative in time is proportional to the Hamiltonian  $\hat{H}$  of the system, with  $i$  being the imaginary unit,  $\hbar$  the reduced Planck constant and  $\psi$  the wavefunction describing the quantum state of the neutron. In presence of an external magnetic field  $\vec{B}(\vec{x}, t)$ , which can vary spatially and temporally, the Hamiltonian looks like [Mez88]

$$\hat{H} = -\frac{\hbar^2}{2m} \Delta - \hat{\vec{\mu}} \cdot \vec{B}(\vec{x}, t) \quad (2.3)$$

The first term describes the kinetic energy ( $m$  is the mass of the neutron and  $\Delta$  the Laplace operator) whereas the second term is corresponding to the potential energy of the neutron inside a magnetic field (and neglecting gravity). Here  $\hat{\vec{\mu}}$  is the vector operator of the magnetic moment of the neutron given by  $\hat{\vec{\mu}} = \mu \vec{\sigma} = \gamma \frac{\hbar}{2} \vec{\sigma}$  [Kra04] and  $\vec{\sigma}$  is the Pauli spin vector operator consisting of all three Pauli matrices,  $\vec{\sigma} = (\sigma_x, \sigma_y, \sigma_z)^T$ . The Pauli spin matrices in the  $\sigma_z$  eigenbasis are expressed as

$$\sigma_x = \begin{pmatrix} 0 & 1 \\ 1 & 0 \end{pmatrix}, \quad \sigma_y = \begin{pmatrix} 0 & -i \\ i & 0 \end{pmatrix}, \quad \sigma_z = \begin{pmatrix} 1 & 0 \\ 0 & -1 \end{pmatrix} \quad (2.4)$$

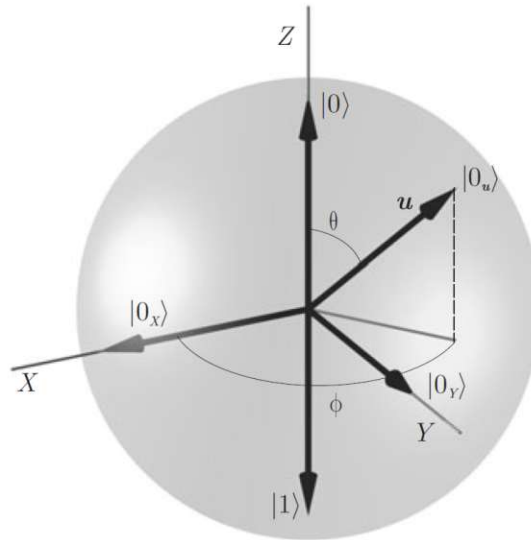


Figure 2.1: Bloch sphere representation of a qubit system, in this case of a spinor of a spin- $\frac{1}{2}$  particle. The south and the north poles correspond to the up-state  $|\uparrow\rangle = |1\rangle$  and the down-state  $|\downarrow\rangle = |0\rangle$ , respectively. Pure states lie on the surface of the sphere, whereas mixed states are lying inside. The angles  $\theta$  and  $\phi$  are given as in equation (2.6) and define an arbitrary pure state  $|0_u\rangle$ . The states  $|0_x\rangle$  and  $|0_y\rangle$  are superposition of  $|0\rangle$  and  $|1\rangle$ . From [HR06].

It follows that the nonrelativistic Schrödinger equation for a neutral spin- $\frac{1}{2}$  particle (also called Pauli equation for neutral particles) is given by

$$i\hbar \frac{\partial}{\partial t} \psi(\vec{x}, t) = \left[ -\frac{\hbar^2}{2m} \Delta - \gamma \frac{\hbar}{2} \vec{\sigma} \cdot \vec{B}(\vec{x}, t) \right] \psi(\vec{x}, t) \quad (2.5)$$

The state vector

$$\psi(\vec{x}, t) = \begin{pmatrix} \psi^+(\vec{x}, t) \\ \psi^-(\vec{x}, t) \end{pmatrix} = \Phi(\vec{r}, t) |S\rangle = f_+(\vec{r}, t) \cos\left(\frac{\theta}{2}\right) |\uparrow\rangle + f_-(\vec{r}, t) e^{i\phi} \sin\left(\frac{\theta}{2}\right) |\downarrow\rangle \quad (2.6)$$

is a two component spinor wave function, with  $f_+(\vec{r}, t)$  and  $f_-(\vec{r}, t)$  being the spatial wave function,  $|\uparrow\rangle$  and  $|\downarrow\rangle$  the spin eigenstates and  $\theta$  and  $\phi$  the polar and azimuthal angle of the spin vector respectively. The spin state  $|S\rangle$  is often represented on a Bloch sphere as depicted in figure (2.1).

The value of the potential energy term in equation (2.5) is not only given by the magnitude of the magnetic field, but also depends on the relative direction of the spin of the neutron with respect to the magnetic field (scalar product between  $\vec{\mu}$  and  $\vec{B}$ ). In the semi-classical picture of Larmor precession we think of the spin as a vector. So if the spin is parallel to the  $\vec{B}$ -field the potential energy decreases (due to the minus sign) and increases if the spin is antiparallel to  $\vec{B}$ . If they are orthogonal to each other the neutron does not experience any potential. In a more quantum mechanical picture one can say that the two spin states gain different potential energy (Zeeman splitting).

This consideration becomes important when it comes to the description of spin echo and zero field precession (section 3.2).

### Dynamics of Spinor $|S\rangle$

For a spatially independent magnetic field it is possible to write down an ansatz to equation (2.5) by

$$\psi(\vec{r}, t) = e^{i\vec{k}\vec{r} - i\omega t} |S(t)\rangle \quad (2.7)$$

Plugging this back into the Pauli equation one finds for the left hand side

$$i\hbar \frac{\partial}{\partial t} \psi(\vec{x}, t) = i\hbar \frac{\partial}{\partial t} e^{i\vec{k}\vec{r} - i\omega t} |S(t)\rangle = \hbar\omega e^{i\vec{k}\vec{r} - i\omega t} |S(t)\rangle + e^{i\vec{k}\vec{r} - i\omega t} i\hbar \frac{\partial}{\partial t} |S(t)\rangle \quad (2.8)$$

and for the right hand side

$$\left[ -\frac{\hbar^2}{2m} \Delta - \gamma \frac{\hbar}{2} \vec{\sigma} \cdot \vec{B}(t) \right] \psi(\vec{x}, t) = \frac{\hbar^2}{2m} k^2 e^{i\vec{k}\vec{r} - i\omega t} |S(t)\rangle - e^{i\vec{k}\vec{r} - i\omega t} \gamma \frac{\hbar}{2} \vec{\sigma} \cdot \vec{B}(t) |S(t)\rangle \quad (2.9)$$

Both sides must be equal thus leading to

$$\frac{\partial}{\partial t} |S(t)\rangle = \frac{1}{2} i\gamma \vec{\sigma} \cdot \vec{B}(t) |S(t)\rangle \quad (2.10)$$

where we used the fact that the kinetic energy of the neutron is  $\hbar\omega = \frac{\hbar^2 k^2}{2m}$ . This equation is called the Larmor equation and governs the time evolution of the 2-dimensional spinor wave function  $|S(t)\rangle$ . For a constant field  $\vec{B}$  (not explicitly time dependent) we find the the well known solution

$$|S(t)\rangle = e^{\frac{1}{2} i\gamma \vec{\sigma} \cdot \vec{B} t} |S(0)\rangle \quad (2.11)$$

The unitary operator  $U = e^{\frac{1}{2} i\gamma \vec{\sigma} \cdot \vec{B} t}$  describes a rotation around the direction of  $\vec{B}$  in the 2-dimensional complex space of the spinors over an angle  $\alpha = \gamma B t$  ( $B = |\vec{B}|$ ) with frequency  $\omega_L = \gamma B$ . This is the so-called Larmor frequency, which we will also encounter for the dynamics of the polarization. Using group theory language one says that  $U$  is forming the special unitary group  $SU(2)$  and that the Pauli matrices are the so-called generators of these transformations.  $SU(2)$  is the group of unitary  $2 \times 2$  matrices with determinate equal to 1.

## Polarization in experiment

The white beam line in Vienna is utilising polarized neutrons. The polarization of a neutron beam is defined as

$$\vec{P} = \begin{pmatrix} \langle \sigma_x \rangle \\ \langle \sigma_y \rangle \\ \langle \sigma_z \rangle \end{pmatrix} \quad (2.12)$$

It is the vector of the expectation values of the Pauli spin matrices. In general, only one component of the polarization vector is of interest. If we assume that the beam is initially fully polarized in  $z$ -direction (mostly chosen such that  $z$  is the direction of guide field i.e.  $\vec{B}_0$ ) we can write the  $z$ -component as

$$P_z = \langle \sigma_z \rangle = \langle S | \sigma_z | S \rangle = \langle S | \Pi_z^+ | S \rangle - \langle S | \Pi_z^- | S \rangle \quad (2.13)$$

where we split the  $\sigma_z$  operator into the two projection operators  $\Pi_z^+$  and  $\Pi_z^-$  which are projecting on the spin eigenstates  $|\uparrow\rangle$  and  $|\downarrow\rangle$  respectively. These projection operators can be linked to the measured intensities in an experiment. We can write them as  $\langle S | \Pi_z^+ | S \rangle = \frac{I_z^+}{I_z^+ + I_z^-}$  and  $\langle S | \Pi_z^- | S \rangle = \frac{I_z^-}{I_z^+ + I_z^-}$ , allowing us to rewrite equation (2.13) as

$$P_z = \frac{I_z^+ - I_z^-}{I_z^+ + I_z^-} \quad (2.14)$$

The Intensities  $I_z^+$  and  $I_z^-$  correspond to the expectation values of the projectors  $\Pi_z^+$  and  $\Pi_z^-$  respectively and are also associated with the maximal and minimal counts at a spin flipping measurement. Consequently enabling experimental access to the quantity  $P_z$ , which is a real number between  $-1$  and  $1$ . In interferometry experiments the contrast and the visibility are calculated in the same way.

A different quantity is the degree of polarization  $P$  which defined as the length of the polarization vector  $P = |\vec{P}|$

$$P = |\vec{P}| = \sqrt{\langle \sigma_x \rangle^2 + \langle \sigma_y \rangle^2 + \langle \sigma_z \rangle^2} \quad (2.15)$$

The degree of polarization has a value range between  $0$  and  $1$ , where  $0$  is describing a totally mixed state and  $1$  a pure state.

### Dynamics of Polarization $\langle \vec{\sigma} \rangle$

The polarization of a neutron beam is defined as the expectation value of the Pauli vector operator. If the neutron beam is perfectly polarized ( $P = 1$ ) one can assume a pure state for the beam thus one can write  $\vec{P} = \langle \psi(\vec{x}, t) | \vec{\sigma} | \psi(\vec{x}, t) \rangle = \langle S(t) | \vec{\sigma} | S(t) \rangle = \langle \vec{\sigma} \rangle$ . Otherwise the beam is described as a mixed state  $\rho$  and the polarization is given by  $\vec{P} = \text{Tr}(\rho \vec{\sigma})$ .

To calculate the dynamics of the polarization vector  $\vec{P} = \langle \vec{\sigma} \rangle$  in the presence of a magnetic field, we assume the Hamiltonian given in equation (2.5) and start from the Heisenberg equation for observables given by (e.g. [Sch07])

$$\frac{d}{dt} \langle \vec{\sigma} \rangle = \frac{i}{\hbar} \langle [H, \vec{\sigma}] \rangle + \left\langle \frac{\partial \vec{\sigma}}{\partial t} \right\rangle \quad (2.16)$$

where the term in the squared brackets denotes the commutator between the Hamiltonian  $H$  and the polarization. Since  $\langle \vec{\sigma} \rangle$  is not explicitly time dependent the last term in equation (2.16) is equal to zero. Additionally, the kinetic energy part of the Hamiltonian commutes with  $\vec{\sigma}$ . Therefore we are only left with  $\frac{d}{dt} \langle \vec{\sigma} \rangle = -\frac{\gamma}{2} i \langle [\vec{\sigma} \cdot \vec{B}, \vec{\sigma}] \rangle$ . To calculate this expression we make use of the fact that one can look at the commutator of two vectors (or a vector  $\vec{\sigma}$  and a scalar  $\vec{\sigma} \cdot \vec{B}$ ) componentwise and use the relation  $[\sigma_i, \sigma_j] = 2i\epsilon_{ijk}\sigma_k$  which assigns the commutator of two Pauli matrices to the third one, with  $\epsilon_{ijk}$  being the Levi-Civita symbol.

$$[\vec{\sigma} \cdot \vec{B}, \vec{\sigma}]_x = B_x[\sigma_x, \sigma_x] + B_y[\sigma_y, \sigma_x] + B_z[\sigma_z, \sigma_x] = B_y 2i(-\sigma_z) + B_z 2i\sigma_y \quad (2.17)$$

$$[\vec{\sigma} \cdot \vec{B}, \vec{\sigma}]_y = B_x 2i\sigma_z + B_z 2i(-\sigma_x) \quad (2.18)$$

$$[\vec{\sigma} \cdot \vec{B}, \vec{\sigma}]_z = B_x 2i(-\sigma_y) + B_y 2i\sigma_x \quad (2.19)$$

One can write the commutator of all three components much more elegantly as the cross product between  $\vec{B}$  and  $\vec{\sigma}$ ,  $[\vec{\sigma} \cdot \vec{B}, \vec{\sigma}] = 2i(\vec{\sigma} \times \vec{B})$ . If we insert this back into (2.16) we get

$$\frac{d}{dt} \langle \vec{\sigma} \rangle = -\frac{\gamma}{2} i \langle [\vec{\sigma} \cdot \vec{B}, \vec{\sigma}] \rangle = \gamma \langle \vec{\sigma} \times \vec{B} \rangle \quad (2.20)$$

If the magnetic field is purely time-dependent (i.e. perfectly homogeneous at every given point in time) one can write  $\gamma \langle \vec{\sigma} \times \vec{B} \rangle = \gamma \langle \vec{\sigma} \rangle \times \vec{B}$ . The equation of motion can be written as

$$\frac{d}{dt} \langle \vec{\sigma} \rangle = \gamma \langle \vec{\sigma} \rangle \times \vec{B} \quad (2.21)$$

This is the well-known Bloch equation which describes the motion of an classical magnetic moment in an external magnetic field. The change in time of the polarization  $\langle \vec{\sigma} \rangle = \vec{P}$  is orthogonal to  $\vec{P}$  and  $\vec{B}$  causing the polarization vector to precess around the magnetic field direction while preserving its length as well as the angle between  $\vec{B}$  and  $\vec{P}$ . This precession is called Larmor precession and is illustrated in figure (2.2).

Any 3-dimensional vector cross product can be rewritten with the help of the angular momentum operators  $\vec{L} = (L_x, L_y, L_z)$ . One can write  $\vec{a} \times \vec{b} = i(\vec{L} \cdot \vec{b})\vec{a}$  [LT08]. Additionally, the matrices  $\vec{L}$  are exactly the generators of the  $3 \times 3$  rotation matrices  $R$  in 3-dimensional euclidean space [Bal90] (i.e. the special orthogonal group  $SO(3)$ ). In adjoint representation the angular momentum operators look like



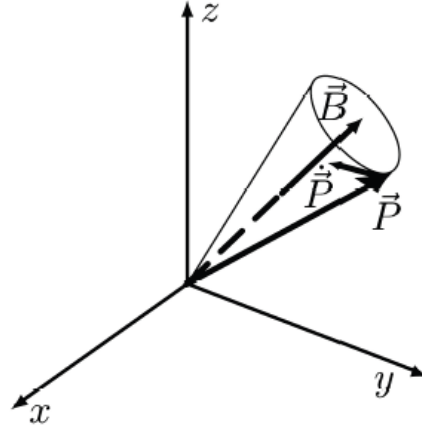


Figure 2.2: The time derivative of the polarization vector  $\dot{\vec{P}}$  is orthogonal to the polarization vector  $\vec{P} = \langle \vec{\sigma} \rangle$  and the magnetic field  $\vec{B}$  thus causing a precession around the direction of  $\vec{B}$ .

$$L_x = \begin{pmatrix} 0 & 0 & 0 \\ 0 & 0 & -i \\ 0 & i & 0 \end{pmatrix} L_y = \begin{pmatrix} 0 & 0 & i \\ 0 & 0 & 0 \\ -i & 0 & 0 \end{pmatrix} L_z = \begin{pmatrix} 0 & -i & 0 \\ i & 0 & 0 \\ 0 & 0 & 0 \end{pmatrix} \quad (2.22)$$

This yields for the Larmor equation

$$\frac{d}{dt} \langle \vec{\sigma} \rangle = i\gamma \vec{L} \cdot \vec{B}(t) \langle \vec{\sigma} \rangle \quad (2.23)$$

One immediately sees the close relation to equation (2.10). If  $\vec{L}$  is substituted with  $\frac{\hbar}{2}$  we arrive at the Larmor equation for spinors. The factor  $1/2$  gives rise to the quantum phenomenon of  $4\pi$  symmetry of spinors, that is  $\psi(0) = \psi(4\pi)$ . The "classical" polarization vector  $\vec{P}$ , on the other hand, obeys ordinary rotation rules and shows a standard  $2\pi$  symmetry  $\vec{P}(0) = \vec{P}(2\pi)$  [RW15]. A solution to equation (2.23) can be found in the same manner as for the spinor case (i.e. for constant  $\vec{B}$ )

$$\vec{P}(t) = \langle \vec{\sigma} \rangle (t) = e^{i\gamma \vec{L} \cdot \vec{B} t} \vec{P}(0) \quad (2.24)$$

The exponential function  $R = e^{i\gamma \vec{L} \cdot \vec{B} t}$  again describes a rotation around  $\vec{B}$  about an angle of  $\alpha = \gamma B t$  hence with a frequency  $\omega_L = \gamma B$  which is the Larmor frequency, the same as for spinors. It is the frequency with which the polarization vector precesses around  $\vec{B}$  and  $t$  being the time the neutron is exposed to the magnetic field. This time is almost always proportional to the velocity  $v$  of the neutron and the length of the magnetic field region  $L$  as the neutron flies through the experimental setup ,  $t = \frac{L}{v}$ . This precession enables spin manipulations with so-called DC spin rotators, where DC stands for direct current generating a static magnetic field. If the strength of the magnetic field and the length of the field region is adjusted correctly one can achieve a  $\pi$  flip meaning

that  $\alpha = \pi$ . Unfortunately this method does not work for a white neutron beam, since the precession angle depends on the velocity of the neutrons, leading to depolarization of the neutron beam. Nevertheless, DC-rotators are commonly used at monochromatic beamlines.

### 2.2.1 Geometric Frequency and Adiabaticity Parameter

We will briefly discuss the effects and consequences of a varying quantisation axis on the polarization vector. This is associated with a magnetic field  $\vec{B} = \vec{B}(\vec{x}, t)$ , which is dependent on time (e.g. rotating field in time) and/or space, i.e. it changes its orientation along the flight path of the beam. To describe the dynamics of the polarization qualitatively it is of use to define the adiabaticity parameter  $k$  as the ratio of the Larmor frequency  $\omega_L = \gamma B$  to the frequency  $\omega_f$  with which the field changes [Pl09]

$$k = \frac{\omega_L}{\omega_f} \quad (2.25)$$

For a pure time dependent and rotating field  $\vec{B}(t) = e^{iL_z \omega t} B$ ,  $\omega_f$  is simply the rotation frequency of the field ( $\omega_f = \omega$ ). For a pure space dependent field,  $\omega_f$  is equal to the geometric rotation frequency  $\omega_g$  (see also adiabatic RF flipper 2.3.3). It is defined as

$$\omega_f = \omega_g = \frac{d\alpha_g}{dt} = \frac{d\alpha_g}{dx} v \quad (2.26)$$

where  $\alpha_g$  is the geometric rotation angle, describing the angle between the magnetic field at the initial position  $\vec{B}(\vec{x} = \vec{0})$  and the field at position  $x$ , which is  $\vec{B}(\vec{x})$ . Then  $\omega_g$  determines how fast the neutron experiences the change of the external magnetic field. Its value increases the faster the neutrons, contrary to the adiabaticity parameter  $k$ , which decreases with neutron velocity. With the help of  $k$  we can describe three qualitatively different situations of the motion of polarization.

If  $k \gg 1$ , the polarization vector can follow the field and the angle between  $\vec{B}$  and  $\vec{P}$  remains unchanged. This is utilised in adiabatic spin flippers. If  $k \ll 1$ , the change appears sudden and the polarization vector can not follow the field, thus the precession cone will change. This is utilised in DC-spin flippers. If  $k \approx 1$ , it is difficult to make a statement about the movement of the polarization vector.

## 2.3 Neutron Spin Flipper

In the following sections on spin flipping devices some approximations were made. Firstly, the neutrons motion is treated classically, which means that it is possible to assign a distinct velocity and position to the neutron. The spin, on the other hand, is treated quantum mechanically. Furthermore, we assume that the kinetic energy of the neutron is much greater than the potential energy of the magnetic field ( $\frac{\hbar^2 k^2}{2m} \gg \gamma B$ ),

therefore reflection at the boundary can be neglected.

In a full quantum mechanical treatment the neutron is described by a wave packet with no distinct velocity and position. This has minor effects on the flip efficiency.

### 2.3.1 Adiabatic Static Spin Rotators

As discussed in section (2.2.1) the polarization vector will follow the magnetic field if the adiabaticity parameter  $k$  is large enough. This effect can be utilised to rotate the polarization vector in a desired fashion, e.g. rotate it by  $\frac{\pi}{2}$  [KRP91; Kra+03].

Assume a spatially dependent magnetic field, which is pointing in  $z$ -direction at position  $x = 0$  ( $\vec{B}(0) = B \cdot \hat{z}$ ) and in  $x$ -direction at position  $x = L$  ( $\vec{B}(L) = B \cdot \hat{x}$ ). This corresponds to rotation by  $\frac{\pi}{2}$  over the  $y$ -axis. Additionally, assume a neutron beam initially polarized in  $z$ -direction. If the magnetic field is strong enough and the change happens gradually and slowly enough the polarization can follow the magnetic field and will be rotated by  $\frac{\pi}{2}$  as well. A V-coil is capable of carrying out exactly such rotations. Since  $k = \frac{\omega L}{\omega_g}$  with  $\omega_L = \gamma B$  and  $\omega_g = \frac{\pi v}{L}$ , the rotation capability is a function of the strength of the magnetic field  $B$ , the distance  $L$  over which the field changes and the velocity  $v$  of the neutron. This shows that adiabatic rotators are applicable at a white neutron beam if  $k \gg 1$  for the fastest neutrons. In that case the rotation is accomplished for the entire spectrum.

A static flipper is not able to initiate zero field precession as is going to be discussed in section (3.2). They are solely used to prepare neutrons in a coherent spin superposition.

### 2.3.2 Resonant RF Spin Flipper

In this section we want to study the effects of an weak oscillating magnetic field with frequencies in the radio frequency domain (RF) superimposed with a strong static magnetic field on the polarization of the neutron beam. This setup is also used in nuclear magnetic resonance (NMR) experiments and (together with a static gradient field) for magnetic resonance imaging (MRI). If the parameters of such a device are chosen correctly, spin manipulation become possible even spin flips can occur. For the derivation of the dynamics of the polarization we will only consider time dependent fields, since the space dependency can be transformed away if one knows the velocity of the neutrons. Therefore the total magnetic field reads

$$\vec{B}(t) = \begin{pmatrix} B_1 \cos(\omega t) \\ 0 \\ B_0 \end{pmatrix} \quad (2.27)$$

where  $B_1$  is the amplitude of the RF-field oscillating with frequency  $\omega$  and  $B_0$  the magnitude of the static magnetic field. We assume  $x$  as the beam direction. One can decompose an oscillating field in  $x$ -direction into two oppositely rotating fields with the

same frequency but half the amplitude (see figure (2.3))

$$\vec{B}(t) = \begin{pmatrix} \frac{B_1}{2} \cos(\omega t) \\ \frac{B_1}{2} \sin(\omega t) \\ 0 \end{pmatrix} + \begin{pmatrix} \frac{B_1}{2} \cos(\omega t) \\ -\frac{B_1}{2} \sin(\omega t) \\ 0 \end{pmatrix} + \begin{pmatrix} 0 \\ 0 \\ B_0 \end{pmatrix} \quad (2.28)$$

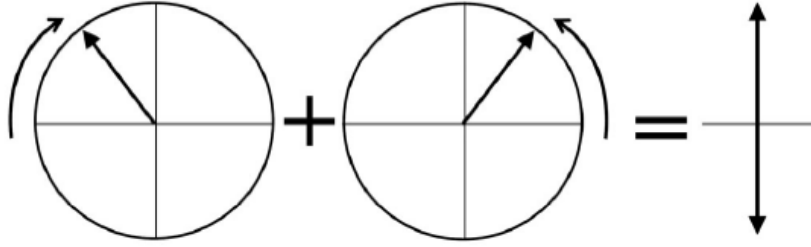


Figure 2.3: An illustration showing the equivalence of two counter rotating fields and one oscillating field. Contrary to what the figure might suggest, the rotating fields must have half the amplitude of the oscillating field. From [Plo09].

It is possible to express the two rotating fields with the help of the rotation matrices  $R$  (see equation (2.24)). Furthermore, a rotation around the  $\hat{n}$ -axis is not changing a vector in  $\hat{n}$ -direction, thus we can write  $B_0\hat{z} = e^{iL_z\omega t}B_0\hat{z}$ . This leads to the following expression for the magnetic field

$$\vec{B}(t) = e^{iL_z\omega t} \left( \frac{B_1}{2}\hat{x} + B_0\hat{z} \right) + \frac{B_1}{2}e^{-iL_z\omega t}\hat{x} \quad (2.29)$$

where the rotating fields are pointing in  $x$ -direction at time  $t = 0$ .

To solve the Larmor equation (2.23) for this time dependent field, we need to transform into a different reference frame, where the magnetic field appears static (or almost static), so that we can use the solution of equation (2.24). To achieve this we change into a rotating frame with the exact same frequency as of the rotating magnetic field. The new polarization vector thus becomes  $\vec{P}_r(t) = e^{-iL_z\omega t}\vec{P}(t) \rightarrow \vec{P}(t) = e^{iL_z\omega t}\vec{P}_r(t)$ . Plugging  $\vec{B}(t)$  and our substitution into the Larmor equation gives us

$$\frac{d}{dt}(e^{iL_z\omega t}\vec{P}_r(t)) = i\gamma\vec{L} \left[ e^{iL_z\omega t} \left( \frac{B_1}{2}\hat{x} + B_0\hat{z} \right) + \frac{B_1}{2}e^{-iL_z\omega t}\hat{x} \right] e^{iL_z\omega t}\vec{P}_r(t) \quad (2.30)$$

Exploiting the commutation relation between the angular momentum operators in adjoint representation ( $[L_i, L_j] = i\epsilon_{ijk}L_k$ ) leads to the following useful relation for constant  $\vec{B}$  fields:  $\vec{L}e^{i\vec{L}\hat{n}\omega t}\vec{B} = e^{i\vec{L}\hat{n}\omega t}\vec{L}\vec{B}e^{-i\vec{L}\hat{n}\omega t}$  [Kra04]. We can now reformulate equation (2.30)

$$\begin{aligned}
 \frac{d}{dt} \left( e^{iL_z\omega t} \vec{P}_r(t) \right) &= i\gamma e^{iL_z\omega t} \vec{L} e^{iL_z\omega t} \left( \frac{B_1}{2} \hat{x} + B_0 \hat{z} \right) P_r(t) + i\gamma \vec{L} e^{-iL_z\omega t} \frac{B_1}{2} \hat{x} e^{iL_z\omega t} P_r(t) \\
 e^{-iL_z\omega t} \frac{d}{dt} \left( e^{iL_z\omega t} \vec{P}_r(t) \right) &= i\gamma \vec{L} e^{iL_z\omega t} \left( \frac{B_1}{2} \hat{x} + B_0 \hat{z} \right) P_r(t) + i\gamma e^{-iL_z2\omega t} \vec{L} \frac{B_1}{2} \hat{x} e^{iL_z2\omega t} P_r(t) \\
 e^{-iL_z\omega t} \frac{d}{dt} \left( e^{iL_z\omega t} \vec{P}_r(t) \right) &= i\gamma \vec{L} e^{iL_z\omega t} \left( \frac{B_1}{2} \hat{x} + B_0 \hat{z} \right) P_r(t) + i\gamma \vec{L} e^{iL_z2\omega t} \frac{B_1}{2} \hat{x} P_r(t)
 \end{aligned} \tag{2.31}$$

Applying the product rule to the left hand side gives

$$e^{-iL_z\omega t} i L_z \omega e^{iL_z\omega t} \vec{P}_r(t) + e^{-iL_z\omega t} e^{iL_z\omega t} \frac{d}{dt} \vec{P}_r(t) = i L_z \omega \vec{P}_r(t) + \frac{d}{dt} \vec{P}_r(t) \tag{2.32}$$

Putting both sides together and rearrange one term gives

$$\begin{aligned}
 \frac{d}{dt} \vec{P}_r(t) &= i\gamma \vec{L} \left[ \frac{B_1}{2} \hat{x} + B_0 \hat{z} \right] \vec{P}_r(t) - iL_z\omega \vec{P}_r(t) + i\gamma \vec{L} \left( e^{iL_z2\omega t} \frac{B_1}{2} \hat{x} \right) \vec{P}_r(t) \\
 \frac{d}{dt} \vec{P}_r(t) &= i\vec{L} \left[ \gamma \frac{B_1}{2} \hat{x} + (\gamma B_0 - \omega) \hat{z} \right] \vec{P}_r(t) + i\gamma \vec{L} \left( e^{iL_z2\omega t} \frac{B_1}{2} \hat{x} \right) \vec{P}_r(t)
 \end{aligned} \tag{2.33}$$

The above equation is the Larmor equation for the polarization in the rotating frame. One can see that the magnetic field has now a constant component and one term, which is rotating rapidly with twice the frequency of the original field (i.e.  $2\omega$ ) and small amplitude ( $B_0 \gg \frac{B_1}{2}$ ). For times  $t \gg \frac{1}{2\omega}$  this latter term is not contributing and averages to zero. Neglecting this term is called the *Rotating Wave Approximation* [HR06], but leaves us with an small shift of resonance frequency called the Bloch-Siegert shift [BS40]. The solution of the dynamics of the polarization in a static field is known and given in equation (2.24). Our polarization vector  $\vec{P}_r$  in the rotating reference frame is therefore

$$\vec{P}_r(t) = \exp \left[ \gamma \frac{B_1}{2} L_x + (\gamma B_0 - \omega) L_z \right] \vec{P}_r(t=0) \tag{2.34}$$

In general  $B_0 \gg B_1$  such that the  $L_z$ -term in the exponent will dominate. The important exception is if  $\gamma B_0 \simeq \omega$ . In this case the second term in the exponent vanishes and we get a clean rotation around the  $x$ -axis (in the rotating reference frame), hence enabling us to flip the polarization. This condition for the frequency ( $\omega = \gamma B_0$ ) of the rotating field (and consequently of the oscillating field) is referred to as *frequency resonance*. Returning to the original reference frame and assuming that  $\vec{P}_r(0) = \vec{P}(0)$  gives

$$\vec{P}(t) = e^{iL_z\omega t} e^{iL_x\gamma \frac{B_1}{2} t} \vec{P}(0) \tag{2.35}$$

One can see that the initial polarization is rotated around the  $x$ -axis by an angle  $\alpha = \gamma \frac{B_1}{2} t$ . Furthermore, the polarization is flipped (i.e. rotated by  $\pi$ ) if  $\alpha = -\pi$  hence

we get a constraint for the strength of the oscillating field, namely  $\alpha = \gamma \frac{B_1}{2} t = -\pi \rightarrow B_1 = \frac{2\pi}{\gamma t}$ . This condition is referred to as *amplitude resonance*. It should be mentioned that the second rotation in equation (2.35) does not have an effect on the polarization only if the vector  $e^{iLx\gamma \frac{B_1}{2} t} \vec{P}(0)$  is pointing in the  $z$ -direction. If we assume an initial beam polarization in  $z$ -direction we get

$$e^{iLz\omega t} e^{iLx\pi} \begin{pmatrix} 0 \\ 0 \\ 1 \end{pmatrix} = e^{iLz\omega t} \begin{pmatrix} 0 \\ 0 \\ -1 \end{pmatrix} = \begin{pmatrix} 0 \\ 0 \\ -1 \end{pmatrix} \quad (2.36)$$

One can see that the polarization has been flipped from  $\vec{P}(t=0) = \begin{pmatrix} 0 \\ 0 \\ 1 \end{pmatrix}$  to  $\vec{P}(t) = \begin{pmatrix} 0 \\ 0 \\ -1 \end{pmatrix}$ .

The flip efficiency  $\epsilon$  is the probability for a spin flip defined as [Kra04]

$$\epsilon = \frac{1 - P_z}{2} \quad (2.37)$$

with  $P_z = \vec{P} \cdot \hat{z}$  the measured polarization after the flipper (equation (2.13)) and  $0 \leq \epsilon \leq 1$ , telling you the normalized amount of flipped spins. This also corresponds to the probability for a single spin to be flipped. Considering an experimental setup, the time  $t$  the neutrons are exposed to the magnetic fields is  $t = \frac{L}{v}$ , where  $L$  is the length of the field region and  $v$  the neutron velocity. This shows that the flip efficiency depends on the neutron velocity. For a resonant RF flipper in frequency resonance the flip efficiency is [Sud05] (expressing  $e^{i\vec{L}\hat{n}\omega t}$  in terms of sines and cosines)

$$\epsilon = \sin^2 \left( \frac{B_1 \gamma t}{4} \right) = \sin^2 \left( \frac{B_1 \gamma L}{4v} \right) \quad (2.38)$$

Therefore a resonant RF flipper only works properly for a very small range of neutron velocities (figure 2.4).

So in general this kind of flipper is not suitable for a white neutron beam. However, there is a method to achieve high flip efficiency for all wavelength (see section 2.3.4). As a final remark on this kind of device, it should be mentioned that one can add an arbitrary phase to the magnetic field such that

$$\begin{pmatrix} B_1 \cos(\omega t) \\ 0 \\ B_0 \end{pmatrix} \rightarrow \begin{pmatrix} B_1 \cos(\omega t + \phi) \\ 0 \\ B_0 \end{pmatrix} \quad (2.39)$$

and still come up with the same expression for the flip efficiency if the initial polarization is  $\vec{P} = \pm \hat{z}$ , i.e. is pointing only in  $z$ -direction [Kra04]. Hence, it does not

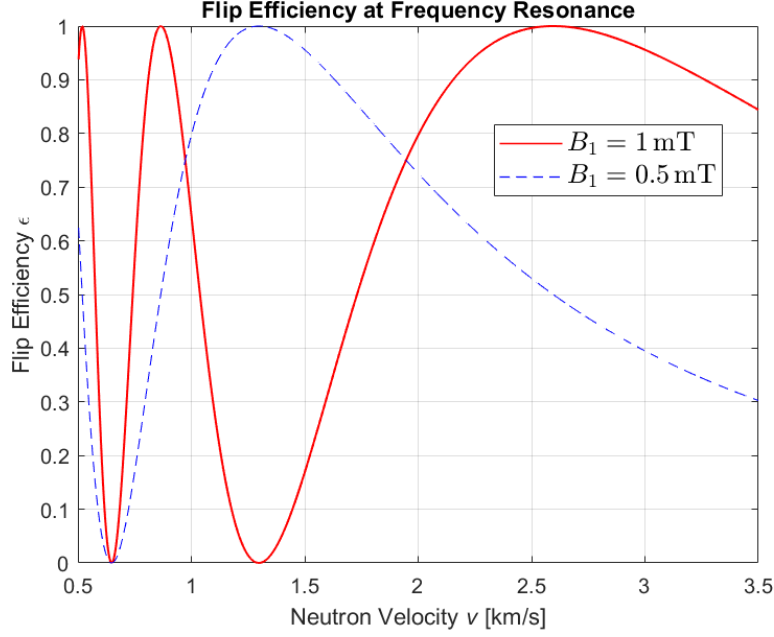


Figure 2.4: Plot showing the flip efficiency versus neutron velocity (equation (2.38)) at frequency resonance for  $L = 0.089$  m and two different amplitudes of the oscillating field (1 mT and 0.5 mT). High efficiencies (e.g.  $\epsilon \geq 0.98$ ) are achieved only for small velocity ranges.

matter during what phase of the oscillation process of the RF field (i.e. at what time) the neutron enters the flipper. The polarization vector after the RF flipper including a phase  $\phi$  of the oscillating field is

$$\vec{P}(t) = e^{iL_z\omega t + 2\phi} e^{iL_x\gamma\frac{B_1}{2}t} \vec{P}(0) \quad (2.40)$$

Due to the close analogy of the spinor Larmor equation (equation (2.10)) and the Larmor equation for the polarization (equation (2.23)), we can write down the solution in the spinor case in frequency resonance as

$$|S(t)\rangle = e^{\frac{1}{2}i\sigma_z\omega t} e^{\frac{1}{2}i\sigma_x\gamma\frac{B_1}{2}t} |S(0)\rangle \quad (2.41)$$

The amplitude resonance condition for a  $\pi$ -flip is identical to the polarization,  $B_1 = \frac{2\pi}{\gamma t}$ . The  $\sigma_z$  matrix exponential is inducing a state dependent phase originating from the energy difference the two spin states experience. One can bother an alternative picture from atomic physics to describe this phenomenon qualitatively. The static magnetic field  $B_0$  is splitting the degenerate energy level of the free neutron into two levels (Zeeman splitting). It is then possible to address the transition between the different levels (i.e. states  $|\downarrow\rangle, |\uparrow\rangle$ ) by photon (RF field) emission or absorption, respectively. Thus the total energy of the neutrons can be changed in an RF flipper by interaction with photons, contrary to static DC-flippers where the total energy of the neutron does not change.

### 2.3.3 Adiabatic RF Spin Flipper

Another device similar to the resonant RF spin flipper is the adiabatic RF spin flipper, first described in 1975 [YuV75]. Contrary to the former it is capable to efficiently flip spins for a broad range of neutron velocities. This of course comes in handy at the white beam line. The crucial difference is an additional static magnetic gradient, which is superimposed with the strong  $B_0$  field. The resulting magnetic field is time and space dependent, where  $x$  is the direction the beam is propagating.

$$\vec{B}(x, t) = \left[ B_0 + B_{GR} \cos\left(\frac{\pi x}{L}\right) \right] \hat{z} + B_1 \sin\left(\frac{\pi x}{L}\right) \cos(\omega t) \hat{x} \quad (2.42)$$

with  $B_{GR}$  the amplitude of the gradient field,  $L$  the length of the field region and  $B_1$  the amplitude of the RF field. We assumed that the gradient is cosine-shaped and that the amplitude of the RF field is sine-shaped, such that it is zero at the begin and the end of the flipper and has its maximum value in the middle (see figure (2.5)).

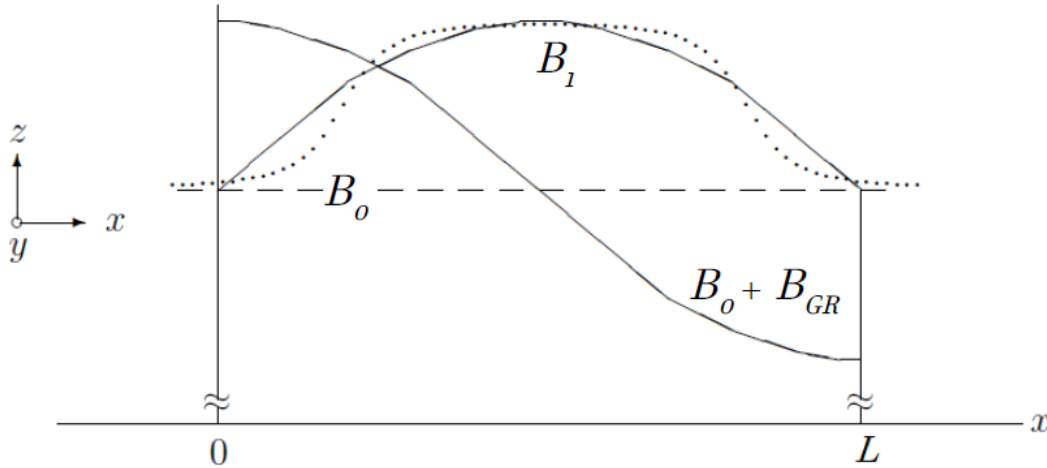


Figure 2.5: Magnetic field configuration at an adiabatic RF spin flipper with length  $L$ . The static field in  $z$ -direction becomes space dependent, due to the gradient field  $B_{GR}$ . The amplitude of the RF field  $B_1$  is also space dependent and approximated with a sine function (dotted line: in practice). The neutron beam is along the  $x$ -direction. From [Kra04]

This is a reasonable approximation for most RF coils. To be precise, we already should have taken this amplitude shape into account for the magnetic field of the RF flipper (see 2.3.2), but have implicitly assumed an average value of the magnetic field, which is constant throughout the device. In this case we will explicitly take the sine-shaped amplitude of the RF field into account. Using a constant neutron velocity  $v$  we get rid of the space dependency ( $x = vt$ ). Furthermore, we define the geometric rotation frequency as  $\omega_g = \frac{\pi v}{L}$ , assume resonance condition ( $\omega = \gamma B_0$ ) and set  $B_1/2 = B_{GR}$  as well as  $B_0 \gg B_1$ . Finally we decompose the oscillating field into two rotating fields like in the previous section and end up with [Kra04]



$$\vec{B}(t) = B_0 \hat{z} + \frac{B_1}{2} e^{iL_z \omega t} e^{-iL_y \omega_g t} \hat{z} + \frac{B_1}{2} e^{-iL_z \omega t} \sin(\omega_g t) \hat{x} \quad (2.43)$$

where the rotation around  $y$  accounts for the gradient field. To solve the Larmor equation for the polarization vector under the effect of such a field we again transform into a rotating frame with frequency  $\omega$  rotating around  $z$ -axis, hence  $\vec{P}(t) = e^{iL_z \omega t} \vec{P}_r(t)$ . Plugging this into our Larmor equation and remembering the commutation relations and  $\omega = \gamma B_0$  yields

$$\frac{d}{dt} \vec{P}_r(t) = i\gamma \sin(\omega_g t) \vec{L} e^{-iL_z 2\omega t} \frac{B_1}{2} \hat{x} \vec{P}_r(t) + i\gamma e^{-iL_z \omega t} \vec{L} e^{iL_z \omega t} e^{-iL_y \omega_g t} \frac{B_1}{2} \hat{z} e^{iL_z \omega t} \vec{P}_r(t) \quad (2.44)$$

The first term is again a fast rotating field, which we can neglect and the second can be reformulated using commutation relations such that

$$\frac{d}{dt} \vec{P}_r(t) = i\gamma \vec{L} e^{-iL_y \omega_g t} \frac{B_1}{2} \hat{z} \vec{P}_r(t) \quad (2.45)$$

It follows that the resulting effective magnetic field in the singly rotating reference frame is still rotating around the  $y$ -axis. This is of course due to the cosine-shaped gradient field. Already at this point one can relate this magnetic field to equation (2.29), which describes an RF flipper operated in frequency resonance and the rotating wave approximation already applied. The resulting magnetic field is of the same form as equation (2.45). Thus the next step is to change to another rotating reference frame, in order to end up with an constant magnetic field  $\vec{B}$ . The polarization vector in the doubly rotating frame reads  $\vec{P}_{rr}(t) = e^{iL_y \omega_g t} \vec{P}_r(t) \rightarrow \vec{P}_r(t) = e^{-iL_y \omega_g t} \vec{P}_{rr}(t)$ . Substituting this to equation (2.45) yields

$$\frac{d}{dt} \vec{P}_{rr}(t) = i\gamma \vec{L} \frac{B_1}{2} \hat{z} \vec{P}_{rr}(t) + i L_y \omega_g \vec{P}_{rr}(t) \quad (2.46)$$

$$\frac{d}{dt} \vec{P}_{rr}(t) = i\gamma \vec{L} \left[ \frac{B_1}{2} \hat{z} + \frac{\omega_g}{\gamma} \hat{y} \right] \vec{P}_{rr}(t) \quad (2.47)$$

In this doubly rotating reference frame the  $\vec{B}$  field is constant, hence we can easily solve the Larmor equation.

$$\vec{P}_{rr}(t) = e^{i\gamma \vec{L} \left[ \frac{B_1}{2} \hat{z} + \frac{\omega_g}{\gamma} \hat{y} \right] t} \vec{P}_{rr}(0) \quad (2.48)$$

We assume  $\vec{P}(t=0) = \vec{P}_r(t=0) = \vec{P}_{rr}(t=0)$  and transform back to the original frame.

$$\vec{P}(t) = e^{iL_z \omega t} e^{iL_y \omega_g t} e^{i\gamma \vec{L} \left[ \frac{B_1}{2} \hat{z} + \frac{\omega_g}{\gamma} \hat{y} \right] t} \vec{P}(0) \quad (2.49)$$

The neutrons enter the flipper at time  $t=0$  and we want to calculate the polarization right after the flipper  $\vec{P}_f(t=t_f)$  at time  $t_f = \frac{L}{v}$ . From this follows  $\omega_g t_f = \pi$  and for the polarization

$$\vec{P}_f(t=L/v) = e^{iLz\frac{\omega}{\omega_g}\pi} e^{iL_y\pi} e^{i\gamma\vec{L}\left[\frac{B_1}{2}\hat{z} + \frac{\omega_g}{\gamma}\hat{y}\right]}\frac{\pi}{\omega_g}\vec{P}(0) \quad (2.50)$$

The first rotation acting on  $\vec{P}(0)$  is not about a conventional axis, but rather around an axis  $\hat{m} = \frac{\gamma B_1/2}{\Omega}\hat{z} + \frac{\omega_g}{\Omega}\hat{y}$  where  $\Omega$  is the length of the vector given by  $\Omega = \sqrt{\gamma^2(\frac{B_1}{2})^2 + \omega_g^2}$  and  $\hat{m}$  is a vector in the  $y$ - $z$ -plane (see figure 2.6).

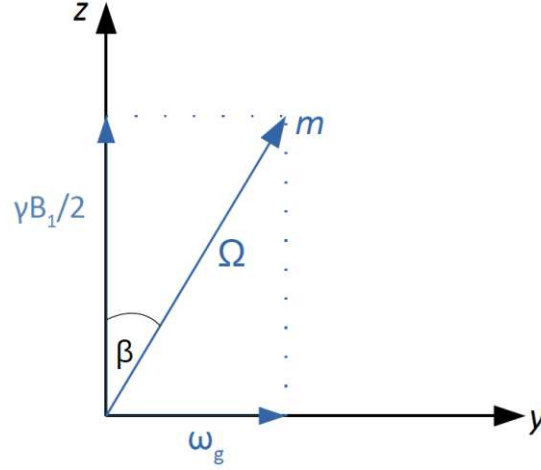


Figure 2.6: Geometric representation of the  $m$ -axis in the  $y$ - $z$  plane. The angle  $\beta$  is given by  $\sin(\beta) = \frac{\omega_g}{\Omega} = \frac{1}{\sqrt{1+k^2}}$ , therefore decreasing with the adiabaticity parameter  $k$ . For large enough  $k$  one can assume that the  $m$ -axis is identical to the  $z$ -axis.

This rotation can be transformed into rotations around the conventional axis. First we rotate  $\hat{m}$  to the  $z$ -axis. Next we do the rotation around the  $z$ -axis, followed by the rotation back to the  $\hat{m}$ -axis. Thus we can write this rotation around the  $\hat{m}$ -axis as [Col15]

$$e^{i\gamma\vec{L}\left[\frac{B_1}{2}\hat{z} + \frac{\omega_g}{\gamma}\hat{y}\right]t} = e^{iL_x\beta} e^{iL_z\Omega t} e^{-iL_x\beta} \quad (2.51)$$

where  $\beta$  is the angle between  $\hat{m}$  and  $\hat{z}$ ,  $\sin(\beta) = \frac{\omega_g}{\Omega}$ . The adiabaticity parameter  $k$  for this kind of flipper can be described by the ratio of the Larmor frequency induced by the RF field and the geometric frequency, reading  $k = \frac{\omega_{L,rf}}{\omega_g} = \frac{\gamma B_1/2}{\omega_g}$ . It follows that  $\Omega = \omega_g\sqrt{1+k^2}$  and  $\sin(\beta) = \frac{1}{\sqrt{1+k^2}}$ . Together with equation (2.51) we can write the solution for the polarization vector as

$$\vec{P}_f(t=L/v) = e^{iLz\frac{\omega}{\omega_g}\pi} e^{iL_y\pi} e^{iL_x\frac{1}{\sqrt{1+k^2}}} e^{iL_z\pi\sqrt{1+k^2}} e^{-iL_x\frac{1}{\sqrt{1+k^2}}} \vec{P}(0) \quad (2.52)$$

Now we assume that the beam is initially polarized in  $z$ , meaning  $\vec{P}(0) = \hat{z}$ . From this we can calculate the  $z$ -component of the polarization after the flipper (again writing the exponentials in terms of sine and cosine i.e. as rotation matrices). It reads

$$P_f \cdot \hat{z} = \frac{2}{1+k^2} \sin^2\left(\frac{\pi}{2}\sqrt{1+k^2}\right) - 1 \quad (2.53)$$

The flip efficiency of this flipper is subsequently (equation (2.37)) [GOR97]

$$\epsilon = 1 - \frac{1}{1+k^2} \sin^2 \left( \frac{\pi}{2} \sqrt{1+k^2} \right) \quad (2.54)$$

One has  $\epsilon = \epsilon(k) = \epsilon(B_1, B_{GR}, v, L)$ , i.e. the flip efficiency is a function of the oscillating field  $B_1$ , the gradient field  $B_{GR}$ , the neutron velocity  $v$  and the length of the flipping device  $L$ . The flip efficiency for a monochromatic beam and a white beam is depicted in figure (2.7).

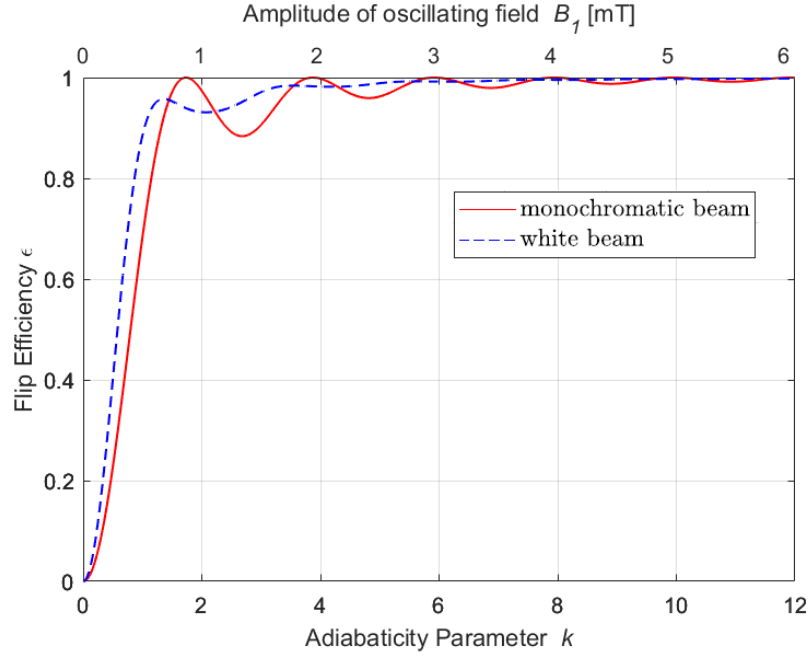


Figure 2.7: Flip efficiency for a monochromatic beam and for a white beam, both initially polarized in  $z$ -direction. The velocity of the former is assumed to be equal to the maximum velocity in the white beam spectrum. The length of the flipper was set to  $L = 0.089$  m. The monochromatic beam follows equation (2.54) with  $k$  being changed by  $B_1$ , since  $L$  and  $v$  are fixed. For the white beam an uniform velocity distribution between  $6 \text{ \AA} = 660 \text{ m/s}$  and  $3 \text{ \AA} = 1319 \text{ m/s}$  has been assumed. The flip efficiency was averaged over the entire ensemble and  $k$  then refers to the fastest neutrons i.e.  $k = \omega_{L,rf}/\omega_g = (\gamma \frac{B_1}{2}) / (\frac{\pi v_{max}}{L})$ . For both cases, the overall efficiency increases with  $k$ .

The increase of the flip efficiency with higher  $k$  can also be seen in the equation of motion of the polarization vector (equation (2.52)). For large  $k$  ( $\gamma \frac{B_1}{2} \gg \omega_g$ ), the  $\hat{m}$ -axis turns closer to the  $z$ -axis therefore  $\beta \approx 0$  and we can neglect the rotations around the  $x$ -axis. Furthermore,  $\Omega \approx \gamma \frac{B_1}{2}$  in this limit. This yields

$$\vec{P}_f = e^{iLz \frac{\omega}{\omega_g} \pi} e^{-iLz \frac{\gamma B_1 \pi}{2\omega_g}} e^{iLy \pi} \vec{P}(0) \quad (2.55)$$

where we used the following relation,  $e^{iLy \pi} e^{iLz \frac{\gamma B_1 \pi}{2\omega_g}} = e^{-iLz \frac{\gamma B_1 \pi}{2\omega_g}} e^{iLy \pi}$ . The first rotation about the  $y$ -axis is flipping the polarization by an angle  $\pi$ . If  $\vec{P}(0) = \hat{z}$  ( $\vec{P}(0) = -\hat{z}$ ) the polarization becomes  $\vec{P} = -\hat{z}$  ( $\vec{P} = \hat{z}$ ). The subsequent rotations

	resonant RF Flipper			adiabatic RF Flipper		
	$B_1$	flip eff.	power	$B_1$	flip eff.	power
monochromatic beam	$\frac{2\pi v}{\gamma L}$	1	$P_{rf}$	$\sqrt{3}\frac{2\pi v}{\gamma L}$	1	$3 \cdot P_{rf}$
white beam	$\frac{2\pi v}{\gamma L}$	0.4572	$P_{rf}$	$5\frac{2\pi v}{\gamma L}$	0.9889	$25 \cdot P_{rf}$

Table 2.2: Table comparing a resonant to an adiabatic RF flipper. For the white beam the same distribution as for figure (2.7) has been assumed. So the velocity of the monochromatic beam is equal to the maximum velocity of the white beam. As expected, the adiabatic RF flipper achieves much higher flip efficiencies at a white neutron beam. The drawback is the significantly higher electric power demand, which can be an engineering challenge at an experimental setup. The value  $k = 5$  for the adiabatic RF flipper at the white beam was chosen as an example. One of course could increase this value to achieve higher flip efficiency, but needs to be aware of the quadratically increasing power demand.

around the  $z$ -axis do not change the polarization any more, thus leaving us with a spin flip for all neutron velocities for which  $\gamma\frac{B_1}{2} \gg \omega_g$ . Moreover, just like for the resonant RF flipper, it can be shown that the phase of the oscillating RF field does not influence the flip efficiency [Kra04]. Furthermore, in both cases the total energy of the neutron is changed by photon absorption or emission. The spinor function after the adiabatic RF flipper is given by

$$|S(t)\rangle = e^{i\frac{\sigma_z}{2}t(\omega - \gamma\frac{B_1}{2})} e^{i\frac{\sigma_y}{2}\pi} |S(0)\rangle \quad (2.56)$$

If the two different RF flipping devices are compared, one can see that the amplitude of the RF field must be significantly higher in the adiabatic flipper case. To flip spins of a monochromatic neutron beam with velocity  $v$  with a resonant RF flipper, the amplitude of the oscillating field must be  $B_1 = \frac{2\pi v}{\gamma L}$ , whereas for the adiabatic RF flipper one needs  $B_1 = k\frac{2\pi v}{\gamma L}$ , with the smallest  $k$  value to also achieve 100 % efficiency being  $\sqrt{3}$  (see figure 2.6). The electric power  $P$  is proportional to  $B_1^2$  (see table 4.1 and 5.1). For the resonant RF flipper the power needed for a flip is  $P = P_{rf}$ . Table (2.2) summarizes the comparison between the two devices.

### 2.3.4 Time Dependent RF Amplitude

A method to flip neutron spins at a white beam efficiently with an RF flipper requires an option for time-of-flight (TOF), where all neutrons start at the same time from the same position. To achieve this a chopping system is required, which turns the continuous beam into a pulsed one. The technical implementation is explained in section (4). The spin-flip probability  $\epsilon$  at frequency resonance for a neutron with velocity  $v$  passing

through a device of length  $L$  with an RF amplitude  $B_1$  is given by (see also equation (2.38))

$$\epsilon = \sin^2 \left( \frac{B_1 \gamma t}{4} \right) = \sin^2 \left( \frac{B_1 \gamma L}{4v} \right) \quad (2.57)$$

We want  $\epsilon = 1$  therefore the argument of the sine function must be equal to  $\frac{\pi}{2}$ . Lets assume the neutron starts flying towards the RF flipper at time  $t = 0$  a distant  $d$  away from the device. We can therefore write the velocity as  $v = \frac{d}{t}$ . This leads us to the following expression

$$\frac{\pi}{2} = \frac{B_1 \gamma L t}{4d} \rightarrow B_1 = \frac{2\pi d}{\gamma L t} \quad (2.58)$$

The resulting magnetic field becomes time dependent and the amplitude decays with  $\propto \frac{1}{t}$  [Mar+03]. Most importantly, the probability for a  $\pi$ -flip becomes independent of the velocity of the neutron, thus becoming applicable at a pulsed white beam. Fast neutrons will experience a strong magnetic field for a short time, whereas slow neutrons arrive later at the flipper, thus experiencing a weaker magnetic field, but for a longer time period. Both cases result in the same spinor wave function.

The neutron pulse and the RF signal must be timed correctly. Additionally one needs to be aware of very slow neutrons being counted as very fast. This *frame overlap* can occur, if the time between two pulses is set to short, such that slow neutrons from the first pulse arrive at the RF flipper at the start of the second. Overall, a time dependent RF amplitude  $B_1(t)$  is capable of flipping spins at a pulsed white neutron beam.

## 2.4 Reflection and Supermirrors

In order to understand the principle of polarizing supermirrors, we first look at the general case of an incident neutron on a materials surface, i.e. the transition of a region of zero potential (free particle) to a region of finite potential. In close analogy to theory of optics of electromagnetic wave, we can write an index of refraction as [RW15]

$$n(\vec{r}) = \left[ 1 - \frac{V(\vec{r})}{E} \right]^{\frac{1}{2}} \quad (2.59)$$

where  $V(\vec{r})$  is the potential and  $E$  the energy eigenvalue of the neutron. There are a handful of different interaction potential terms [Sea86], most notably the Fermi pseudopotential term  $V_N$  and the well known Zeeman term. Former is describing the strong force interaction between the nucleus of a material at sites  $\vec{r}_j$  and the neutrons


$$V_N(\vec{r}) = \sum_j \frac{2\pi\hbar}{m} b_c \delta(\vec{r} - \vec{r}_j) \approx \frac{2\pi\hbar^2}{m} b_c N \quad (2.60)$$

the parameter  $b_c$  is called the coherent scattering length and is a material constant and  $N$  the atom density. The approximation yields from averaging the potential over a macroscopic volume. The Zeeman term reads  $V_{mag}(\vec{r}) = -\vec{\mu} \cdot \vec{B}(\vec{r})$  (see section 2.2). If we assume two field regions with index of reflection  $n_1$  and  $n_2$  and a neutron incident from region 1 impinging on region 2, we know that for any type of wave (e.g. [Dem08]) total reflection can only occur if  $n_1 > n_2$ . Lets assume region 1 to be air, for which holds  $n_1 = n_{air} \approx n_{vacuum} = 1$ . For neutrons vacuum is an optically denser medium than most materials, hence total reflection is possible in those cases. Furthermore, the critical angle for total reflection  $\theta_c$  is given by [UI10]

$$\theta_c = \left[ \frac{V}{E_\perp} \right]^{\frac{1}{2}} = \left[ \arcsin \left( V \frac{m\lambda}{2\pi^2\hbar^2} \right) \right]^{\frac{1}{2}} \quad (2.61)$$

where  $E_\perp$  is the energy of the free neutron perpendicular to the surface of the material. The critical angle depends on the wavelength of the incident neutron  $\lambda$  and on the potential  $V$  in region 2. The critical angle at the boundary of air to Nickel has a critical angle of  $\theta_c^{Ni} = 0.1^\circ/\text{\AA}$  [Ima11]. To achieve high reflectivity over a broader wavelength range and greater grazing angles, supermirrors are used [Mez76; Mez77]. These devices exploit Bragg diffraction, similar to monochromators. For grazing angles  $\theta > \theta_c$ , the incident beam will be partially transmitted and partially reflected. If a second boundary is placed behind the first, constructive interference between the beams reflected from the two boundaries can be observed if the optical path difference is  $n\lambda$  (Bragg condition). Hence reflection for these wavelength occur (Bragg peak). One can extend this principle to a multilayer structure with slightly varying distances between the individual layers, see figure (2.8). This results in a much higher reflectivity for a broader wavelength range compared to total reflection.

In order to obtain polarizing supermirrors we need to alternate magnetic and non-magnetic materials in such a way that for one spin component (e.g.  $|\uparrow\rangle$ ) the potentials of the two materials is equal. Remembering equation (2.3) and (2.60) we write  $V_{N,a} = V_{N,b} \pm V_{mag,b}$ , for a non-magnetic material  $a$  and a magnetic material  $b$ . Therefore the index of refraction are the same for this spin component and no reflection occurs. Moreover, the other spin component does experience a change in refractive index and thus gets reflected. In this way a spatial separation of the two spin states is possible for a broad wavelength range. One spin state is absorbed, the other one is utilised in the experiment. Polarizing supermirrors are characterized by their  $m$ -value defined as  $m = \theta_{Mirror}/\theta_{Ni}$ . Figure (2.9) shows the reflectivity and obtained polarization for different grazing angles in units of the  $m$ -value.

One needs to keep in mind that the grazing angles with high reflectivity are still very small. That means that a high divergence of the neutron beam can lead to a decreasing intensity if supermirrors are used in the setup. The supermirrors used at the white beam are manufactured by Swiss Neutronics and generate a neutron beam

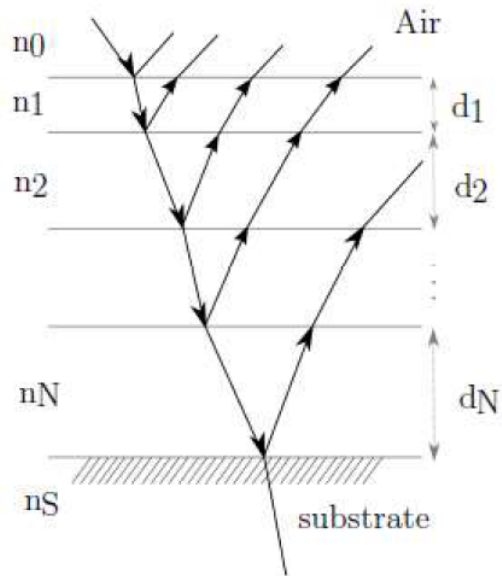


Figure 2.8: A multilayer structure with varying spacing as used in supermirrors. From [Dem13].

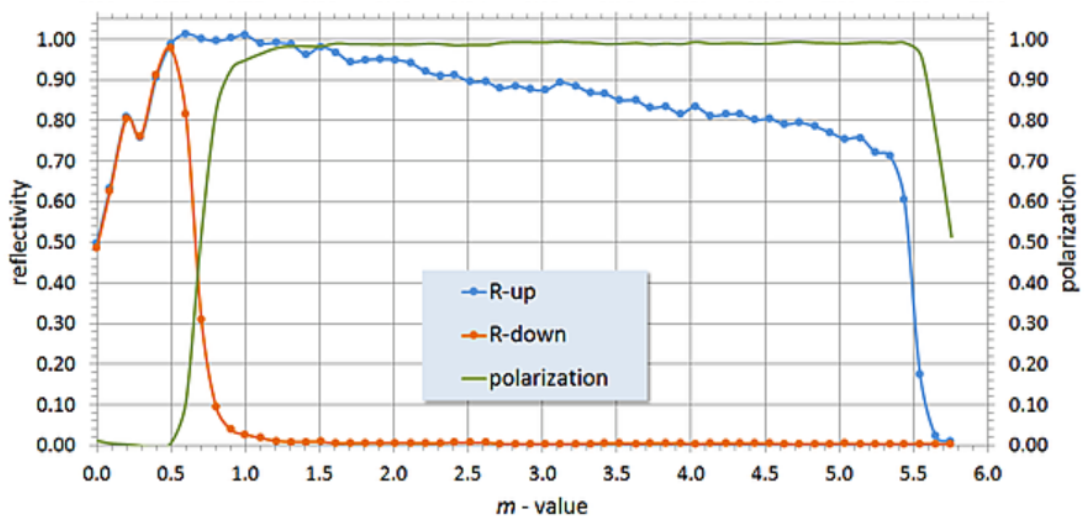


Figure 2.9: A Fe/Si polarizing supermirror. For certain grazing angles only the up-spin state is reflected. From [www.swissneutronics.ch/products/neutron-supermirrors](http://www.swissneutronics.ch/products/neutron-supermirrors).

with a degree of polarization  $> 0.99$ . Supermirrors are used as polarisers as well as spin analysers.

## 2.5 Neutron Source and Counting Statistics

At the Atominstut Vienna, neutrons are provided by a TRIGA MARK II reactor of swimming pool type (see figure (2.10)). Construction were finished in 1962. The fuel, 19.8 % Uranium-235, is fissured and produces on average 2.5 neutrons. They are then slowed down by a moderator, which is in this case water. They reach thermal

equilibrium and show a Maxwellian energy distribution [RW15]. According to their kinetic energy the neutrons are now thermal neutrons. The thermal power output of the reactor is rather low and amounts to 250 kW with a thermal flux at the central irradiation tube in the core of  $10^{13} \text{ m}^{-2} \text{ s}^{-1}$  [Wie20]. Four beamports (one tangential, three radial) guide the neutrons to the experiments, whereby one of them is the white neutron beam line [Mac18].



Figure 2.10: The TRIGA MARK II research reactor in Vienna [Wie20]. The white beam line is on back side and not visibly in this photo.

The installation of the white beam line was supervised by the team of the TRIGA Center, most notably W. Mach and was finished in 2018 [Mac18]. The beam experimental site is shielded by a boron enriched concrete and only accessible when the beam is blocked (see figure (2.11)). An interlock system and the a lattice door control the access. In the pre-chamber a heavy concrete block is mounted on a hydraulic lift table, which acts as a beam shutter. Furthermore, the shutter block can only be controlled from the outside after a "search-button" inside the site is pressed to ensure that nobody is inside the chamber when the beam is opened. At the beamport between pre-chamber and experimental site a supermirror is installed and embedded in the concrete. Due to the divergence of the beam at this position, some neutrons hit the reflective side of the mirror, whereas some are passing the beamport without interacting with matter. This results in two neutron beams at the experimental site inclining an angle of about  $1^\circ$ .



The one reflected from the mirror is polarized contrary to the other. The unpolarized beam has a higher flux and is absorbed at the end of the experimental site by a beamstop. Experiments were solely utilising the polarized beam, which has a flux of about  $1.5 \times 10^5 \text{ s}^{-1}$  (detector saturation). The experimental site is rather short with a total length of 3.7 m. This is an important feature to consider when deriving the technical parameters of the experiment (see table 4.1).

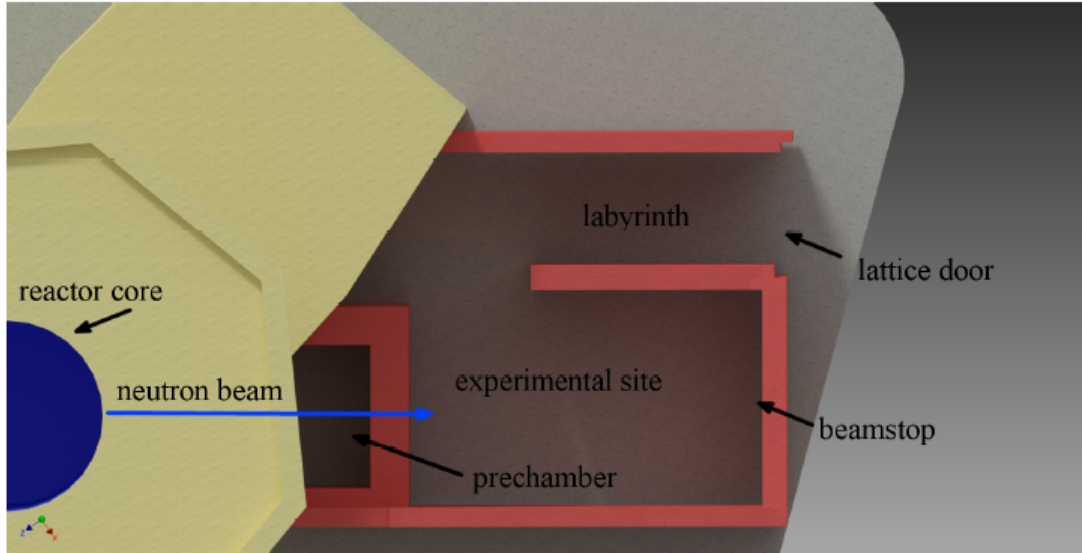


Figure 2.11: Sketch of the white beam line, aerial perspective. From [Mac18]

## Counting Statistics

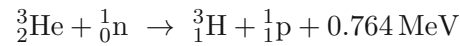
Since the occurrence of detection events at small time intervals has a constant probability, is independent from the absolute time and does not depend on the time since the last event, we can say that the number of counts  $N$  registered obey a Poisson distribution [RW15].

$$P(N) = \frac{\bar{N}^N}{N!} e^{-\bar{N}} \quad (2.62)$$

where  $\bar{N}$  is the mean count value. Hence, the variance of the counts can be written as  $(\Delta N)^2 = \bar{N}$  and the standard deviation as  $\Delta N = \sqrt{\bar{N}}$ . The measurement error is therefore calculated by taking the square root of the measured counts. Moreover, the relative error is  $\frac{\Delta N}{N} = \frac{\sqrt{\bar{N}}}{N} = \frac{1}{\sqrt{\bar{N}}}$ , which means that the relative error can be reduced by higher count value, achieved either through longer measurement times or higher flux. Making a beam monochromatic reduces the flux drastically. The white neutron beam has the highest flux of all beamports in Vienna, but the drawback that a polychromatic beam is not easy to handle in terms of spin flipping.

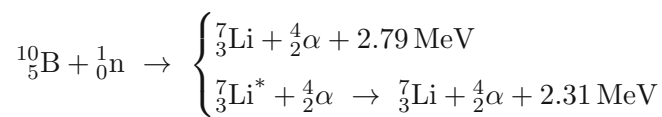
## 2.6 Detector

Since neutrons do not carry electrical charge, they can not directly be convert into measurable electrical signal. However, it is possible to detect them indirectly through arising reaction products. A widely used type of detectors are gas filled ionisation chambers, where a gaseous element with a high neutron absorption cross section is placed in a strong electric field [Kno89]. The detector is often cylindrically shaped with a wire along the longitudinal axis serving as the anode and the shell as the cathode. Thus, electrically charged reaction products will drift towards the anode (cathode) and induce an electrical signal. Two important detection mediums are Boron-10 and Helium-3. The latter has a 40 % higher absorption cross section and is used at the white beam line in Vienna. Detection process starts with the following reaction



The 0.764 MeV are transferred to the reaction products as kinetic energy. When the charged particles hit the an electrode they are inducing a current and can thus be counted. The detector used for the experiments is 1 inch in diameter.

The Boron-10 reaction equation reads



where the electrical signal is generated by the Helium nuclei. Due to the indirect detection method any information on energy and polarization of the neutron is lost during the detecting process .

## Chapter 3

# Spin Echo

Since the first description of neutron spin echo (NSE) in 1972 [Mez72] the technique has continuously been extended to more sophisticated version like neutron resonance spin echo (NRSE) [GG87] or the application of neutron spin echo to small angle neutron scattering [Kel+95; Rek96]. This technique uses two oppositely orientated magnetic field regions, where the second one reverses the Larmor precession of the first region leading to a spin echo. The underlying physical phenomena of Larmor precession as described in section 2.2 is spin interferometry (sometimes called Larmor interferometry). Even though the former description is sufficient for the most part, we will in this chapter study the semi classical description of spin interferometry as well.

Furthermore, at a neutron scattering experiment the spin echo method can achieve high energy resolution below the wavelength spread of the beam and it becomes possible to directly determine the cosine Fourier transform of the scattering function [Mez80; Gäh+96]. NSE is an inelastic scattering technique used to resolve dynamics in the sample on timescales of some picoseconds up to a few nanoseconds. The most powerful instrument is the IN15 spectrometer at the Institut Laue-Langevin in Grenoble with spin echo times up to 1  $\mu$ s [Lau]. In a similar way, SESANS can resolve scattering angles smaller than the beam divergence, whereas small angle neutron scattering cannot. With this technique it is possible investigate structures in the range of 5 nm–20  $\mu$ m [Rek+05]. Nevertheless, this chapter will not focus entirely on the examination of a sample material, but rather on the dynamics of the neutron spin and the polarization of the beam in such a setup.

### 3.1 Neutron Spin Echo (NSE)

#### 3.1.1 Classical Model: Larmor Precession

Let us assume a setup as sketched in figure (3.1). A neutron beam polarized in the direction of the guide field  $\vec{B}$  ( $z$ -direction) is incident on the magnetic field region from the left. In the following derivations we use the reasonable assumption that the energy

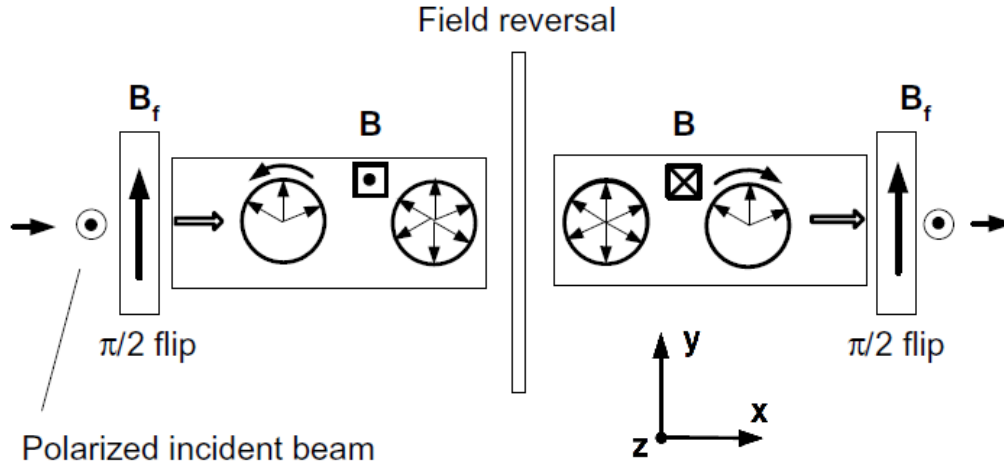


Figure 3.1: Magnetic field configuration of a Neutron Spin Echo (NSE) instrument. The small arrows in circles indicate Larmor precession of the neutron spins. A polarized neutron beam is incident from the left. In the first field region the neutron spins will obtain different Larmor precession angles. After the second field region of same magnitude (before the second  $\pi/2$  rotation) all acquired precession angles will be reversed. Therefore the initial polarization is restored. This sketch does not show a sample, but it would be placed at the position of the field reversal. From [Sud05]

of the free neutron is much larger than the Zeeman splitting (i.e.  $\mu B \ll \frac{\hbar^2 k^2}{2m}$ ) and thus neglect reflections at the boundary of the magnetic field regions. First, the neutrons pass through a static flipper with a magnetic field  $\vec{B}_f$  pointing in  $y$ -direction to rotate the spins by  $\frac{\pi}{2}$  into the  $x$ - $y$ -plane. Directly after the rotation the spins are pointing in positive  $x$ -direction.

The neutrons then enter the guide field  $\vec{B}$ , which is orthogonal to the neutrons spin thus Larmor precession occurs, which is governed by the Bloch equation (2.21). The precession angle is given by  $\alpha = \omega_L t = \frac{\gamma B L}{v}$  ( $\omega_L$  the Larmor frequency,  $B = |\vec{B}|$ ,  $L$  the length of the magnetic field region and  $v$  the neutron velocity). The angle is time dependent and consequently velocity dependent, which means that neutrons with different velocities will have different Larmor precession angles at the end of this field region. One can view these different angles as individual clocks telling the time the neutron spent in the magnetic field.

The next and crucial step is the field reversal (see figure 3.1). This can either be done by a second guide field pointing in the exact opposite direction (say  $-z$ -direction) or by a  $\pi$  flip. In the latter case the spin will remain in the  $x$ - $y$ -plane but the precession angle will be transformed from  $\alpha$  to  $-\alpha$ .

In the second guide field region of length  $L'$  and strength  $B'$  the neutron spin acquires an additional angle  $\alpha'$ . The net spin precession angle is therefore

$$\delta\alpha = -\alpha + \alpha' = -\frac{\gamma}{v}(BL - B'L') \quad (3.1)$$

The effect of the first field region is completely compensated by the second one if  $B = B'$  and  $L = L'$  (and  $v = v'$ ).

As a last step we flip the spins by  $-\frac{\pi}{2}$ . The initial state will be recovered if the net precession is zero, otherwise we end up with a different state.

The Larmor equation for the polarization vector can easily be solved (compare section 2.2). The beam is initially polarized in  $z$ -direction. After the first  $\frac{\pi}{2}$  rotation around the  $y$ -direction the polarization is pointing in the  $x$ -direction. It then precesses around the  $z$ -direction about an angle  $\delta\alpha$ . The last rotation of  $-\frac{\pi}{2}$  around the  $y$ -axis yields a polarization vector in the  $y$ - $z$ -plane with its components depending on the total net precession angle  $\delta\alpha$ .

$$\vec{P} = \begin{pmatrix} \langle\sigma_x\rangle \\ \langle\sigma_y\rangle \\ \langle\sigma_z\rangle \end{pmatrix} = \begin{pmatrix} 0 \\ 0 \\ 1 \end{pmatrix} \xrightarrow{(\pi/2)_y} \begin{pmatrix} 1 \\ 0 \\ 0 \end{pmatrix} \xrightarrow{(\delta\alpha)_z} \begin{pmatrix} \cos(\delta\alpha) \\ \sin(\delta\alpha) \\ 0 \end{pmatrix} \xrightarrow{(-\pi/2)_y} \begin{pmatrix} 0 \\ \sin(\delta\alpha) \\ \cos(\delta\alpha) \end{pmatrix} \quad (3.2)$$

If the polarization is measured in  $z$ -direction  $\langle\sigma_z\rangle$ , we can see that it is dependent on the precession angle  $\delta\alpha$ . The spin echo condition is met if  $\delta\alpha = 0$ . Furthermore, the intensity shows a damped oscillation in  $\delta\alpha$ , where the damping is proportional to the wavelength spread of the beam. Therefore it first decreases with  $\delta\alpha$  until  $\delta\alpha = \pi$  and can reach local maxima for multiples of  $2\pi$ .

In the case of a scattering experiment a sample would be placed between the guide fields. The rest of the instrument is set up as described above (i.e.  $B = B'$  and  $L = L'$ ). If the neutrons scatter inelastically from the sample the velocity in the second region  $v'$  is shifted which influences the precession angle acquired in the second region. We will assume that the neutron is not changing its direction in the scattering process. Thus we can write for the net precession angle

$$\delta\alpha = -\gamma BL \left( \frac{1}{v} - \frac{1}{v'} \right) \quad (3.3)$$

and for the  $z$ -component of the polarization  $\langle\sigma_z\rangle = \cos(\delta\alpha)$

We further assume that the scattering is quasi elastic, meaning that the energy change of the neutron is very small, i.e.  $v' = v + \delta v$  with  $\delta v \ll v$ . The neutron energy transfer is defined by

$$\begin{aligned} \hbar\omega &= \frac{m}{2}(v^2 - v'^2) \\ &= \frac{m}{2}(v + v')(v - v') \\ &= \frac{m}{2}(2v - \delta v)(\delta v) \approx mv\delta v \end{aligned} \quad (3.4)$$

Hence we get for the total precession angle ( $B = B'$  and  $L = L'$ )

$$\begin{aligned} \delta\alpha &= \gamma BL \left( \frac{1}{v} - \frac{1}{v'} \right) = \gamma BL \left( \frac{1}{v} - \frac{1}{v + \frac{\hbar\omega}{mv}} \right) = \\ &\gamma BL \frac{\frac{\hbar\omega}{mv}}{v^2 + v\delta v} \approx \gamma BL \frac{\hbar}{mv^3} \omega = \tau\omega \end{aligned} \quad (3.5)$$

where the proportionality factor  $\tau$  between the net precession angle and the energy transfer has the dimension of time and is called spin echo time [Plo09]. It solely depends on the incident beam and the apparatus parameters. The physical meaning of this time becomes clear in the next section (3.1.2), when we consider each spin state individually. Not every neutron is for certain scattered with an energy transfer  $\hbar\omega$ , but rather with a probability  $S(\vec{q}, \omega)d\omega$  given by the scattering function  $S(\vec{q}, \omega)$  [Van54], where  $\vec{q}$  is the transverse momentum transfer. This probability needs to be taken into account when calculating the spin expectation value of a neutron beam at the end of the instrument. The measurable average value of  $\sigma_z$  is therefore given by

$$\langle \sigma_z \rangle = \int d\omega S(\vec{q}, \omega) \cos(\delta\alpha) = \int d\omega S(\vec{q}, \omega) \cos(\tau\omega) = F(\vec{q}, t = \tau) \quad (3.6)$$

this is the cosine Fourier transform of  $S(\vec{q}, \omega)$  with respect to  $\omega$ , which is called the intermediate scattering function  $F(\vec{q}, \tau)$  [Gäh+96]. In most scattering experiments  $S(\vec{q}, \omega)$  is measured, but in a spin echo experiment the cosine Fourier transform is encoded directly in the polarization.

Contrary to a SESANS setup (see section 3.3), NSE can only encode the energy transfer in the polarization. The former uses tilted magnetic field region to enable angle encoding as well.

### 3.1.2 Semi-Classical Approach

The underlying cause of Larmor precession is the interference of the coherent spin-up and spin-down states with slightly different momenta caused by the Zeeman splitting [Sud05]. In this approach we will treat each spin eigenstate individually, but assume classical trajectories through the setup.

In quantum mechanics a quantity is conserved if the according operator  $A$  commutes with the Hamiltonian  $H$ . The expectation value of  $A$  obeys  $\frac{d}{dt} \langle A \rangle = \frac{i}{\hbar} \langle [H, A] \rangle + \langle \frac{\partial A}{\partial t} \rangle$  (see equation 2.16 and e.g. [Sch07]). In the case of a DC-flipper the magnetic field is only dependent on position (upon entering and leaving) and we can show that the kinetic energy (and thus the momentum) as well as the potential energy changes, whereas the total energy (i.e. the frequency  $\omega$ ) is a conserved quantity. Moreover, because the Zeeman term  $-\vec{\mu} \cdot \vec{B}(\vec{x})$  has a dependency on the spin direction with respect to the magnetic field orientation, we get different dynamics for the two spin eigenstates  $|\uparrow\rangle$  and  $|\downarrow\rangle$ .

For the three aforementioned energies hold:  $\langle \frac{\partial}{\partial t}(-\frac{\hbar^2}{2m}\Delta) \rangle = \langle \frac{\partial}{\partial t}(-\vec{\mu} \cdot \vec{B}(\vec{x})) \rangle = \langle \frac{\partial H}{\partial t} \rangle =$

0. For the kinetic energy follows

$$\frac{d}{dt} \left\langle -\frac{\hbar^2}{2m}\Delta \right\rangle = \frac{i}{\hbar} \left\langle \left[ -\frac{\hbar^2}{2m}\Delta - \vec{\mu} \cdot \vec{B}(\vec{x}), -\frac{\hbar^2}{2m}\Delta \right] \right\rangle = -\frac{i\hbar^2}{4m} \gamma \vec{\sigma} \cdot \left\langle [\vec{B}(\vec{x}), \Delta] \right\rangle \neq 0 \quad (3.7)$$

and for the potential energy

$$\frac{d}{dt} \left\langle -\vec{\mu} \cdot \vec{B}(\vec{x}) \right\rangle = \frac{i}{\hbar} \left\langle \left[ -\frac{\hbar^2}{2m}\Delta - \vec{\mu} \cdot \vec{B}(\vec{x}), -\vec{\mu} \cdot \vec{B}(\vec{x}) \right] \right\rangle = -\frac{i\hbar^2}{4m} \gamma \vec{\sigma} \cdot \left\langle [\Delta, \vec{B}(\vec{x})] \right\rangle \neq 0 \quad (3.8)$$

For the total energy follows  $\frac{d}{dt} \langle H \rangle = \frac{i}{\hbar} \langle [H, H] \rangle = 0$  since the Hamiltonian is not explicitly time dependent. Hence the increase of the potential energy of the spin-up state must be compensated by a decrease of the kinetic energy (i.e. the momentum) and vice versa for the spin-down state. Furthermore, we can see from equation (3.7) and (3.8) that  $\frac{d}{dt} \langle E_{kin} \rangle = -\frac{d}{dt} \langle E_{pot} \rangle$ . We consider the incident beam to have energy  $E = \hbar\omega = \frac{mv^2}{2} = \frac{\hbar^2 k^2}{2m}$ . The wave function in the region of the magnetic field (after a  $\frac{\pi}{2}$  rotation) can be written as a superposition of up and down spin in  $z$ -eigenbasis [Sud05]

$$|\psi\rangle = \frac{1}{\sqrt{2}} e^{-i\omega t} \begin{pmatrix} e^{ik_{\uparrow}x} \\ e^{ik_{\downarrow}x} \end{pmatrix} \quad (3.9)$$

where  $k_{\uparrow}$  and  $k_{\downarrow}$  are the wave numbers for the spin-up and spin-down state respectively. They are given by  $k_{\uparrow} = k - \Delta k$  and  $k_{\downarrow} = k + \Delta k$ . The kinetic energy of the up state is  $E_{kin,\uparrow} = \frac{\hbar^2 k_{\uparrow}^2}{2m} = \frac{\hbar^2 k^2}{2m} - \mu B$ , with  $\mu B$  half the Zeeman splitting. We can thus write

$$\begin{aligned} \frac{\hbar^2}{2m} (k^2 - k_{\uparrow}^2) &= \mu B \\ \frac{\hbar^2}{2m} (k + k_{\uparrow})(k - k_{\uparrow}) &= \mu B \\ \frac{\hbar^2}{2m} (2k - \Delta k)(\Delta k) &= \mu B \end{aligned} \quad (3.10)$$

Since the change in energy between the two spin states induced by a magnetic field is small compared to the energy of the free incident neutron, we can approximate  $2k - \Delta k \approx 2k$  and write

$$\Delta k \approx \frac{\mu B m}{\hbar^2 k} \quad (3.11)$$

The kinetic energy of the down state is given by  $E_{kin,\downarrow} = \frac{\hbar^2 k_{\downarrow}^2}{2m} = \frac{\hbar^2 k^2}{2m} + \mu B$ . Moreover, since  $v = \frac{\hbar k}{m}$  also the velocity of the two spin eigenstates becomes distinct. According to equation (3.9) the different momenta will induce a difference in phase [GGK94].

Right after the first magnetic field ( $x = L$ ) the phases of the two spin states will be

$$\Phi_{\uparrow,\downarrow}^{(1)} = k_{\uparrow,\downarrow} L = \left( k \mp \frac{\mu B m}{\hbar^2 k} \right) L \quad (3.12)$$

Thus the phase difference between up-state and down-state is

$$\delta\Phi^{(1)} = \Phi_{\uparrow}^{(1)} - \Phi_{\downarrow}^{(1)} = -\frac{2\mu B m}{\hbar^2 k} L = -\frac{2\mu B}{\hbar v} L \quad (3.13)$$

We can also calculate the difference in arrival time between the spin eigenstates after a magnetic field region of length  $L$

$$\begin{aligned} t_{\uparrow} - t_{\downarrow} &= \frac{Lm}{\hbar(k - \frac{\mu B m}{\hbar^2 k})} - \frac{Lm}{\hbar(k + \frac{\mu B m}{\hbar^2 k})} = \\ &\frac{2Lm^2\mu B}{\hbar^3 k^3 - \hbar^3 \Delta k^2 k} \approx \frac{2Lm^2\mu B}{\hbar^3 k^3} = \frac{2L\mu B}{mv^3} = \tau \end{aligned} \quad (3.14)$$

The time  $\tau$  is again the spin echo time, but this time with the concrete physical meaning of the time delay between the spin states in a magnetic field. In a scattering experiment the spin eigenstates hit the sample with a time difference  $\tau$ . In the subsequently second field region of length  $L'$  and strength  $B'$  (with scattering: wave number  $k'$ ) the two states will pick up phases of

$$\Phi_{\uparrow,\downarrow}^{(2)} = k'_{\uparrow,\downarrow} L' = \left( k' \pm \frac{\mu B' m}{\hbar^2 k'} \right) L' \quad (3.15)$$

so the phase difference in the second region yields

$$\delta\Phi^{(2)} = \Phi_{\uparrow}^{(2)} - \Phi_{\downarrow}^{(2)} = \frac{2\mu B' m}{\hbar^2 k'} L' = \frac{2\mu B'}{\hbar v'} L' \quad (3.16)$$

Like in the previous section the phases  $\delta\Phi^{(1)}$  and  $\delta\Phi^{(2)}$  acquired in the two regions completely cancel if  $B = B'$ ,  $L = L'$  and  $v = v'$  then  $\delta\Phi^{(1)} + \delta\Phi^{(2)} = 0$ . Furthermore, the spatial separation of the spin eigenstates due to their different velocities becomes zero at the end of region 2 and they can interfere (spin echo), because the spin eigenstates of the same individual neutron are coherent.

The final  $-\frac{\pi}{2}$ -rotation will bring back the initial state if  $\delta\Phi^{(1)} + \delta\Phi^{(2)} = 0$ .

Also in this approach it can be shown that the polarization  $\langle \sigma_z \rangle$  is proportional to the intermediate scattering function  $F$ . We want to write the wave function  $|\psi\rangle$  after it passed through both field regions and is scattered by a sample. If assume that the  $|\uparrow\rangle$  ( $|\downarrow\rangle$ ) state scatters at position  $\vec{r}_i$  ( $\vec{r}_j$ ) and time  $t_i$  ( $t_j$ ) we get with the energy  $\omega$  and the scattering vector  $\vec{q}$  [Gäh+96]

$$|\psi\rangle = \frac{1}{\sqrt{2}} e^{i(\vec{k}' \cdot \vec{x} - \omega t)} \begin{pmatrix} e^{i\omega t_i} e^{-i\vec{q} \cdot \vec{x}_i} \rho(\vec{x}_i, t_i) e^{i\omega\tau/2} \\ e^{i\omega t_j} e^{-i\vec{q} \cdot \vec{x}_j} \rho(\vec{x}_j, t_j) e^{-i\omega\tau/2} \end{pmatrix} \quad (3.17)$$

where  $\rho(\vec{x}, t)$  is the density of the scattering system and the exponentials containing  $\vec{q}$  and  $\omega$  account for the momentum and energy transfer respectively.



We can now calculate the  $z$ -component of the polarization by

$$\langle \psi | \sigma_z | \psi \rangle = \frac{1}{2} \int d^3 x_i \int d^3 x_j \int dt_i \int dt_j \int d\omega e^{-i\vec{q} \cdot (\vec{x}_i - \vec{x}_j)} \langle \rho(\vec{x}_i, t_i) \rho(\vec{x}_j, t_j) \rangle e^{i\omega(\tau + t_i - t_j)} + c.c \quad (3.18)$$

Since the detection mechanism is not able to resolve different energies, we must consider all energies and have to integrate over  $\omega$ . This integration (i.e. Fourier transform of a constant) just gives a Dirac Delta function  $\delta(\tau + t_i - t_j)$ . Furthermore, we set  $\vec{x}_j = \vec{x}_i + \vec{X}$  and get

$$\langle \sigma_z \rangle = \frac{1}{2} \int d^3 X \left[ \int dt_i \int d^3 r_i \langle \rho(\vec{x}_i, t_i) \rho(\vec{x}_i + \vec{X}, t_i + \tau) \rangle \right] e^{i\vec{q} \cdot \vec{X}} + c.c \quad (3.19)$$

for the polarization. The term in the squared bracket is exactly the density-density correlation function  $G(\vec{X}, \tau)$ , which relates the density at  $\vec{x}_i$  and  $t_i$  with that at  $\rho(\vec{x}_i + \vec{X}$  and  $t_i + \tau)$ . So the polarization reads

$$\langle \sigma_z \rangle = \frac{1}{2} \int d^3 X G(\vec{X}, \tau) e^{i\vec{q} \cdot \vec{X}} + c.c \quad (3.20)$$

This expression is the spatial Fourier transform of  $G(\vec{X}, \tau)$ . It can be shown that this is proportional to the intermediate scattering function  $F(\vec{q}, \tau)$  [Van54]. Hence

$$\langle \sigma_z \rangle \sim \int d^3 X G(\vec{X}, \tau) e^{i\vec{q} \cdot \vec{X}} \sim F(\vec{q}, \tau) \quad (3.21)$$

In conclusion, we have also shown in this semi-classical picture that the measured polarization is proportional to the cosine Fourier transform of the scattering function, hence the intermediate scattering function.

A full quantum mechanical treatment, where the beam is given by a wave packet and the individual trajectories of the spin eigenstates are analysed quantum mechanically, can be found in [Gäh+96].

## 3.2 Neutron Resonant Spin Echo (NRSE)

The basic idea and experimental setup of neutron resonant spin echo (NRSE) is the same as for ordinary neutron spin echo (NSE). The main difference is the usage of time dependent magnetic fields (section 2.3.2 and 2.3.3), which leads to neutron-photon interaction. A first theoretical description appeared in 1987 by Gähler and Golub [GG87].

The underlying principle of NRSE is *zero field precession*, where Larmor precession seemingly occurs in a region with zero magnetic field [Spo+08]. Zero field precession is enabled by neutron-photon interaction, when the neutron gains (or loses) energy due to photon absorption (or emission). This interaction can not appear in static magnetic fields like DC-flipper, but needs time dependent fields as in an RF flipper.

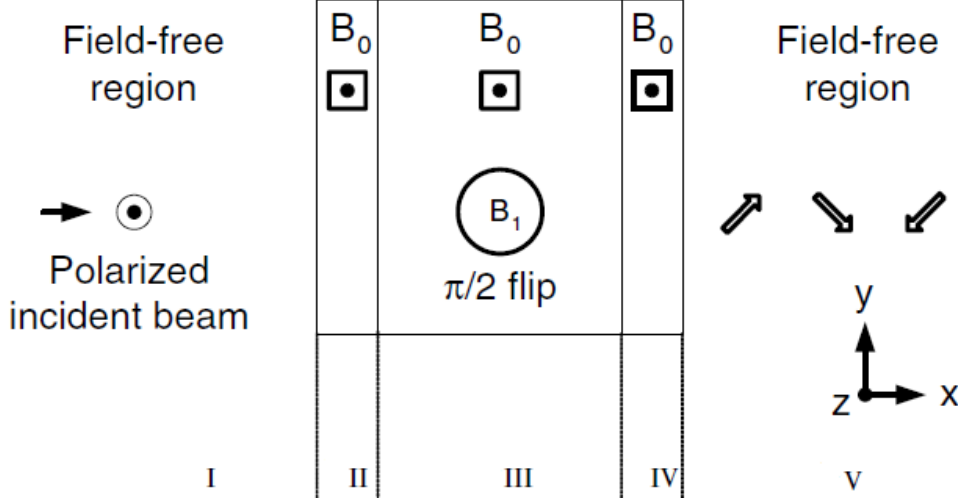


Figure 3.2: Idealized magnetic field configuration of a resonant RF flipper set to a  $\frac{\pi}{2}$  rotation as described in section 2.3.2. The neutron beam is propagating in  $x$ -direction and is initially polarized in  $z$ -direction. The flipper is divided into five areas labelled I to V. **I**: Field free region and no precession. **II**: Sharp transition to a static magnetic field  $B_0$  in  $z$ -direction. **III**: An additionally RF field rotates the polarization vector by  $\frac{\pi}{2}$ . **IV**: Same magnetic field as in region II thus inducing no change of the polarization. **V**: Upon exiting, the inverse procedure of entering the static field occurs, leading to a precessing polarization vector in a field free region. Adapted from [Sud05].

We start with a classical picture of Larmor precession and consider an RF field as sketched in figure (3.2). The flight path of the neutron is divided into five sections (I to V). The neutron beam is propagating in  $x$ -direction and is initially polarized in  $z$ -direction ( $\vec{P}_I = \hat{z}$ ). The magnetic field in region II is pointing in  $z$ -direction, thus using equation (2.23) we can write  $\vec{P}_{II} = e^{iL_z(\gamma B_0 \frac{x_{II}}{v})} \vec{P}_I = \vec{P}_I$ , where  $B_0$  is the magnitude of the static field,  $x_{II}$  the length of the region and  $v$  the velocity of the neutron. We again neglect possible reflection due to the transition from region I to II.

In region III an oscillating magnetic field is superimposed on the  $B_0$  field (see (2.27)). The solution of the polarization in such a field in the rotating wave approximation and for frequency resonance is given by equation (2.35)

$$\vec{P}(t_1) = e^{iL_z(\gamma B_0 t_1)} e^{iL_x \alpha(t_1)} \vec{P}(0) \quad (3.22)$$

where  $\alpha(t_1) = \gamma \frac{B_1}{2} t_1$  is the angle the polarization vector is rotated and  $t_1$  is the time the neutron spends in the RF flipper. In this case we set the RF flipper to  $\pi/2$  mode, i.e.  $\alpha(t_1) = \frac{\pi}{2}$ , which results in the following polarization after the RF field

$$\vec{P}_{III} = e^{iL_z(\gamma B_0 t_1)} e^{iL_x \frac{\pi}{2}} \vec{P}_{II} = e^{iL_z(\gamma B_0 t_1)} e^{iL_x \frac{\pi}{2}} \hat{z} \quad (3.23)$$

The polarization vector in region IV does not change since the static field is still present, therefore  $\vec{P}_{IV} = \vec{P}_{III}$ . Upon exiting the static field in region IV, due to the RF

field, the opposite procedure happens as for entering the static magnetic field. Instead of a rotation  $e^{iL_z(\gamma B_0 \frac{x}{v})}$  we get  $e^{-iL_z(\gamma B_0 \frac{x}{v})}$ . This explanation becomes more vivid in the next section, when the two spin states are investigated in more detail (3.2.1). Hence the polarization in region V is given by

$$\vec{P}_V = e^{-iL_z(\gamma B_0 \frac{x}{v})} \vec{P}_{IV} = e^{-iL_z(\gamma B_0 \frac{x}{v})} e^{iL_z(\gamma B_0 t_1)} e^{iL_x \frac{\pi}{2}} \hat{z} = e^{iL_z \gamma B_0 (t_1 - \frac{x}{v})} \hat{y} \quad (3.24)$$

If we write the rotation around  $z$  in the terms of sine and cosine we get

$$\vec{P}_V = \begin{pmatrix} \sin(\gamma B_0 (t_1 - \frac{x}{v})) \\ -\cos(\gamma B_0 (t_1 - \frac{x}{v})) \\ 0 \end{pmatrix} \quad (3.25)$$

We can see that the precession angle of the polarization vector after the flipper has a spatial dependency (and time dependency  $\frac{x}{v} = t$ ) as if a magnetic field in  $z$ -direction is present. This ongoing precession in a region of no magnetic field is called *Zero Field Precession* (ZFP).

Another way to achieve ZFP with an RF flipper is to set  $\alpha(t_1)$  to a  $\pi$ -flip and have the incoming beam polarized perpendicular to the  $B_0$  field (i.e. in the  $x$ - $y$ -plane) by a DC-flipper beforehand. The polarization vector in region V ( $\vec{P}_{V,\pi}$ ) is then

$$\vec{P}_{V,\pi} = \begin{pmatrix} \sin(\gamma B_0 (t_1 - 2\frac{x}{v})) \\ \cos(\gamma B_0 (t_1 - 2\frac{x}{v})) \\ 0 \end{pmatrix} \quad (3.26)$$

It is apparent that the precession in this case is twice as fast as in the previous case. Moreover, it seems like a magnetic field of  $2B_0 \hat{z}$  is present after the flipper [GGK94]. This stems from the fact that one spin state absorbs the energy while the other emits that same energy, which leads to the double energy difference and double the precession frequency. In  $\pi/2$  mode only one state absorbs or emits energy. In the case of a  $\pi$ -flip the neutron is absorbing (emitting) twice the energy from the electromagnetic field compared to a  $\frac{\pi}{2}$  rotation.

Considering the whole NRSE instrument, one spin echo arm exists of two identical RF flippers, where the first one starts the zero field precession and the second one stops it. Zero field precession only occurs between the two RF flippers, but not at the sample position. The second arm of the spin echo setup would again be a mirrored version of the first. Solely the static fields of the RF flipper  $B_0$  point in the opposite direction. A major advantage of NRSE over NSE is the potential to achieve higher Larmor frequencies in the spin echo arms, without the need of long homogenous magnetic field regions. These are hard to realise and potential inhomogeneities lower the resolution. However, it is easier to implement static magnetic field than RF fields with high frequencies. For that reason current NSE instruments have higher energy resolution at the moment than NRSE instruments.

### 3.2.1 Semi Classical Approach

Similar to section 3.1.2 we now want to look at energy changes of the spin eigenstates in the same time dependent magnetic field  $\vec{B}(t)$  as given in (2.39). We use the Heisenberg equation for the time derivative of the expectation values (equation (2.16)). The expectation value of the kinetic energy of a neutron in such a field is a conserved quantity since

$$\frac{d}{dt} \left\langle -\frac{\hbar^2}{2m} \Delta \right\rangle = \frac{i}{\hbar} \left\langle \left[ -\frac{\hbar^2}{2m} \Delta - \vec{\mu} \cdot \vec{B}(t), -\frac{\hbar^2}{2m} \Delta \right] \right\rangle + \left\langle \frac{\partial}{\partial t} \left( -\frac{\hbar^2}{2m} \Delta \right) \right\rangle = 0 \quad (3.27)$$

where  $-\frac{\hbar^2}{2m} \Delta - \vec{\mu} \cdot \vec{B}(t) = H$  is the Hamiltonian of the system. Needless to say, the total energy of the neutron is not conserved since the Hamiltonian is explicitly time dependent because of  $\vec{B}(t)$

$$\frac{d}{dt} \langle H \rangle = \left\langle \frac{\partial}{\partial t} \left( -\frac{\hbar^2}{2m} \Delta - \vec{\mu} \cdot \vec{B}(t) \right) \right\rangle \neq 0 \quad (3.28)$$

By absorption or emission of a photon from the RF field the total energy of the neutron is increased or decreased. In the case of a spin flip (i.e. rotation by  $\pi$ ,  $|\uparrow\rangle \rightarrow |\downarrow\rangle$ ) the energy of the neutron alters by  $2\mu B_0$ . The condition for frequency resonance gives us  $\omega_{\text{rf}} = \gamma B_0$  and the energy change becomes  $2\mu B_0 = \hbar \omega_{\text{rf}}$ , thus equal to the energy of a photon with frequency  $\omega_{\text{rf}}$  [ABR81]. Since the kinetic energy remains unchanged, the change in total energy manifests in a change of the potential energy by the same value with opposite sign. For the potential energy holds

$$\frac{d}{dt} \langle -\vec{\mu} \cdot \vec{B}(t) \rangle = \frac{i}{\hbar} \left\langle \left[ -\frac{\hbar^2}{2m} \Delta - \vec{\mu} \cdot \vec{B}(t), -\vec{\mu} \cdot \vec{B}(t) \right] \right\rangle + \left\langle \frac{\partial}{\partial t} (-\vec{\mu} \cdot \vec{B}(t)) \right\rangle = \left\langle \frac{\partial}{\partial t} (-\vec{\mu} \cdot \vec{B}(t)) \right\rangle \neq 0 \quad (3.29)$$

A graphical summary of the energy changes is depicted in figure (3.3). As described in section (3.1.2) the different momenta of the eigenstates being in a coherent superposition lead to Larmor precession.

We now want to describe the evolution of the wave function of the neutron through a resonant RF flipper given in figure (3.2). The initial wave function of a neutron propagating in  $x$ -direction and polarized in  $z$  in the field free region I is given by

$$|\psi\rangle_{\text{I}} = e^{ikx} e^{-i\omega t} |\uparrow\rangle \quad (3.30)$$

with wave number  $k$  and energy  $\hbar\omega = \frac{\hbar^2 k^2}{2m}$ .

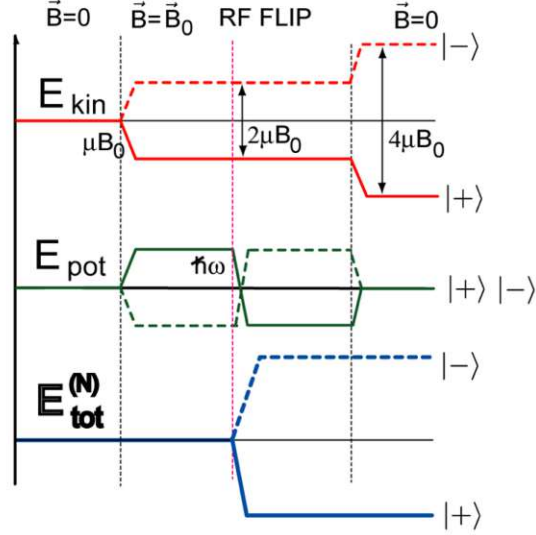


Figure 3.3: Energy diagrams in case of  $\pi$ -flip by a resonant RF flipper as indicated in figure (3.2). Upon entering a static field the kinetic and the potential energy changes, whereas the total energy remains constant. The time dependent field induces a  $\pi$ -flip and the potential energy as well as the total energy change. Upon exiting the flipper the potential energy changes again, while the total energy does not. This leads to an additional change in kinetic energy. After the RF flipper the two spin eigenstates exhibit an energy difference of  $4\mu B_0 = 2\hbar\omega_{\text{rf}}$ . From [Has+10].

When it enters a static magnetic field (region II) the wave number is changed (see equation 3.9) and we get

$$|\psi\rangle_{\text{II}} = e^{ik_{\uparrow}x} e^{-i\omega t} |\uparrow\rangle \quad (3.31)$$

where  $k_{\uparrow} = k - \Delta k$  and  $\Delta k$  given by (3.11)). Next the neutron goes through an RF flipper of frequency  $\omega_{\text{rf}} = \gamma B_0$ , which is set to a  $\frac{\pi}{2}$ -rotation. The wave function at the end of region III is (equation (2.41) and [Spo+12])

$$|\psi\rangle_{\text{III}} = \frac{1}{\sqrt{2}} e^{ik_{\uparrow}x} e^{-i\omega t} \left[ e^{-i\omega_{\text{rf}}t_1/2} |\uparrow\rangle - i e^{i\omega_{\text{rf}}t_1/2} |\downarrow\rangle \right] \quad (3.32)$$

where  $t_1$  the time the neutron spends in region III. In region IV the wave function does not change, therefore  $|\psi\rangle_{\text{IV}} = |\psi\rangle_{\text{III}}$  [Sud05]. Upon leaving a static field (region IV) the up-state and the down-state gain a phase factor of  $e^{i\Delta k x}$  and  $e^{-i\Delta k x}$  respectively, which is the opposite of entering a static magnetic field. The wave function in the last region reads

$$|\psi\rangle_{\text{V}} = \frac{1}{\sqrt{2}} e^{ikx} e^{-i\omega t} \left[ e^{-i\omega_{\text{rf}}t_1/2} |\uparrow\rangle - i e^{i\omega_{\text{rf}}t_1/2} e^{-i2\Delta k x} |\downarrow\rangle \right] \quad (3.33)$$

The kinetic energies of the up-state and down-state in region V are  $E_{\text{kin},\uparrow} = \frac{\hbar^2 k^2}{2m} - \mu B_0$  and  $E_{\text{kin},\downarrow} = \frac{\hbar^2 k^2}{2m} + \mu B_0$ , hence the difference amounts to  $2\mu B$ . The same holds

for the total energy since there is no potential in region V. The polarization vector after the flipper is

$$\vec{P}_V = \langle \psi |_V \vec{\sigma} | \psi \rangle_V = \begin{pmatrix} \sin(\gamma B_0 t_1 - 2\Delta kx) \\ -\cos(\gamma B_0 t_1 - 2\Delta kx) \\ 0 \end{pmatrix} \quad (3.34)$$

In this zero field region,  $\vec{P}_V$  is still precessing with a spatially dependent phase  $\gamma B_0 t_1 - 2\Delta kx$ . If we compare this result with the polarization vector obtained by classical derivation (equation 3.25), we can see that  $2\Delta kx = \gamma B_0 \frac{x}{v}$ . It shows again that the altered momenta of the spin eigenstates is the underlying cause of Larmor precession.

To achieve ZFP with twice the Larmor frequency one initially needs a superposition of spins of the form  $|\psi\rangle = \frac{1}{\sqrt{2}} e^{ikx} e^{-i\omega t} (|\uparrow\rangle + |\downarrow\rangle)$ , which is obtained after a DC-Coil. Additionally, the subsequent RF flipper must be set to a  $\pi$  flip. This leads to a difference in kinetic and total energy of the spin states of  $4\mu B_0$  (see figure 3.3) and further to a polarization vector of

$$\vec{P}_{V,\pi} = \langle \psi |_V \vec{\sigma} | \psi \rangle_V = \begin{pmatrix} \sin(\gamma B_0 t_1 - 4\Delta kx) \\ -\cos(\gamma B_0 t_1 - 4\Delta kx) \\ 0 \end{pmatrix} \quad (3.35)$$

with a phase of  $4\Delta kx$ . This method to generate ZFP is for example used in [Spo+10]. As the energy difference between the ground state and these excited states is very small (4 MHz is already very high), the rate for spontaneous emission is very low (e.g. [Dem10]) and can be neglected.

### 3.3 Spin Echo Small Angle Neutron Scattering (SESANS)

The main goal at a small angle neutron scattering (SANS) experiment is the investigation of the structure of a sample by measuring scattered neutrons at small angles. Combining this with a spin echo setup by placing the sample between the two magnetic field arms, one gets a spin echo small angle neutron scattering (SESANS) instrument as introduced in [Kel+95; Rek96]. Such instruments are able to resolve structures smaller than the divergence of the neutron beam, which is the limiting factor of SANS.

Up until now we have studied NSE setups with perpendicular field boundaries with respect to the neutron beam. The necessary novelty at a SESANS setup are titled magnetic field regions. We have seen in equation (3.1) that the summed precession angle  $\delta\alpha$  depends on the time  $t = \frac{L'}{v}$  the neutron spends in the magnetic field and consequently the length  $L'$  of the field region. If the neutron is scattered elastically from a sample, the path of the neutron will vary in the second arm compared to the first one. Hence, the precession in the second arm will not cancel the precession gained in the first and

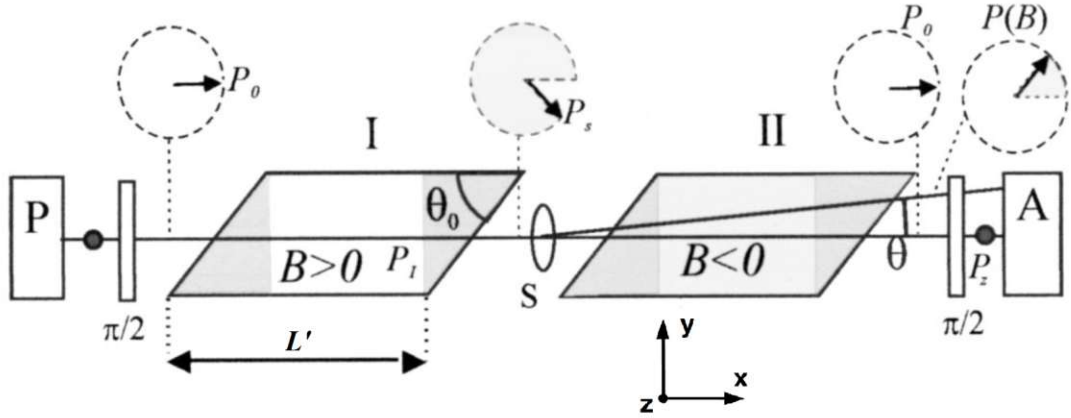


Figure 3.4: Setup of a SESANS instrument. The neutron beam is travelling in positive  $x$ -direction. Firstly, it gets polarized by the polariser P, followed by a  $\frac{\pi}{2}$  rotation. The resulting polarization vector  $P_0$  is pointing in  $x$ -direction. The parallelogram-shaped magnetic field of region I is pointing in  $z$  and forms an angle  $\theta_0$  with the beam direction. Larmor precession occurs along the path  $L'$ , after which the polarization is  $P_s$ . If the neutron does not scatter from the sample S, the precession of the first field is cancelled in region II (magnetic field pointing in opposite direction) and after the  $\frac{\pi}{2}$  rotation the polarization is pointing in  $z$  again ( $P_z$ ). A neutron scattering from the sample by an angle  $\theta$  has a different path length through the magnetic field region II compared to region I. Thus, the  $\frac{\pi}{2}$  rotation does not recover the initial polarization but is  $P(B)$ . Finally, the polarization is analysed by a spin analyser A. From [Rek+05].

therefore decreases the polarization. By tilting the field regions this effect is amplified and becomes measurable to first order in tilting angle  $\theta_0$ .

We want to study a SESANS setup as depicted in figure (3.4). We consider a neutron beam propagating in  $x$ -direction and polarized in  $z$ -direction parallel to the direction of the magnetic fields. A sample S is placed between two parallelogram-shaped magnetic field regions, which are tilted in such a way that the neutron beam hits the field region at an angle  $\theta_0 \neq \frac{\pi}{2}$ . The path length through the first field region is  $L' = \frac{L}{\sin(\theta_0)}$ , where  $L$  is the minimal normal distance inside the parallelograms (see figure 3.5). If the neutron does not interact with the sample the path length in the second region would be  $L_2' = L'$  and the net precession  $\delta\alpha$  is equal to zero, i.e. the echo condition is met. If the neutron scatters elastically (no change in velocity) from the sample at an angle  $\theta$ , the path length of the neutron in the second field region will be different and  $\delta\alpha \neq 0$ .

In order to calculate the phase difference we will consider the problem geometrically. We can write the phase acquired in the first region as

$$\alpha_1 = \frac{\gamma B}{v} L' = \frac{\gamma B}{v} \frac{L}{\sin(\theta_0)} \quad (3.36)$$

where  $B$  is the magnetic field strength and  $v$  the velocity of the neutron. We consider a small angle scattering event, similar to the small velocity change due to quasi elastic scattering at the NSE (equation 3.4). The neutron is deflected by an angle  $\theta$  from the

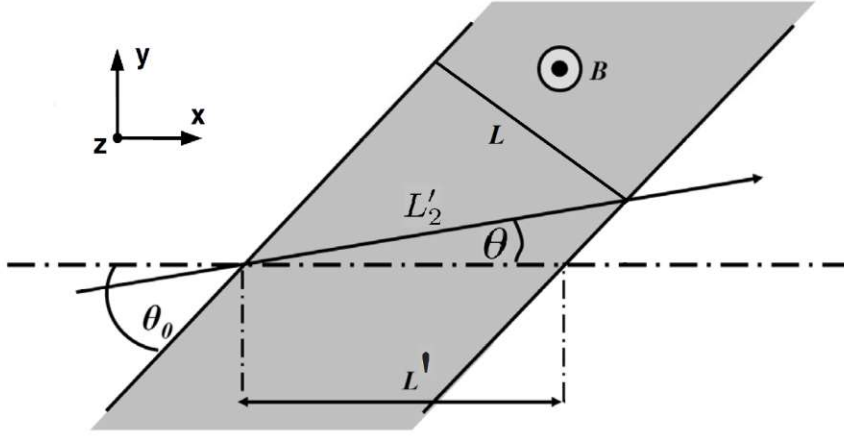


Figure 3.5: Sketch of the neutron trajectories through a skew magnetic field region, tilted by an angle  $\theta_0$ . The path length in the first region is  $L'$  and in the second field region  $L'_2$ , caused by small angle scattering from the sample by an angle  $\theta$ . Adapted from [Plo09].

sample, therefore changing the angle between the neutron flight path and the normal of the parallelogram to  $\theta_2$  which is equal to  $\theta_2 = \theta_0 - \theta$  (figure 3.5).

The phase acquired in the second region is thus

$$\alpha_2 = -\frac{\gamma B}{v} L'_2 = -\frac{\gamma B}{v} \frac{L}{\sin(\theta_2)} \quad (3.37)$$

This yields for the net precession  $\delta\alpha = \alpha_1 + \alpha_2 = \frac{\gamma B}{v} L \left( \frac{1}{\sin(\theta_0)} - \frac{1}{\sin(\theta_2)} \right)$ . We can expand  $\delta\alpha$  in a Taylor series around  $\theta_0 = \theta_2$  and write the first two terms as

$$\delta\alpha \approx [\delta\alpha]_{\theta_0=\theta_2} + \left[ \frac{d}{d\theta_2} (\delta\alpha) \right]_{\theta_0=\theta_2} \cdot (\theta_0 - \theta_2) \quad (3.38)$$

The first term vanishes and the second gives

$$\delta\alpha = \frac{\gamma B}{v} \frac{L}{\sin(\theta_0)} \cot(\theta_0) \theta = \frac{\gamma B}{v} L' \cot(\theta_0) \theta \quad (3.39)$$

The absolute value of the momentum transfer for small angles  $\theta$  is given by  $|q| = q_y = k_0 \theta$ , where  $k_0$  is the wave vector of the incoming neutron [Brü05]. The net precession becomes

$$\delta\alpha = \frac{\gamma B}{v k_0} L' \cot(\theta_0) q_y = \delta_{\text{NSE}} q_y \quad (3.40)$$

The proportionality constant  $\delta_{\text{NSE}}$  has the dimension of length and is called the spin echo length [Plo09]. It is given by

$$\delta_{\text{NSE}} = \frac{\gamma B}{v k_0} L' \cot(\theta_0) \quad (3.41)$$

A concrete physical meaning can be attributed to the quantity  $\delta_{\text{NSE}}$  if the two spin states are viewed individually, which will be done in the next section (see 3.3.1). The measured polarization is reduced by scattering since  $\langle \sigma_z \rangle = \cos(\delta\alpha) = \cos(\delta_{\text{NSE}} q_y)$ . Taking into account the probability of scattering given by the scattering function  $S(\vec{q}, \omega)$



and considering only elastic scattering where  $\omega = 0$  we end up with (compare with equation 3.6)

$$\langle \sigma_z \rangle = \int dq_y S(\vec{q}) \cos(\delta_{\text{NSE}} q_y) = G(\delta_{\text{NSE}}) \quad (3.42)$$

which is again the cosine Fourier transform of the scattering function, but this time with respect to the momentum transfer  $\vec{q}$ . The function  $G(\delta_{\text{NSE}})$  is the density-density correlation function.

Due to the first order approximation we did during this derivation, the spin echo length  $\delta_{\text{NSE}}$  becomes 0 if  $\theta_0 = \frac{\pi}{2}$ , even though the path length in the second region would be different. But the effect is not visible in first order for such small scattering angles. In consequence of the tilted coils, a SESANS instrument can encode the scattering angle in the measured polarization.

### 3.3.1 Semi-Classical Approach

As in the previous sections (3.1.2 and 3.2.1) we will again treat the spin of the neutron quantum mechanically but its trajectory classically. As indicated in figure (3.4), the polarized neutron is rotated by  $\frac{\pi}{2}$  such that the resulting wave function is given by a superposition as

$$|\psi\rangle = \frac{1}{\sqrt{2}} e^{-i\omega t} e^{ik_0 x} [|\uparrow\rangle + |\downarrow\rangle] \quad (3.43)$$

where the quantisation axis is chosen in  $z$ -direction in accordance with the orientation of the magnetic field. From equation (2.59) we know that the index of refraction depends on the potential  $V$  of the field region. Furthermore, the potential is given by  $V = \gamma \frac{\hbar}{2} \vec{\sigma} \cdot \vec{B}$ , therefore depends on the orientation of the spin with respect to the magnetic field. Hence, there will be different indices of refraction for the two spin states, which will also be refracted in different directions. In a static magnetic field the kinetic energy changes along with the potential energy. Furthermore, the wave vector changes by  $\Delta k$ , thus  $k_{\uparrow, \downarrow} = k_{+, -} = k \mp \Delta k$  with  $\Delta k \approx \frac{\mu B m}{\hbar^2 k} = \frac{\gamma B}{2v}$ , where  $v$  is the initial velocity in free space (see section 3.1.2). For the case of tilted field regions it is the component normal to the field boundary  $k_{\perp}$  that experiences the change  $\Delta k$ , where as the component parallel  $k_{\parallel}$  to it remains unchanged [Plo09]. A sketch of this situation is depicted in figure (3.6).

We can write the components of the initial wave vector as  $k_{0\perp} = k_0 \sin(\theta_0)$  and  $k_{0\parallel} = k_0 \cos(\theta_0)$ . The angles  $\theta_+$  and  $\theta_-$  are defined as deviation from the initial propagation direction. From geometric consideration we find for the ratio of parallel to perpendicular component

$$\cot(\theta_0 + \theta_{\pm}) = \frac{k_0 \cos(\theta_0)}{k_0 \sin(\theta_0) \mp \frac{\gamma B}{2v \sin(\theta_0)}} \quad (3.44)$$

where the denominator is the  $k_{\pm\perp}$ . Since  $\Delta k$  is small compared to the wave vector of the free neutron, the angles  $\theta_{\pm}$  will be small as well. If one expands the left hand side

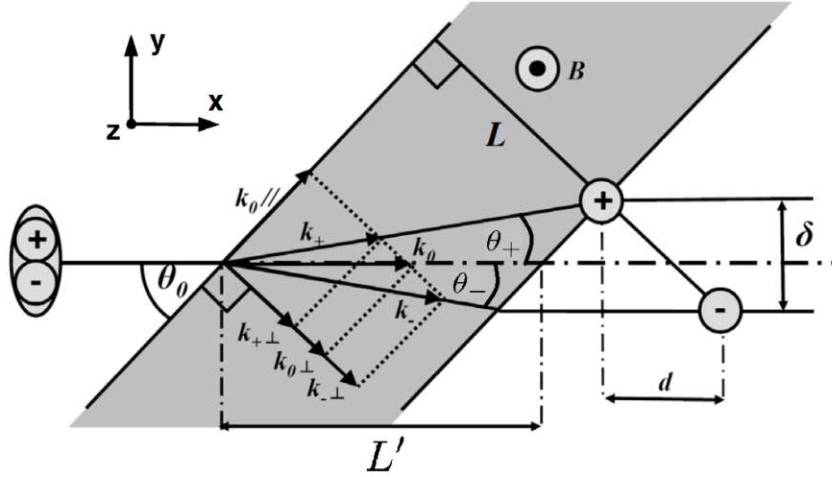


Figure 3.6: Semi classical view of a neutron passing through a tilted magnetic field. The incoming neutron is in a spin superposition of  $|+\rangle$  and  $|-\rangle$ . Upon entering the field, the component of the wave vector parallel to the magnetic field boundary  $k_{0\parallel}$  remains unchanged but the perpendicular component  $k_{\perp}$  changes differently for  $|+\rangle$  and  $|-\rangle$ . Hence, the two spin states are refracted by different angles  $\theta_+$  and  $\theta_-$ . On leaving the magnetic field the initial wave vector  $k_0$  is restored and the spin travel parallel to each other but with a displacement  $\vec{r}_+ - \vec{r}_- = d\hat{x} + \delta\hat{y}$ , where  $\delta$  is the spin echo length and  $d$  caused by the spin echo time. Adapted from [Plo09].

of equation (3.44) to first order in  $\theta_{\pm}$ , we find  $\cot(\theta_0 + \theta_{\pm}) \approx \cot(\theta_0) - \frac{1}{\sin^2(\theta_0)}\theta_{\pm}$ . For the right hand side we find  $\frac{k_0 \cos(\theta_0)}{k_0 \sin(\theta_0)} \pm \frac{k_0 \cos(\theta_0)}{k_0^2 \sin^2(\theta_0)} \frac{\gamma B}{2v \sin(\theta_0)} = \cot(\theta_0) \pm \cot(\theta_0) \frac{\gamma B}{vk_0 \sin^2(\theta_0)}$  to first order in  $\Delta k$ . This yields for the angles  $\theta_{\pm}$

$$\theta_{\pm} = \mp \frac{\gamma B}{2vk_0} \cot(\theta_0) \quad (3.45)$$

When the spin states leave the magnetic field region, the initial wave vector  $k_0$  will be restored and the eigenstates will travel parallel to each other, but with an relative displacement of  $\delta$  (see figure 3.6). The separation of the two spin eigenstates  $\delta$  in  $y$ -direction to first order in  $\theta_{\pm}$  can be written as [Gäh+96]

$$\delta = L'(\theta_+ - \theta_-) = \frac{\gamma B}{vk_0} L' \cot(\theta_0) = \delta_{\text{NSE}} \quad (3.46)$$

which is exactly the proportionality factor we derived in equation (3.41) only this time it emerges as a real distance. In addition to the spatial shift in  $y$ -direction we get a shift in  $x$ -direction called  $d$ , which is proportional to the spin echo time  $\tau$  (see equation 3.14) and reads  $d = v\tau$ .

The phase of the spin-up and spin-down wave function after passing through the first magnetic field region is

$$\Phi_{+,-}^{(1)} = k_{\perp}^{\pm} L_{\perp}^{\pm} + k_{\parallel}^{\pm} L_{\parallel}^{\pm} \quad (3.47)$$

For the  $k$ -vectors the following relationships hold:  $k_{\parallel}^{\pm} = k_{0\parallel} = k_0 \cos(\theta_0)$  and  $k_{\perp}^{\pm} = k_0 \sin(\theta_0) \mp \frac{\gamma B}{2v \sin(\theta_0)}$ . For the path length  $L_{\parallel}^{\pm} = L \cot(\theta_0 + \theta_{\pm})$  and  $L_{\perp}^{\pm} = L = L' \sin(\theta_0)$ .

With the approximation for  $\cot(\theta_0 + \theta_{\pm})$  we get for the phase difference of the two spin states due to the different paths and momenta

$$\Phi_+^{(1)} - \Phi_-^{(1)} = -\frac{\gamma BL}{v \sin(\theta_0)} + \frac{\gamma BL}{v \sin(\theta_0)} \cot^2(\theta_0) \quad (3.48)$$

In addition, there will also arise a phase shift from the path difference  $d$  (figure 3.6), which is  $\Phi_d = k_0 \delta_{\text{NSE}} \cot(\theta_0) = \frac{\gamma BL}{v \sin(\theta_0)} \cot^2(\theta_0)$ . Thus the total phase difference between the spin states after the first region and for the same  $x$ -coordinate ( $x_{\uparrow} = x_{\downarrow}$ ) is

$$\delta\Phi^{(1)} = \Phi_+^{(1)} - \Phi_-^{(1)} - \Phi_d = \frac{\gamma BL}{v \sin(\theta_0)} = \frac{\gamma BL}{v} L' \quad (3.49)$$

Likewise, in this model the echo condition is fulfilled if no scattering from the sample occurs. Then the phase difference acquired in the second magnetic field region is  $\delta\Phi^{(2)} = -\delta\Phi^{(1)}$ , yielding equal phases after region II for both spin states. In the case of scattering from a sample S at an angle  $\theta$  we can calculate its effect on the phase difference as in equation (3.38) and get

$$\delta\Phi_s \approx \left[ \frac{d}{d\theta_2} (\delta\Phi^{(1)}) \right] \cdot \theta = \frac{\gamma B}{v} L' \cot(\theta_0) \theta = \delta_{\text{NSE}} q_y \quad (3.50)$$

where  $q_y$  is the momentum transfer. This result is in accordance with the classical derivation in (3.40). The up-state and the down-state impinge on the sample at positions  $\vec{r}_i$  and  $\vec{r}_j$  respectively.

To calculate the polarization  $\langle \sigma_z \rangle$  in  $z$ -direction at the analyser position we write the corresponding wave function as [Gäh+96]

$$|\psi\rangle = \frac{1}{\sqrt{2}} e^{i(kx - \omega t)} \begin{pmatrix} e^{-i\vec{q}\cdot\vec{r}_i} \rho(\vec{r}_i) e^{-iq_y \delta_{\text{NSE}}/2} \\ e^{-i\vec{q}\cdot\vec{r}_j} \rho(\vec{r}_j) e^{iq_y \delta_{\text{NSE}}/2} \end{pmatrix} \quad (3.51)$$

In case of elastic scattering the  $z$ -polarization is given by

$$\langle \psi | \sigma_z | \psi \rangle = \frac{1}{2} \int d^3 r_i \int d^3 r_j \int d^3 q \rho(\vec{r}_i) \rho(\vec{r}_j) e^{i\vec{q}\cdot(\vec{r}_i - \vec{r}_j)} e^{iq_y \delta_{\text{NSE}}} + c.c. \quad (3.52)$$

The  $y$  component of  $(\vec{r}_i - \vec{r}_j)$  cancels with  $q_y \delta_{\text{NSE}}$  and from the integration over  $q_x$  and  $q_z$  we obtain delta functions, meaning that the points  $\vec{r}_i$  and  $\vec{r}_j$  must have equal  $x$  and  $z$  components. It follows for  $\langle \sigma_z \rangle$

$$\langle \sigma_z \rangle \sim \int dr_i \rho(\vec{r}_i) \rho(\vec{r}_i + \delta_{\text{NSE}} \cdot \hat{y}) \sim G(\delta_{\text{NSE}}) \quad (3.53)$$

By probing the sample with two neutron beams, we can relate the density at position  $\vec{r}_i$  with that at  $\vec{r}_i + \delta_{\text{NSE}} \cdot \hat{y}$ . The measured polarization is proportional to the density-density correlation function as we derived also classically in section (3.3).

# Chapter 4

## Spin Chopping System

In this chapter the first of two experimental approaches is described. It focuses on a chopping system based on spin manipulation to enable time of flight measurements and consequently a flipping technique with time dependent RF amplitudes as described in section (2.3.4). A similar setup has been implemented in [Tak+11]. Another common technique for chopping is to utilise a fast rotating disc with a diameter of 0.5 – 1 m, which is placed in the beam. Usually it has two diametrically opposed window zones, where neutrons can pass [Brü05], thus producing a pulsed beam and enabling TOF. Nevertheless, these discs need a lot of space and cannot achieve chopping frequencies as high as a spin chopping system.

### 4.1 Experimental Setup and Preparation

An illustration of the entire setup is depicted in figure (4.1). The neutron beam is propagating from right to left. In this convention, the first three components are a field stepper, a resonant RF flipper with square pole shoes and a supermirror, which together make the spin chopping system. Latter is flipped along the longitudinal axis, such that it is polarizing the beam in opposite direction compared to the supermirror inside the concrete shielding (not visible in figure 4.1). In theory, if no flip occurs between these two supermirrors, the entire beam would be absorbed in the second supermirror. Unfortunately, supermirrors possess strong magnetic stray fields, which are in this particular configuration also twisted with respect to each other. They are pointing in opposite directions, one in  $z$  one in  $-z$ . From this, adiabatic field transitions in between the mirrors arise, which lead to unwanted adiabatic static spin rotations. To prevent this, a field stepper is placed after the first supermirror. A photograph can be seen in figure (4.2).

The field stepper generates a magnetic field parallel to the stray field of the first supermirror on the one side and a field parallel to the second supermirror (i.e. antiparallel to the first) on the other side. At the maximal current of 6 A the field stepper can produce a highly non-adiabatic jump in magnetic field along the flight path of 4.3 mT.

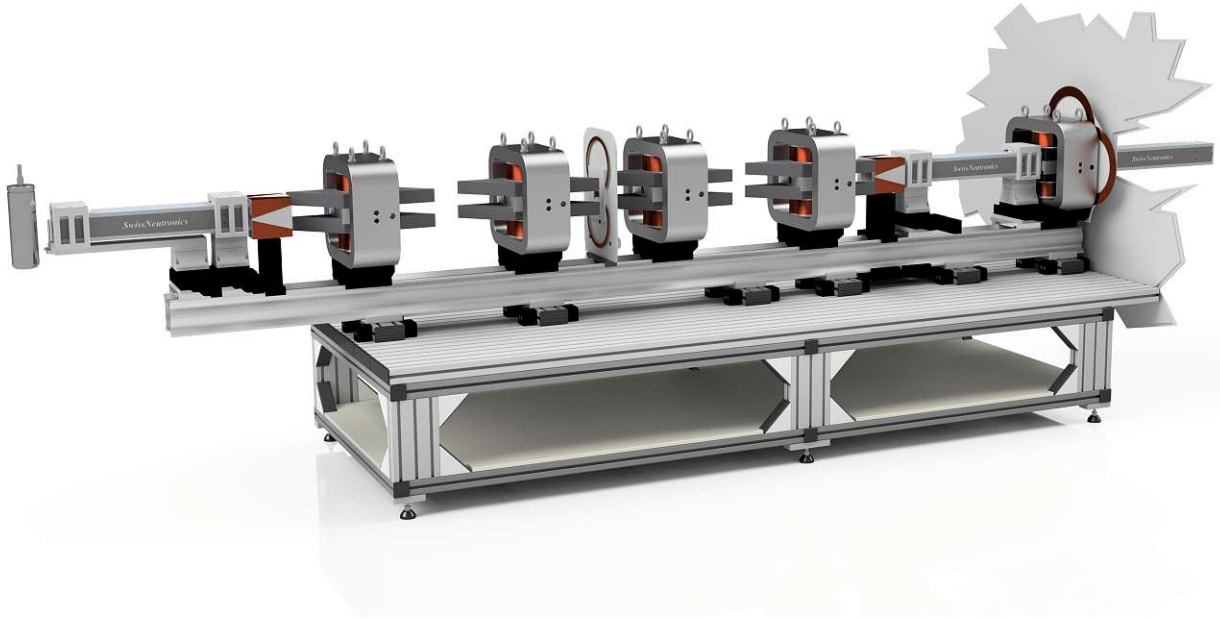


Figure 4.1: Proposed setup for the SESANS instrument. The neutrons enter the setup from the right and are initially polarized by the first supermirror inside the concrete shielding. The next three components are part of the spin chopping system (see text). The next component is a V-coil responsible for superimposing the two spin states. What follows is the first arm of the SESANS instrument, consisting of two RF flipper with parallelogram-shaped pole shoes. A field stepper is separating the two spin echo arms. The next two magnets form the second spin echo arm and are the counterpart of the first. The penultimate component is another V-coil for rotating the spins back into the initial direction, followed by a spin analyser, consisting of a supermirror and the detector.

The subsequent resonant RF flipper has a yoke made out of industrial steel. The  $B_0$  field is generated by a coil with iron core and square pole shoes made out of iron as well (see figure 4.3a). A similar setup has been used in [Gee+19]. The pole shoes help to focus the magnetic field and create sharp field boundaries. In between the pole shoes a solenoid shaped coil induces an oscillating RF field in beam direction. It is 40 mm in length, 24 mm in diameter, has 16 windings and is wound with a 2 mm copper wire. The entire RF coil is embedded in an aluminium box (see figure 4.3b), in order to prevent RF radiation from disturbing the neutron detector and induce false counts.

The RF coil is operated in pulsed mode. The amplitude resonance condition for a  $\pi$  flip is given by  $B_1 = \frac{2\pi}{\gamma t_p}$ , where  $t_p$  is the time the neutron is exposed to the RF field. If the transit time  $t_t$  of the neutrons through the RF coil is significantly larger than the pulse duration and the amplitude of the RF field  $B_1$  is large enough, the amplitude resonance condition is fulfilled for all neutrons in the coil, independent of their wavelength. Only those neutrons, which enter or exit the RF coil during a

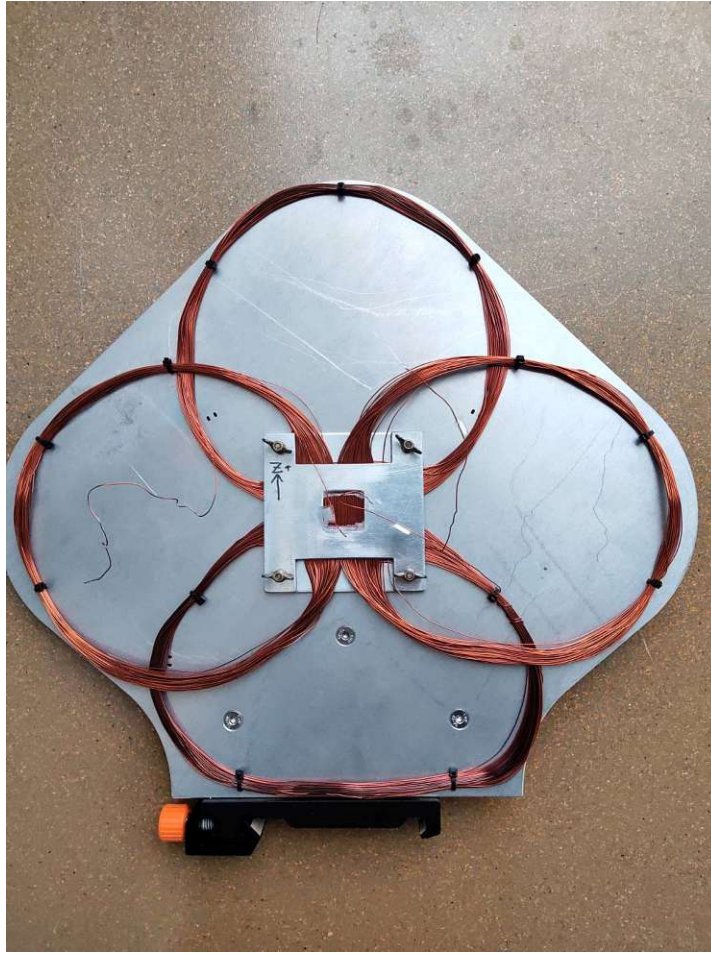


Figure 4.2: Field stepper as used in all spin chopping experiments consisting of two separate circuits in shapes of eights. Only the upright loop was used. According to the right hand rule, a current perpendicular to the beam direction is inducing a magnetic field in  $\pm z$  direction. Neutrons go through the center window, which is covered by the copper wire. Heat production is limiting the current at about 6 A. At this current, the field stepper can produce a highly non-adiabatic jump in magnetic field along the flight path of 4.3 mT.

pulse will not be flipped. The pulse duration was aimed to be one tenth of the transit time of the fastest neutrons. Subsequently, all flipped neutrons will be reflected in the supermirror, whereas all others will be absorbed. Hence, the resulting neutron beam is pulsed and TOF is enabled. The RF signal is generated by the arbitrary function generator AFG1062 from  $\text{\textcircled{R}}$ Tektronix with a frequency range from  $1 \mu\text{Hz}$  to 60 MHz for sine waves. It has two output channels each into  $50 \Omega$  loads and two operation modes, continuous mode and burst mode. The output peak-peak voltage has a range of 1 mV to 10 V. The burst duration is given in cycles ( $1$  to  $10^6$ ), i.e. in multiples of the period of the sine wave. For example at  $f = 4 \text{ MHz}$ , 8 cycles last for  $8 * 0.25 \mu\text{s} = 2 \mu\text{s}$ . The signal is then amplified by the broadband power amplifier 1040L from  $\text{\textcircled{R}}$ Electronics & Innovation.

The DC-current source for the  $B_0$ -coil is the power supply ES030-10 from  $\text{\textcircled{R}}$ DELTA



(a) Rendered image of the RF flipper used for the spin chopping system. The  $B_0$  field is produced by a copper coil with iron core. The aluminium box in between the iron pole shoes is shown in figure (4.3b).

(b) Rendered image of the aluminium housing and the RF coil. The coil is wound on bobbin made out of PEEK and the end plates are made out of aluminium. The inside length in flight direction is 121.5 mm, the height is 25 mm. The port on the right side are suitable for BNC connectors and coax cables.

Figure 4.3

ELEKTRONIKA, with a maximum current output of 10 A. This produces a magnetic field of 160 mT, which corresponds to  $\omega = 2\pi f = 29.32$  MHz (frequency resonance). Moreover, the spin echo length must be greater than the transversal coherence length of the neutron beam in order to manipulate the two spin states separately. The transversal coherence length  $\sigma_T$  can be approximated by geometrical considerations. It is equal to the wavelength of the largest allowed transverse momentum of a neutron that can still be detected. For small angles one can write  $\sigma_T = \frac{2\pi}{k_0\theta}$ , where  $k_0$  is the magnitude of wave vector of the fastest neutrons in the spectrum and  $2\theta$  is the maximum possible spread of the beam. This can be calculated by  $\theta = \frac{d_2+d_1}{D}$ , with  $d_2$  the width of the entry slit of the polariser,  $d_1$  the width of the entry slit of the analyser and  $D$  the distance between those in beam direction. Assuming the wavelength of the fastest neutrons to be  $\lambda = 3.25$  Å and further  $d_1 = 3$  mm,  $d_2 = 8$  mm and  $L = 3$  m, the transversal coherence length yields  $\sigma_T = 88$  nm. Furthermore does the spin echo length scale with the  $B_0$  field. To achieve high versatility the aim was to set the angular frequency to almost maximum value of  $\omega = 25.13$  MHz, i.e. a frequency of  $f = 4$  MHz, resulting in a spin echo length of  $\delta_{\text{NSE}} = 1.068$  μm.

## Electronics

From the electrical engineering point of view it has to be consider that the RF coil

is not a purely ohmic resistor but has a frequency dependent impedance  $Z_l$  given by

$$Z_l = R_l + i\omega L_l \quad (4.1)$$

where  $R_l$  is the ohmic resistance,  $\omega$  the angular frequency of the AC voltage and  $L_l = \frac{\mu_0 N^2 A}{L}$  the inductance of the RF coil ( $N$  the number of windings,  $A$  the cross-section area and  $L$  the length of the coil). In figure (4.4) the circuit diagram of the setup is depicted, where  $R_{load} = R_l$  and  $L_{load} = L_l$ . In order to minimize reflections and maximize the power output at the load, the impedances of the source, cable and load have to be identical for all frequencies, i.e. have to be matched. The imaginary part of the impedance can be matched by adding capacitors  $C_1$ ,  $C_{21}$ ,  $C_{22}$  and  $C_{23}$  to the circuit. Since their impedance is given by  $Z_C = -i\frac{1}{\omega C}$  ( $C$  is the capacitance of the capacitor), the imaginary part of the load can be cancelled.

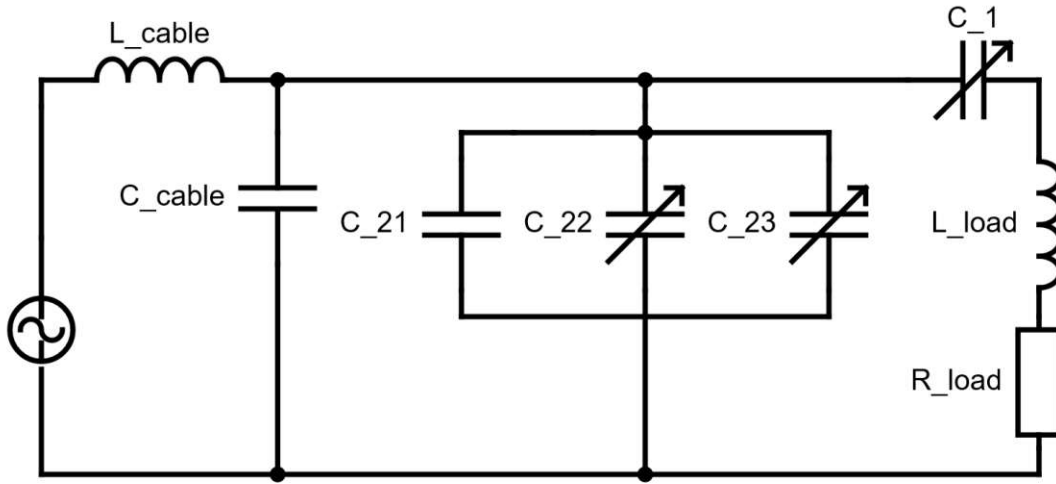


Figure 4.4: Circuit diagram of the spin chopping system. The RF coil has an inductance  $L_{load}$  and a resistance  $R_{load}$ . The source consists of the function generator and the power amplifier. The cable is assumed to be lossless. Capacitors  $C_1$  and  $C_2 = C_{21} + C_{22} + C_{23}$  are responsible for impedance matching at an arbitrary frequency.

If we assume a lossless coaxial cable, the impedance of the cable  $Z_0$  can be calculated by  $Z_0 = \frac{L_{cable}}{C_{cable}}$  and is by design  $50\Omega$  and already matched to the source. To match the load to the cable we apply Kirchoff's loop law to the right loop in figure (4.4) and get

$$\frac{1}{Z_l} = i\omega C_2 + \frac{1}{R_l + i(\omega L_l - \frac{1}{\omega C_1})} \quad (4.2)$$

with  $C_2 = C_{21} + C_{22} + C_{23}$ . The circuit is matched if  $\text{Re}(Z_l) = Z_0$  and  $\text{Im}(Z_l) = 0 \Rightarrow \text{Im} \frac{1}{Z_l} = 0$ . These two conditions lead to two equations for the capacitances  $C_1$  and  $C_2$ , which read [Coo14]

$$C_1(\omega) = \frac{1}{\omega(\omega L_l - \sqrt{R_l(Z_0 - R_l)})} \quad (4.3)$$

$$C_2(\omega) = \frac{1}{\omega Z_0} \sqrt{\frac{Z_0 - R_l}{R_l}} \quad (4.4)$$



A numerical calculation of the important parameters of the circuit and the setup can be seen in table (4.1). From a given coil, frequency and beam spectrum all other quantities were derived. The estimation of the fastest neutrons was done via the tilting angle of the very first supermirror inside the concrete shielding and was assumed to be  $\lambda = 2 \text{ \AA}$ .

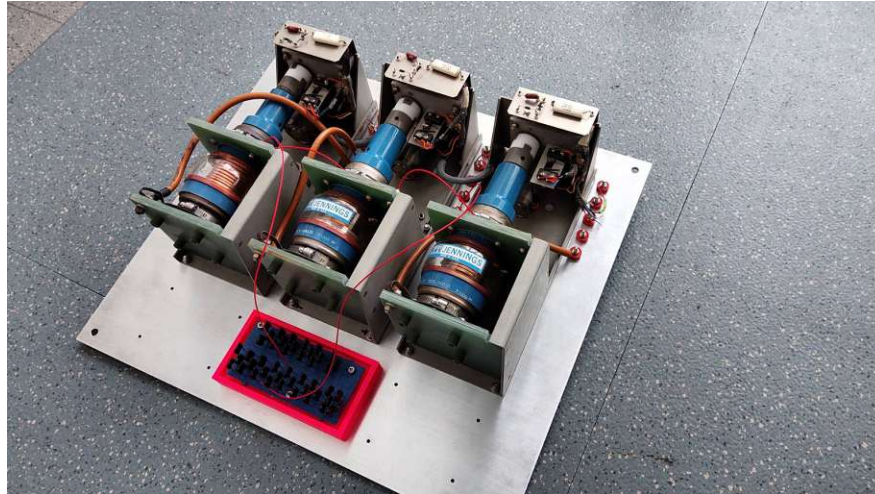
Due to the high frequency the skin effect has to be taken into account. Eddy currents increase the resistivity inside of the copper wire and reduce the effective cross section. At the skin depth  $\delta$  (measured from the surface) the current has only  $1/e$  of its maximum outer surface value. This effect increases the resistance of the load  $R_l$ .

Furthermore, from table (4.1) it can be seen that the voltage at the capacitor  $C_1$  can become very high,  $V_1 = 2.99 \text{ kV}$ . Hence, it requires capacitors with breakdown voltages. Three identical tunable vacuum capacitors were used for  $C_1$ ,  $C_{22}$  and  $C_{23}$  with a breakdown voltage of  $3 \text{ kV}$  and capacitance of  $7 - 1000 \text{ pF}$ . To reach the demanded capacitance of  $C_2 = 15.725 \text{ nF}$  a set of fixed capacitors  $C_{21}$  should be added in parallel to  $C_{22}$  and  $C_{23}$  in order to increase to overall capacitance. The proposed configuration is shown in figure (4.6a). All capacitors used for  $C_{21}$  are identical with a breakdown voltage of  $1 \text{ kV}$  and capacitance of  $1 \text{ nF}$ . The configuration was designed such that the breakdown voltage of  $C_{21}$  matches the one of  $C_{22}$  and  $C_{23}$ . Furthermore, the current through one individual capacitor is reduced by this arrangement. To screen RF radiation, every capacitor is placed in an aluminium box (see figure 4.5), from which coax cable lead to the amplifier and the RF coil.

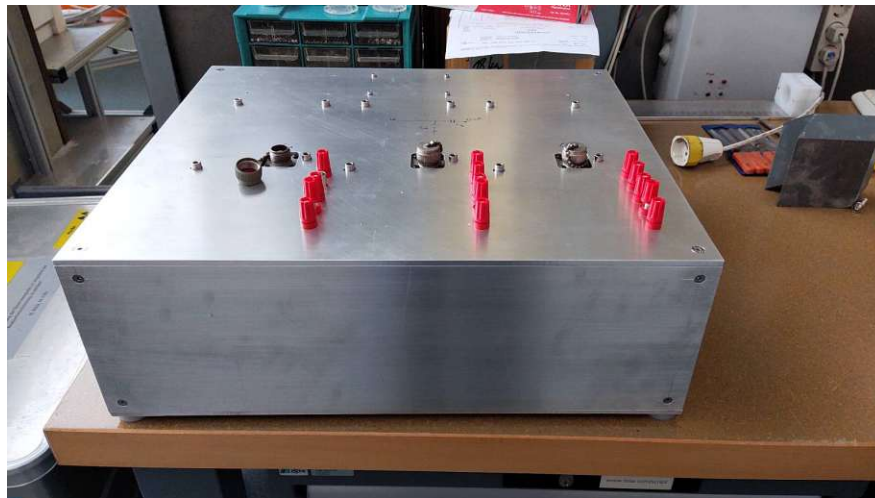
From the amplitude resonance condition one can calculate the necessary magnetic field amplitude  $B_1$  and the amplitude of the corresponding current  $I$ . The amplitude of the necessary AC power at the load is  $P = 136.28 \text{ W}$ , hence an effective power of  $136.28/2 = 68.14 \text{ W}$  for sinusoidal signals. The amplifiers maximum effective power output is  $400 \text{ W}$  in continuous mode, which is equivalent to an amplitude of  $800 \text{ W}$ . This is enough to achieve the desirable power in pulsed mode.

characteristic impedance	$Z_0$		$50 \Omega$
frequency	$f$		4 MHz
smallest wavelength of beam spectrum	$\lambda$		$2 \text{ \AA}$
fastest neutrons of beam spectrum	$v$	$v = \frac{h}{\lambda m}$	$1978 \frac{\text{m}}{\text{s}}$
length of coil	$l$		40 mm
diameter of coil	$d$		24 mm
transit time	$t_t$	$t_t = \frac{v}{l}$	$20.22 \mu\text{s}$
pulse duration	$t_p$	$t_p = \frac{t_t}{10}$	$2.022 \mu\text{s}$
number of windings	$N$		16
diameter of wire	$d_w$		1.6 mm
length of wire	$l_w$	$l_w = \pi d N$	1.2 m
skin depth	$\delta$	$\delta = \sqrt{\frac{2}{\mu_0(\chi+1)\sigma 2\pi f}}$	0.033 mm
effective cross section of wire	$A_w$	$A_w = (\frac{d_w}{2})^2 \pi - (\frac{d_w}{2} - \delta)^2 \pi$	$0.1626 \text{ mm}^2$
resistance of load	$R_l$	$R_l = \frac{\rho l_w}{A_w}$	$0.1277 \Omega$
cross section area of coil	$A$	$A = (\frac{d}{2})^2 \pi$	$452.39 \text{ mm}^2$
inductance of load	$L_l$	$L_l = \frac{\mu_0 N^2 A}{l}$	$3.6365 \mu\text{H}$
capacitance at impedance matching	$C_1$	$C_1 = \frac{1}{\omega(\omega L_l - \sqrt{R_l(Z_0 - R_l)})}$	$0.44771 \text{ nF}$
capacitance at impedance matching	$C_2$	$C_2 = \frac{1}{\omega Z_0} \sqrt{\frac{Z_0 - R_l}{R_l}}$	$15.725 \text{ nF}$
amplitude of magnetic field for $\pi$ flip	$B_1$	$B_1 = \frac{2\pi}{\gamma t_p}$	$16.96 \text{ mT}$
amplitude of AC current at load	$I$	$I = \frac{B_1 l}{\mu_0 N}$	$33.75 \text{ A}$
magnitude of the impedance of the capacitor 1	$Z_{C1}$	$Z_{C1} = \frac{1}{2\pi f C_1}$	$88.87 \Omega$
magnitude of the impedance of the capacitor 2	$Z_{C2}$	$Z_{C2} = \frac{1}{2\pi f C_2}$	$2.53 \Omega$
amplitude of voltage at $C_1$	$V_1$	$V_1 = Z_{C1} \cdot I$	$2.99 \text{ kV}$
magnitude of impedance of $C_1$ and $L_l$ and $R_l$	$Z_{tot}$	$Z_{tot} = \sqrt{(2\pi f L_l - \frac{1}{2\pi f C_1})^2 + R_l^2}$	$2.527 \Omega$
amplitude of voltage at $C_2$	$V_2$	$V_2 = Z_{tot} \cdot I$	$85.28 \text{ V}$
amplitude of power during a pulse at load	$P$	$P = I^2 \cdot R_l$	$136.28 \text{ W}$

Table 4.1: Theoretical calculation of parameters for the spin chopping system. Here  $h$  is the planck constant,  $m$  the mass of the neutron,  $\mu_0$  is the permeability of vacuum,  $\chi$  the magnetic susceptibility of copper,  $\sigma$  the conductivity of copper,  $\rho$  the resistivity of copper and  $\gamma$  the gyromagnetic ratio.



(a)



(b)

Figure 4.5: (a) Capacitors used for impedance matching. The three vacuum capacitors ( $C_1$ ,  $C_{22}$  and  $C_{23}$ ) are tunable, whereas the small capacitors ( $C_{21}$ ) are static and connected as in figure (4.6b). (b) The aluminium shielding with connectors for the capacitors of (a).

A first experimental attempt with the values of the capacitances given in table (4.1) failed. In continuous mode, no resonance was found at 4 MHz and the forward power at the amplifier was equal to the reflected power. One reason for this are possible parasitic capacitances or inductances in the circuit. Another are elevated resistance values arising from electrical contacts and real losses in the cable. After analysing the circuit with a vector network analyser the fixed capacitors  $C_{21}$  were reduced to 5 nF (see figure 4.6b) and the resonance frequency was found at  $f = 3.910933$  MHz. With these values the reflected power become 1 W at a forward power of 20 W. This translates to a ratio of  $10 * \log(\frac{1}{20}) = -29.96$  dB.

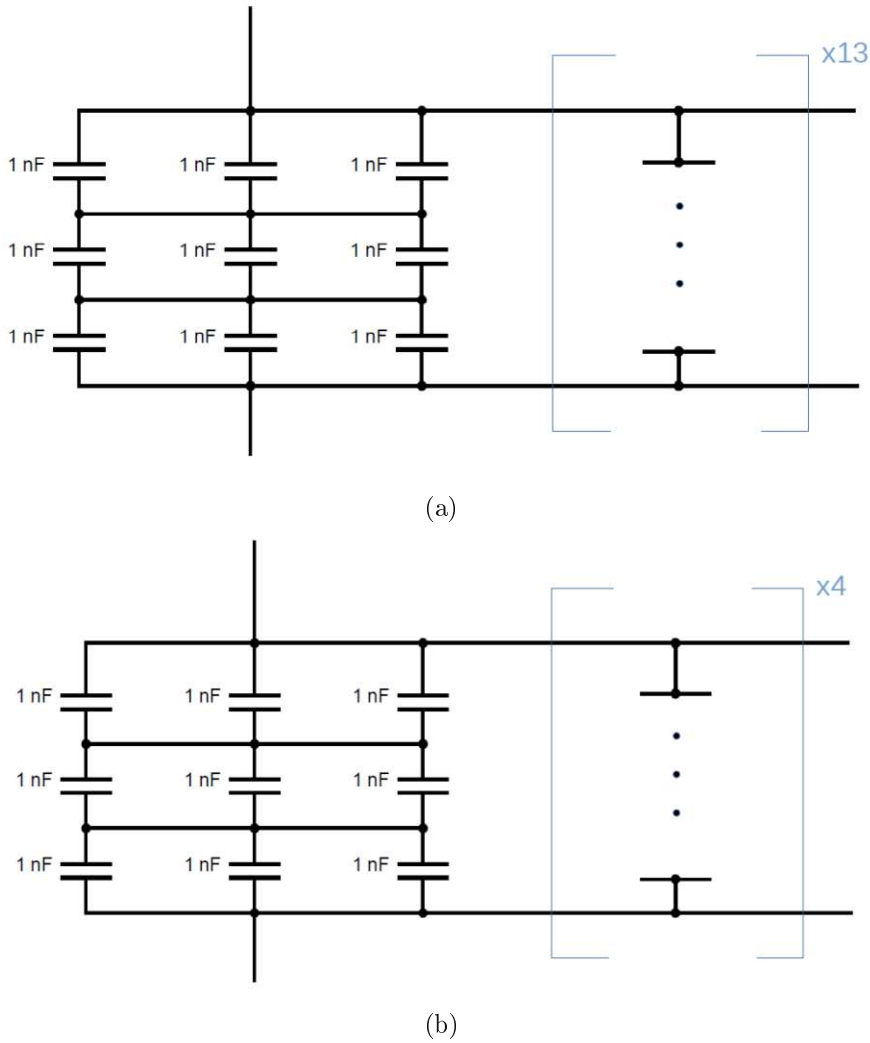


Figure 4.6: Circuit diagram of the capacitance  $C_{21}$ . The block of capacitors shown explicitly has 1 nF and a breakdown voltage of 3 kV. Identical copies are connected in parallel to increase the total capacitance. (a) Proposed configuration after theoretical calculations ( $C_{21} = 14$  nF). (b) Configuration after vna measurements and how it is used in further experiments ( $C_{21} = 5$  nF).

## 4.2 Results

The following measurements and results focus only on the spin chopping system. The magnets of the SESANS setup were turned off at all times.

First the supermirror that is part of the spin chopping system has to be aligned. Out of the two incident neutron beams we solely want to work with the polarized one. In addition we want the intensity to be as high as possible. The degree of polarization is determined through the shim intensity given by  $I_{\text{shim}} = (I_z^+ + I_z^-) / 2$ . The degree of polarization becomes  $P = 1 - I_z^- / I_{\text{shim}}$ . The shim intensity was measured by placing an iron plate in front of the supermirror. The plate absorbs and depolarizes the neutrons from the beam. For the measurement of  $I_z^-$  the iron plate was placed

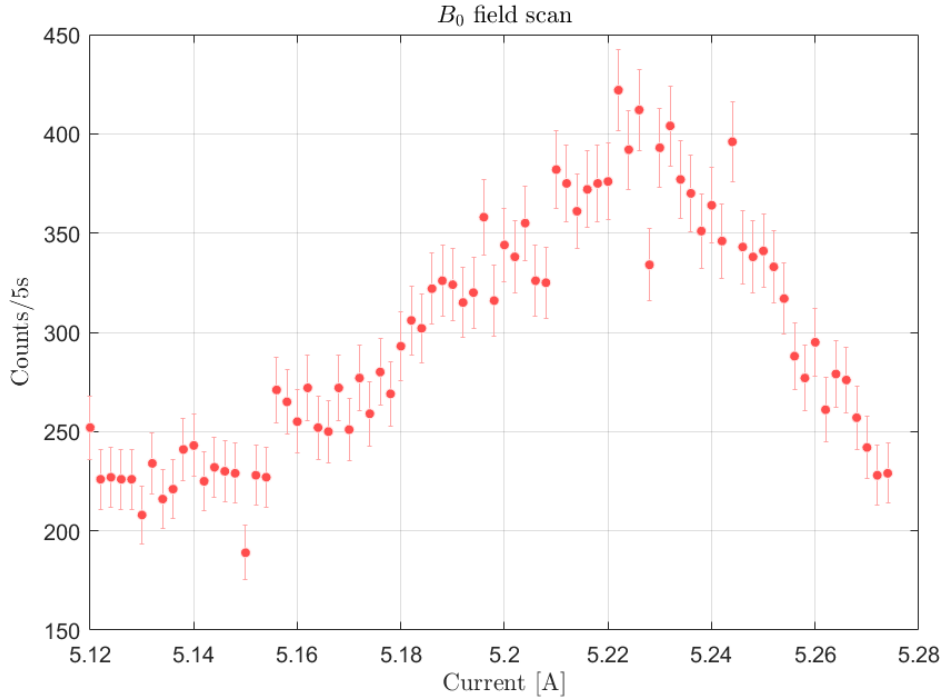


Figure 4.7: Current scan of the  $B_0$  magnet versus neutron counts. The oscillating magnetic field of the RF flipper was continuous at a frequency  $f = 3.910933$  MHz. Since the two supermirrors are oriented oppositely the neutron counts increase when the frequency resonance condition is met and spins start to rotate. The maximal count rate was found at  $I = 5.222$  A.

after the supermirror to account for absorption and thus making the two intensities comparable. For both measurements the current through the field stepper was set to  $I_{\text{FS}} = 6$  A and the RF flipper was completely switched off. At the optimal position the intensities obtained in 30 s were  $I_z^- = 514$  and  $I_{\text{shim}} = 5320$ , which gives  $P = 0.903$ .

Before starting a TOF measurement the frequency resonance condition has to be found. For this the frequency of the RF field was set to the resonance frequency of the electric circuit, i.e.  $f = 3.910933$  MHz, and the function generator to continuous mode with a peak-peak voltage of  $V_{p-p} = 200$  mV. Next, the current  $I$  in the  $B_0$ -coil was scanned. The result is plotted in figure (4.7). At the current with maximum count rate, the most spins were rotated and the static magnetic field corresponds to  $f = 3.910933$  MHz. Frequency resonance was found at  $I = 5.222$  A. A measurement to acquire the optimal oscillating magnetic field amplitude  $B_1$  necessary for a  $\pi$  flip cannot be conducted in continuous mode, but needs time-of-flight measurements. Different TOF spectra have to be recorded with varying output voltage  $V_{p-p}$  from the function generator, thus varying  $B_1$ . Moreover, the pulse duration  $t_p$  needs to be changed accordingly. For each measurement the signal-to-noise ratio is calculated, which is an indication of the flip efficiency of the RF flipper.

For the acquisition of the TOF spectrum depicted in figure (4.8) the following parameter setting was applied:  $I$  and  $f$  as aforementioned, pulse duration  $t_p = 30$  cycles,

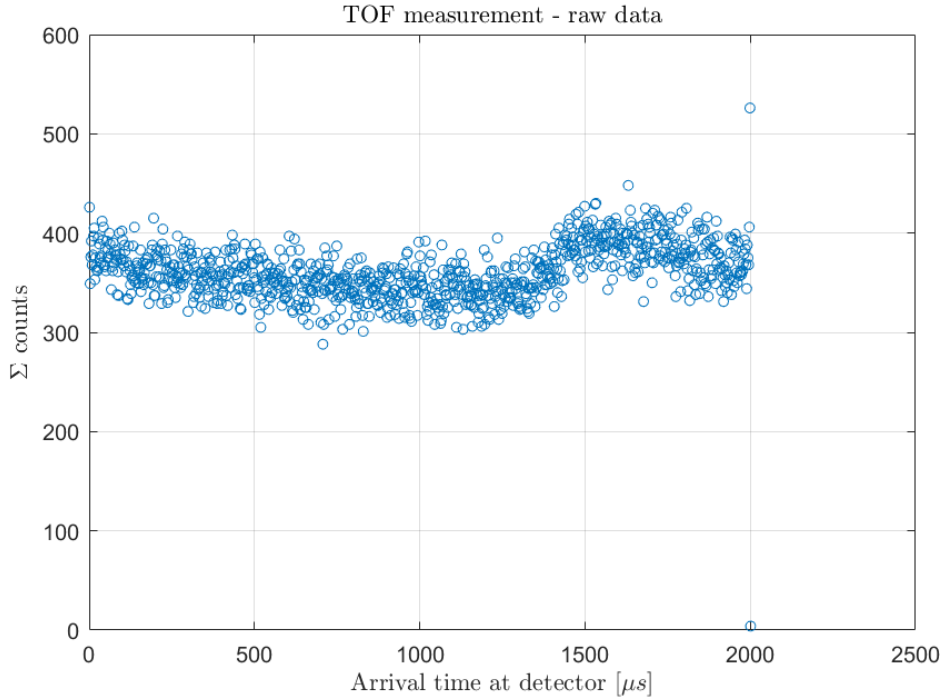


Figure 4.8: Measured time-of-flight spectrum with  $f = 3.910933$  MHz,  $t_p = 30$  cycles,  $V_{p-p} = 820$  mV,  $t_f = 2$  ms, total measurement time of 1 h and 200 kW reactor power. On the x-axis the arrival time at the detector after the start of the RF pulse is plotted. The intensities of each frame were summed. One can see higher count rates for very short arrival times, which is an indication of frame overlap.

$V_{p-p} = 820$  mV, the current of the field stepper  $I_{FS} = 6$  A. The duration of one frame (that is the time between two subsequent pulse starts) is  $t_f = 2$  ms, thus 500 Hz. The entire measurement was running for one hour at a reactor power of 200 kW. The TOF spectrum has a resolution of  $2 \mu\text{s}$  and the neutron counts were summed over all frames, but keeping track of the associated arrival times.

Apart from the high background and the low signal-to-noise ratio (SNR), one can see that more neutrons arrive at the detector between 0-500  $\mu\text{s}$  than between 500-1000  $\mu\text{s}$  indicating a lot of very fast neutrons in the spectrum. The distance between the RF flipper and the detector is 1.86 m. If the neutron arrival time is 0.5 ms the corresponding velocity is 3720 m/s and the wavelength is 1.06 Å. This is unphysical since supermirrors will cut off the spectrum at a certain maximum velocity. The plausible explanation is frame overlap, where slow neutrons from the first frame are counted as fast neutrons in the subsequent frame. Hence, the duration of one frame  $t_f$  needs to be increased. If the neutron arrives at the end of the frame (i.e. 2 ms after the start of the pulse) the velocity is 930 m/s and the wavelength is 4.254 Å.

For the next measurement the voltage was increased to  $V_{p-p} = 1$  V, therefore increasing the amplitude of the magnetic field  $B_1$ . The duration of one frame was increased to 3.03 ms (330 Hz). This allows for neutron velocities down to 614 m/s and wavelength up to 6.445 Å. All other parameters remained unchanged. The TOF spectrum is plotted

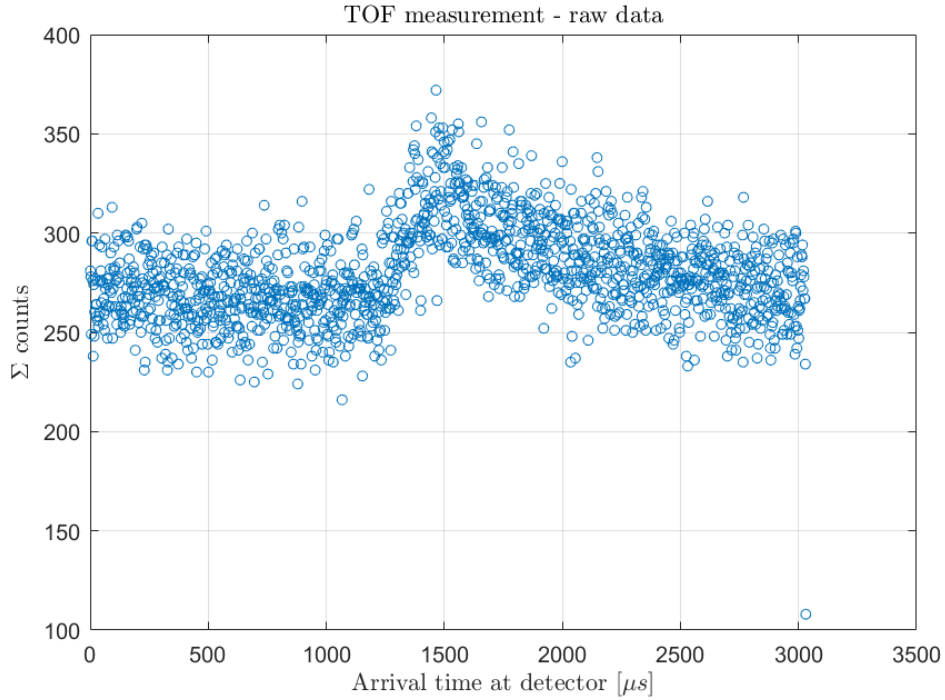


Figure 4.9: Measured Time-of-flight spectrum with  $f = 3.910933$  MHz,  $t_p = 30$  cycles,  $V_{p-p} = 1$  V,  $t_f = 3.03$  ms, total measurement time of 1 h and 200 kW reactor power. Within the first  $1200 \mu\text{s}$  no strong variation in intensity was found (no frame overlap) and they were taken as background level.

in figure (4.9).

One can see that frame overlap has been avoided. Nevertheless, the SNR value remains very low. The processed TOF data can be seen in figure (4.10). Neutron counts of the spectrum were first averaged over  $20 \mu\text{s}$ . Next, counts of the first  $1200 \mu\text{s}$  were assigned as background noise. This is justified by the assumption that no neutrons are faster than  $\frac{1.89 \text{ m}}{1200 \mu\text{s}} = 1550 \text{ m/s}$ , which corresponds to a wavelength of  $\lambda = 2.552 \text{ \AA}$ . This background value was then subtracted from the spectrum. The SNR is consequently the neutron counts divided by the background and has a maximum value of  $1.21 \pm 0.07$  at  $3.13 \text{ \AA}$ . The measurement error was calculated by taking the square root of the intensities after averaging over  $20 \mu\text{s}$ .

To increase the SNR to reasonable value a measurement series with different  $B_1$  amplitudes was conducted. The amplitude was varied by changing the peak-peak voltage  $V_{p-p}$ . The according pulse duration  $t_p$  needs to be found as well. The results are listed in table (4.2). One can see that no significant increase of the SNR was achieved.

A TOF measurement with  $I_{\text{FS}} = 0 \text{ A}$  (field stepper turned off) yielded a maximum SNR of  $1.05 \pm 0.06$  (i.e. noise only). This suggests that the strongest source of the high background and low SNR is the adiabatic field transition between the two supermirrors. In order to obtain a more non-adiabatic transition another field stepper was squeezed between the RF flipper and the first field stepper. This current sheet is an aluminium plate that can conduct currents up to 100 A. With switched off RF field and current

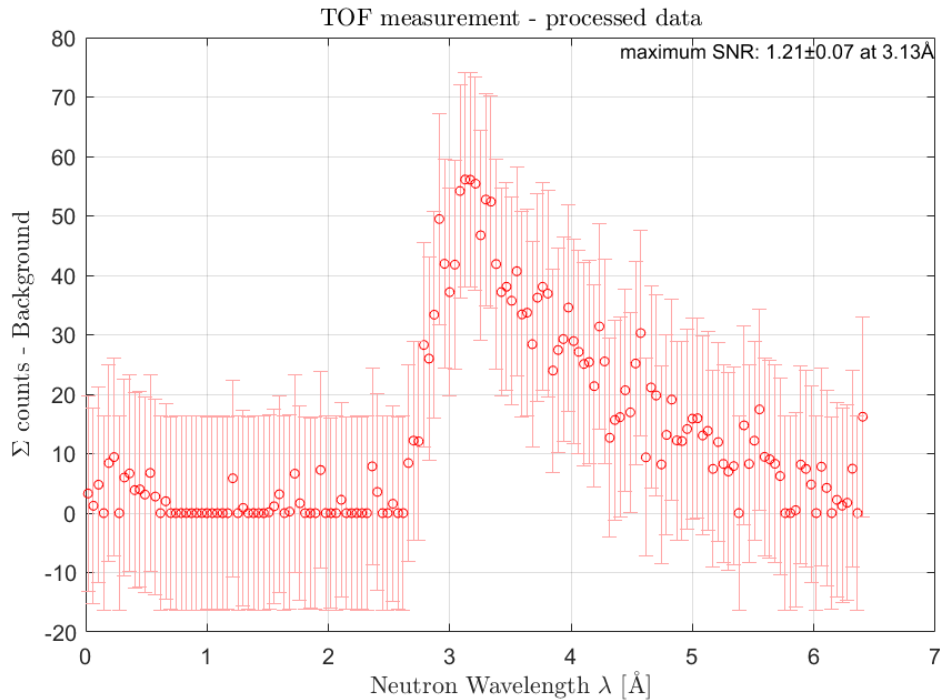


Figure 4.10: Processed data of the TOF measurement series of figure (4.9). The arrival time of the neutrons was converted to wavelength and the intensity was averaged over  $20 \mu\text{s}$ . A background noise was subtracted from the entire spectrum and the all measurement points below the background level were set to zero.

$V_{p-p}$	$t_p$ [cycles]	tot. measurement time	max. SNR	at wavelength [Å]
1	10	1 h	$1.19 \pm 0.18$	3.21
1	15	1 h	$1.34 \pm 0.18$	3.42
1	20	30 min	$1.41 \pm 0.25$	3.47
1.5	20	10 min	$1.64 \pm 0.49$	3.42
1.5	15	1 h	$1.41 \pm 0.18$	3.47
1.5	20	1 h	$1.52 \pm 0.19$	3.34
1.5	25	1 h	$1.66 \pm 0.19$	3.34
1.5	30	1 h	$1.7 \pm 0.2$	3.25

Table 4.2: Summary of TOF measurements with different parameters. The peak-peak voltage  $V_{p-p}$  is provided by the function generator for different pulse durations  $t_p$ . The signal-to-noise ratio (SNR) is increasing with stronger and longer oscillating magnetic fields. All other parameters were not varied between the measurements. Current through the field stepper was set to maximum value of  $I_{FS} = 6 \text{ A}$ . The frequency was  $f = 3.910933 \text{ MHz}$  and the frame time  $t_f = 303 \text{ ms}$ .



sheet but turned on field stepper ( $I_{FS} = 6 \text{ A}$ ), the neutron counts were  $1930 \pm 44$  in 2 min. When the current sheet was turn on as well ( $I_{CS} = 100 \text{ A}$ ), the measured intensity was  $1884 \pm 43$ . The background noise could not be reduced significantly utilising an additional field stepper.

As a last attempt the detector position was slightly changed and cadmium was used to absorb scattered neutrons, thus ensuring that all detected neutrons were going through the RF flipper. With this and the field stepper at  $I_{FS} = 6 \text{ A}$ , the measured intensity in 2 min was  $1415 \pm 38$ . With this slight improvement a TOF spectrum was recorded (figure 4.11).

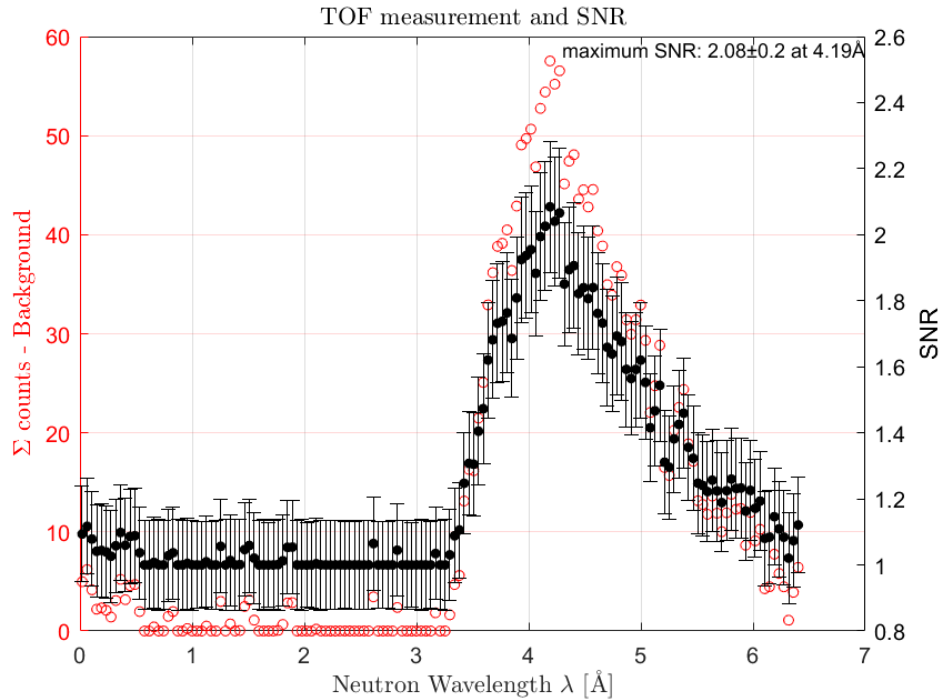


Figure 4.11: Processed Time-of-flight spectrum with  $f = 3.910933 \text{ MHz}$ ,  $t_p = 30$  cycles,  $V_{p-p} = 1.7 \text{ V}$ ,  $t_f = 3.03 \text{ ms}$ , total measurement time of 30 min and 250 kW reactor power. The maximum SNR value is  $2.08 \pm 0.2$  at  $4.19 \text{ \AA}$ . Some frame overlap is still visible, but since the peak signal is not affected it can be neglected.

The maximal signal-to-noise ratio improved to  $2.08 \pm 0.2$ . Its corresponding wavelength shifted to  $4.19 \text{ \AA}$ , most likely due to the new detector position. Due to divergence of the beam, the grazing angle between incident neutrons and the supermirror will be position dependent, leading to a position dependent wavelength spectrum.

### 4.3 Discussion

Already the high background counts were a first harbinger of low SNR. Measured intensity with and without a field stepper showed that adiabatic magnetic field transition between the two supermirrors were the major cause for low SNR values. Using one field stepper lowered background noise, whereas a second field stepper (current sheet) could

not improve the signal. This was also the case for different magnetic field strength. By varying the voltage and the pulse duration, the SNR value was only improving slightly. Furthermore, cadmium shielding did not achieve the desired effect and the maximum SNR remained low at  $2.08 \pm 0.2$ . Due to the small experimental site, the supermirrors can not be placed further apart, which would increase the influence of the field stepper as well as the SNR. With this low SNR value the measurement time would become unreasonable long.

In conclusion, the spin chopping system did not provide clean time-of-flight signals and spin flipping a white beam with time dependent RF amplitudes did not become possible. The next attempt was to implement adiabatic RF flipper.

## Chapter 5

# Development of an adiabatic RF spin flipper coil

For this spin flipping approach at the white neutron beam no time-of-flight is necessary. The flippers of the SESANS instrument will now consist of adiabatic RF spin flipper instead of RF flipper with a time dependent amplitude of the oscillating magnetic field. Zero field precession induced by adiabatic RF flippers at a white neutron beam has been shown in [Kra+01]. A first advantage of this setup is the additional space at the experimental site, since the spin chopping system is not needed anymore. Nevertheless, the arrangement of flipper and supermirror remained the same as in section (4) for all following measurements. Solely the RF coil was exchanged and a gradient coil was placed in the aluminium box. Instead of a short RF flipper, a longer RF coil is used. Furthermore, a static gradient field has to be designed and implemented.

### 5.1 Experimental Setup and Preparation

After the first spin flipping approach and before setting up the second, a laser pointer has been installed in order to align the neutron-optical devices more conveniently. The construction is shown in figure (5.1). The mounting of the laser allows for rotations and translations. The laser light is reflected off a polished silicon plate, which is mounted on a translation stage and on a rotation stage as well. In this case, the neutrons interaction with silicon can be neglected, thus the laser light and the neutron beam can be aligned parallel to each other. Once this is achieved the supermirror is placed in the laser beam and aligned properly. Since neutrons and light are reflected in the same way from the mirror, it is easy to find the optimal detector position.

To obtain high flip efficiencies, a high adiabaticity parameter  $k$  is necessary. Moreover,  $k$  is dependent on the velocity distribution of the beam. From the previous section the spectrum of the white beam is known. The TOF measurement corresponding to the last entry of table (4.2) is used and depicted in figure (5.2). With it, one can calculate

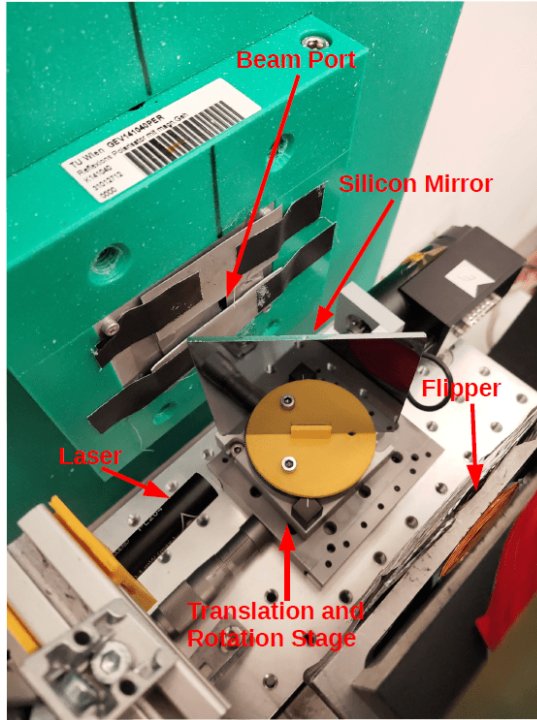


Figure 5.1: Setup of the alignment laser at the experimental site. The laser was placed between the beam port and the flipper. The silicon mirror mounted on a translation and a rotation stage enables one to align the laser parallel to the neutron beam. This way the position of supermirrors and detector can be find easily.

the average flip efficiency  $\epsilon$  for different adiabaticity parameters  $k$ , where  $k$  is referring to the adiabaticity parameter of the fastest neutrons. The result is plotted in figure (5.3). The aim was to reach  $k \approx 10$ , where the flip efficiency is  $\epsilon > 0.996$ .

In case of an adiabatic RF flipper, the adiabaticity parameter is given by the ratio of Larmor frequency induced by the RF field  $\omega_{L,rf}$  and the geometric rotation frequency  $\omega_g$  due to the gradient, hence  $k = \frac{\omega_L}{\omega_g} = \frac{\gamma B_1/2}{\pi v/L}$  (see section 2.3.3). For a given amplitude of the oscillating field  $B_1$ , the adiabaticity parameter  $k$  is smallest for the fastest neutrons in the spectrum. Hence, all other neutrons of the spectrum will have a higher  $k$ -value and consequently a higher flip efficiency, making it reasonable to use the maximum velocity (i.e. smallest  $k$ ) as a reference point. For a given velocity  $v$  and length of the magnetic field  $L$  the adiabaticity parameter can only be increased by increasing  $B_1$ . The amplitude resonance condition of a resonant RF flipper with respect to the fastest neutrons ( $B_{1,rf-res} = \frac{2\pi v_{max}}{\gamma L}$ ) yields  $k = 1$  at an adiabatic RF flipper. Furthermore, one can write  $k = B_1/B_{1,rf-res}$ , which states that the amplitude at the adiabatic RF flipper needs to be 10 times higher than in the resonant RF case in order to achieve  $k = 10$ . Regarding the electrical engineering side, from the last experiments it became apparent that the losses of the additional cables need to be considered. We assume a 1 m coax cable from the amplifier to the capacitor box, 1 m of cables inside the box and another meter of coax cable from the box to the coil. These distances are passed through twice,

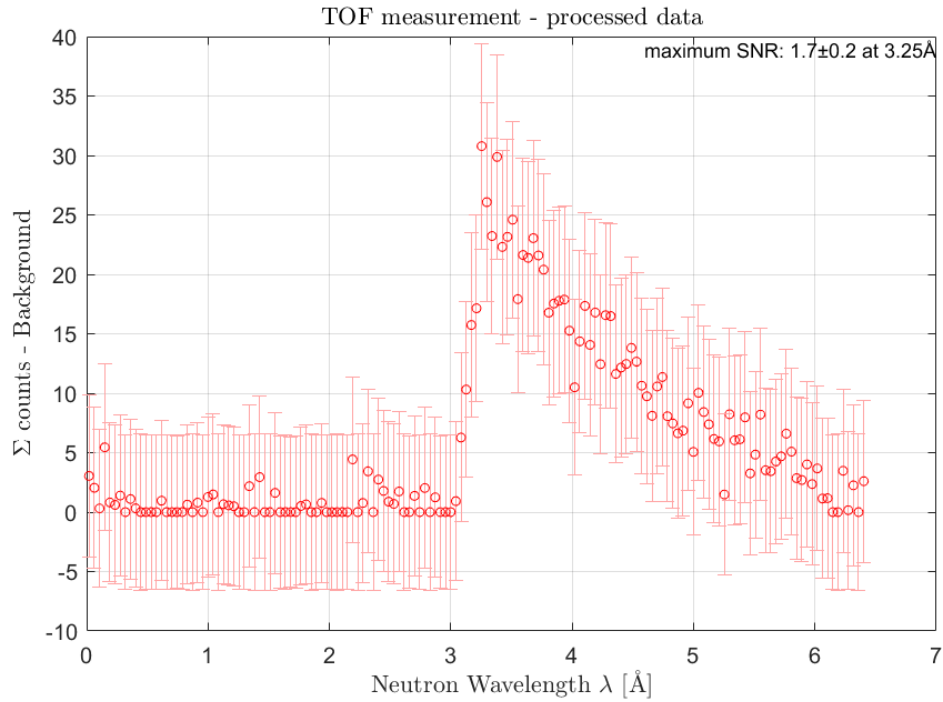


Figure 5.2: Processed Time-of-flight spectrum with  $f = 3.910933$  MHz,  $t_p = 30$  cycles,  $V_{p-p} = 1.5$  V,  $t_f = 3.03$  ms, total measurement time of 1 h and 250 kW reactor power. The fastest neutrons were considered to be at the maximum intensity i.e. at  $\lambda = 3.25$  Å. For this spectrum of the white beam the flip efficiency has been calculated (see figure 5.3).

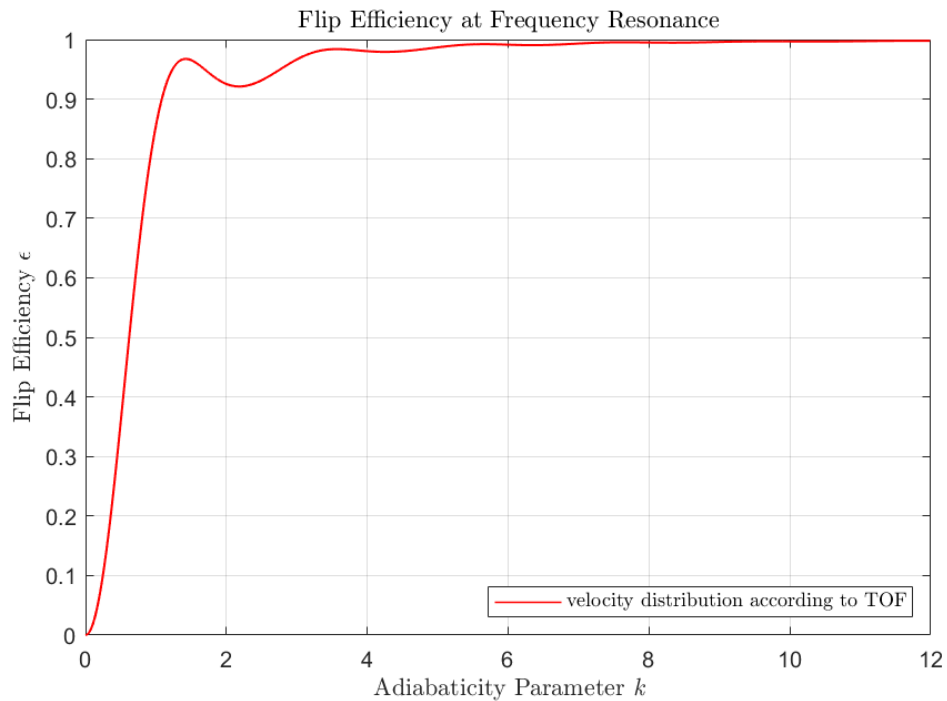


Figure 5.3: Flip efficiency  $\epsilon$  over adiabaticity parameter  $k$  of the fastest neutrons in the spectrum ( $v = 1217 \frac{\text{m}}{\text{s}}$ ). The spectrum was obtained during a TOF measurement, which is given in figure (5.2). A high  $k$ -value is reached by increasing the RF amplitude  $B_1$ , which ensures a high flip efficiency.

since the current runs back and forth. In total 6 m of additional cables are considered, which increase the overall resistance of the circuit drastically. This also raises the power demand at the load. Additional losses will arise in the static capacitors from rapidly reversing the polarity of the dielectric. No such losses will occur at the vacuum capacitors. However, this dissipation is complicated to quantify and will be watched out for during further preparation. Furthermore, the length of the region where the RF field is present is not equal to the length of the RF coil. The amplitude of the oscillating field is reduced at the ends of the RF coil. This is also indicated in figure (2.5). A measurement with a magnetometer at DC current showed, that the region inside the coil where the magnetic field is significantly strong is about 60 mm long. This influences the transit time  $t_t$  of the neutrons and consequently the amplitude  $B_{1,rf-res}$ . With this assumption the other relevant parameter can be calculated. In table (5.1) the results are summarized.

characteristic impedance	$Z_0$		50 $\Omega$
frequency	$f$		4 MHz
smallest wavelength of beam spectrum	$\lambda$	TOF measurement	3.25 $\text{\AA}$
fastest neutrons of beam spectrum	$v$	$v = \frac{h}{\lambda m}$	1217 $\frac{\text{m}}{\text{s}}$
length of RF coil	$L$		89 mm
effective length of RF coil	$L_{eff}$	measurement with DC current	60 mm
diameter of RF coil	$d$		26 mm
transit time for fastest neutrons	$t_t$	$t_t = \frac{v}{L_{eff}}$	49.29 $\mu\text{s}$
number of windings	$N$		32
diameter of wire	$d_w$		1.3 mm
length of wire	$l_w$	$l_w = \pi d N$	2.61 m
skin depth	$\delta$	$\delta = \sqrt{\frac{2}{\mu_0(\chi+1)\sigma 2\pi f}}$	0.033 mm
effective cross section of wire	$A_w$	$A_w = (\frac{d_w}{2})^2 \pi - (\frac{d_w}{2} - \delta)^2 \pi$	0.1314 mm <sup>2</sup>
resistance of load	$R_l$	$R_l = \frac{\rho l_w}{A_w}$	0.3422 $\Omega$
length of additional wires	$l_{add}$		6 m
diameter of additional wire	$d_{add}$		1 mm
effective cross section of add. wires	$A_{add}$	$A_{add} = (\frac{d_{add}}{2})^2 \pi - (\frac{d_{add}}{2} - \delta)^2 \pi$	0.1003 mm <sup>2</sup>
resistance of add. wires	$R_{add}$	$R_{add} = \frac{\rho l_{add}}{A_{add}}$	1.0293 $\Omega$
total resistance	$R$	$R = R_l + R_{add}$	1.3716 $\Omega$
inductance of load	$L_l$	$L_l = \frac{\mu_0 N^2}{l} (\frac{d}{2})^2$	7.6725 $\mu\text{H}$
capacitance at impedance matching	$C_1$	$C_1 = \frac{1}{\omega(\omega L_l - \sqrt{R(Z_0 - R)})}$	0.21547 nF
capacitance at impedance matching	$C_2$	$C_2 = \frac{1}{\omega Z_0} \sqrt{\frac{Z_0 - R}{R}}$	4.7384 nF
amplitude resonance of fastest neutrons	$B_{1,rf-res}$	$B_{1,rf-res} = \frac{2\pi v_{max}}{\gamma L_{eff}}$	0.696 mT
wanted adia. parameter of fastest neutrons	$k$		$k \approx 10$
amplitude of osc. magnetic field for $k = 10$	$B_1$	$B_1 = k \cdot B_{1,rf-res}$	6.96 mT
amplitude of magnetic gradient field	$B_{GR}$	$B_{GR} = B_1 / 2$	3.478 mT
amplitude of AC current at load	$I$	$I = \frac{B_1 L}{\mu_0 N}$	15.40 A
amplitude of voltage at $L_l$	$V_L$	$V_L = \omega L_l \cdot I$	2.97 kV
amplitude of voltage at $C_1$	$V_1$	$V_1 = \frac{1}{2\pi f C_1} \cdot I$	2.84 kV
magnitude of impedance of $C_1$ and $L_l$ and $R$	$Z_{tot}$	$Z_{tot} = \sqrt{(2\pi f L_l - \frac{1}{2\pi f C_1})^2 + R^2}$	8.28 $\Omega$
amplitude of voltage at $C_2$	$V_2$	$V_2 = Z_{tot} \cdot I$	127.56 V
amplitude of power at load	$P$	$P = I^2 \cdot R \propto k^2$	325.42 W

Table 5.1: Theoretical calculation of parameters for an adiabatic RF spin flipper. Here  $h$  is the planck constant,  $m$  the mass of the neutron,  $\mu_0$  is the permeability of vacuum,  $\chi$  the magnetic susceptibility of copper,  $\sigma$  the conductivity of copper,  $\rho$  the resistivity of copper and  $\gamma$  the gyromagnetic ratio.

In comparison to the RF coil used at the spin chopping system, the coil at the adiabatic RF flipper is longer in order to increase the length of the relevant magnetic field region and therefore the adiabaticity parameter. It has a length of 89 mm (see figure 5.4).

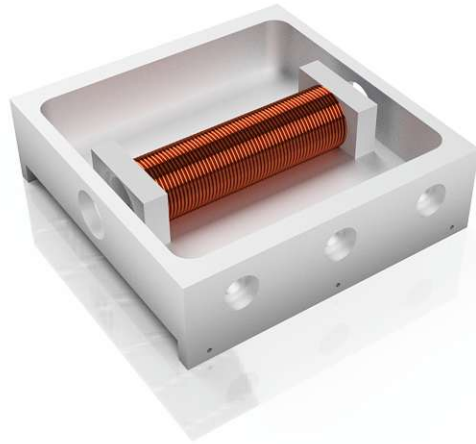


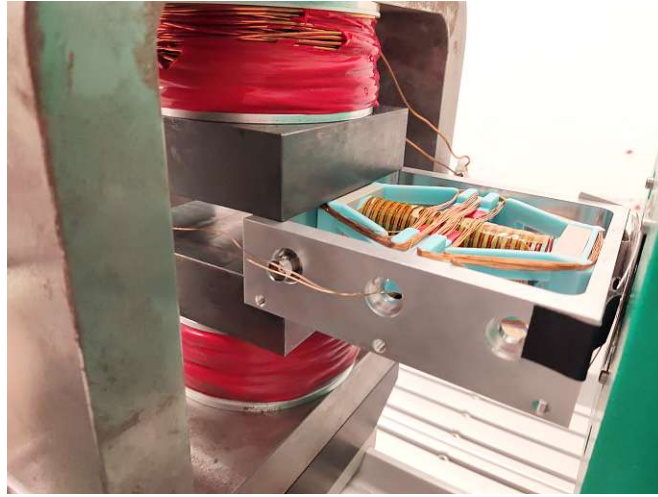
Figure 5.4: Render image of the RF coil used at the adiabatic spin flippers. The coils length is 89 mm. The aluminium box is the same as for the spin chopping system (figure 4.3b). The inside length in flight direction is 121.5 mm, the height is 25 mm. The end plates of the bobbin are made out of aluminium. Beneath the RF coil a notch in the box allows for larger coil diameters than 25 mm.

This influences the amplitudes  $B_{1,rf-res}$  and  $B_1$ . The gradient field amplitude  $B_{GR}$  is given by the value of the amplitude of one rotating field component, i.e.  $B_1/2 = B_{GR} = 3.478$  mT. As a first task a suitable design of a gradient coil needs to be found. It must be capable of inducing a magnetic field strong enough to reach  $k \approx 10$  and the coil has to fit inside the aluminium box, which was especially challenging since the original design did not consider adding a gradient and thus the space between the RF coil and the pole shoe as well as between the RF coil and the box is very limited. Moreover, the field should be constant in the directions perpendicular to the propagation direction and only exhibit a gradient in flight direction. In order to achieve this one makes use of the fact that the magnetic field decreases with distance to the wire.

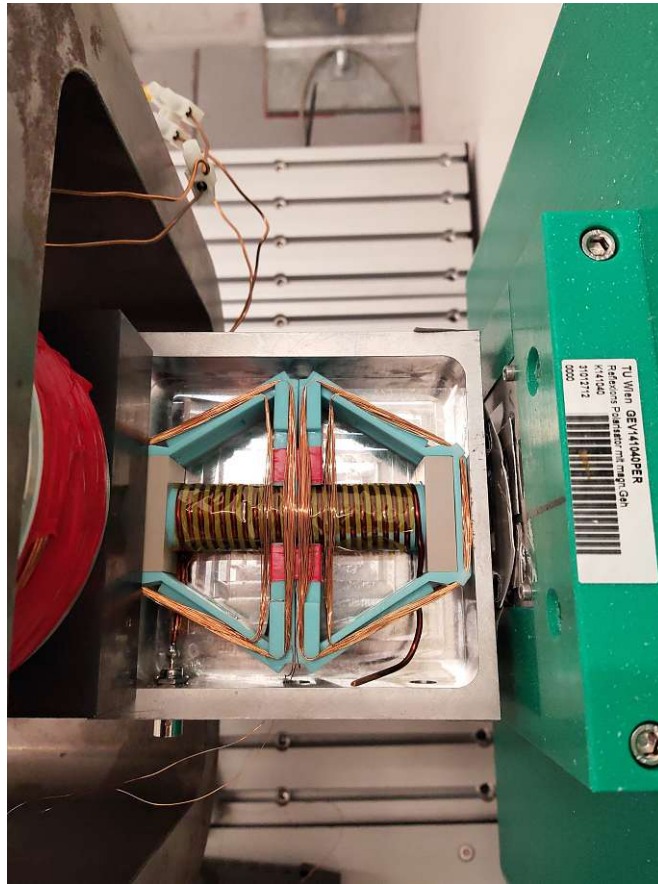
The design best suited turned out to be a double trapezoidal coil in Helmholtz-like configuration. The setup with gradient coil and RF coil is depicted in figure (5.5).

The current through the two loops of the trapezium has different direction of rotation, hence inducing a magnetic field in opposite direction at the two ends of the RF coil. Furthermore, the distance between the gradient and the RF coil is increasing, until halfway the orientation of the field changes and the distance is decreasing again. An identical coil has been wound at the very bottom of the aluminium box to create a more





(a)



(b)

Figure 5.5: Photo of the adiabatic RF flipper outside the pole shoes ( $B_0$  field). This design was used for the experiments to determine the flip efficiency. The double trapezoidal coil is inducing the gradient field. The RF coil is covered in Kapton tape to prevent shorts between the electrical ground (aluminium box) and the RF coil. The counterpart of the upper trapezoidal gradient coil runs along the bottom of the box and is not visible in these photos.

homogeneous magnetic field in directions perpendicular to the beam direction due to

this Helmholtz-like configuration. The design of the bobbin of the gradient is depicted in figure (5.6) and is printed at an in-house resin 3D printer.

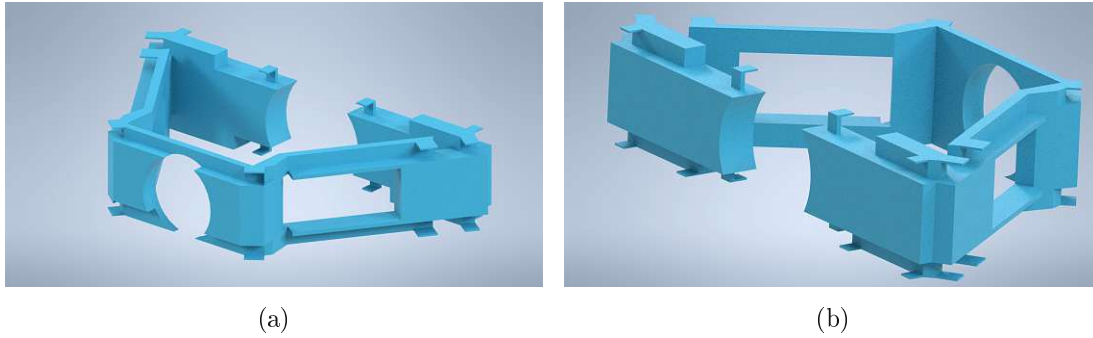


Figure 5.6: (a) Front and (b) rear view of the designed coil holder for the gradient coil, created with  $\text{\textcircled{R}}$ Autodesk Inventor. Two identical pieces were used for one gradient coil. The circular window is a passage for the neutron beam, whereas the rectangular windows on the side make a connection of the RF coil and the BNC connector at the aluminium box possible. The small hooks at the top and bottom make up the upper and the lower cable channel, which are vertically as far apart as possible.

With a total of 35 windings per loop and wire with 0.28 mm in diameter the coil can reach a gradient of  $B_{GR} = 3.478 \text{ mA}$  at a DC current of about 2.48 A. At this current the wire is heating up rapidly, which may lead to problems during long-term operations.

The next preparation step is to match the impedance of the source and cable to the RF coil at about  $f = 4 \text{ MHz}$ . Due to the different RF coil (different number of windings, length and wire) the inductance changed compared to the spin chopping system and one needs to adapt the capacitance in order to match the circuit. Fortunately, the new values for the capacitance were in the reach of the previous capacitor arrangement and no new capacitors had to be added. The vector network analyser  $\text{\textcircled{R}}$ PicoVNA 100 Series with a frequency range from 300 kHz to 6 GHz was used to investigate the circuit. The variable capacitors could be tuned to obtain impedance matching at  $f = 3.781 \text{ MHz}$  (see figure 5.7).

After the impedance was matched, a forward power of 39 W at an reflected value of 1 W was obtained. Due to the high current necessary and the high impedance (resulting from the high frequency), the amplitude of the voltage at the coil is extremely high and became a severe problem. Successively, different issues concerning the RF coil arose. Between the windings of the coil electrical shorts occurred, especially between the first windings. The voltage between the beginning and end of the coil is  $V_L = \omega L_l \cdot I = 2.97 \text{ kV}$ . Between the windings the voltage drops roughly by  $2.97 \text{ kV} / 32 = 92.81 \text{ V}$ , which is causing electric arcs between the windings. These shorts destroy the electrical circuit as well as affect the magnetic field in the RF coil and need to be avoided. Another issue are shorts between the RF coil and the bottom of the aluminium box, i.e. electrical ground. The distance between the wire of the RF coil and the box is less than 1 mm and the breakdown voltage of air becomes insufficient. The sparks are burning the wire

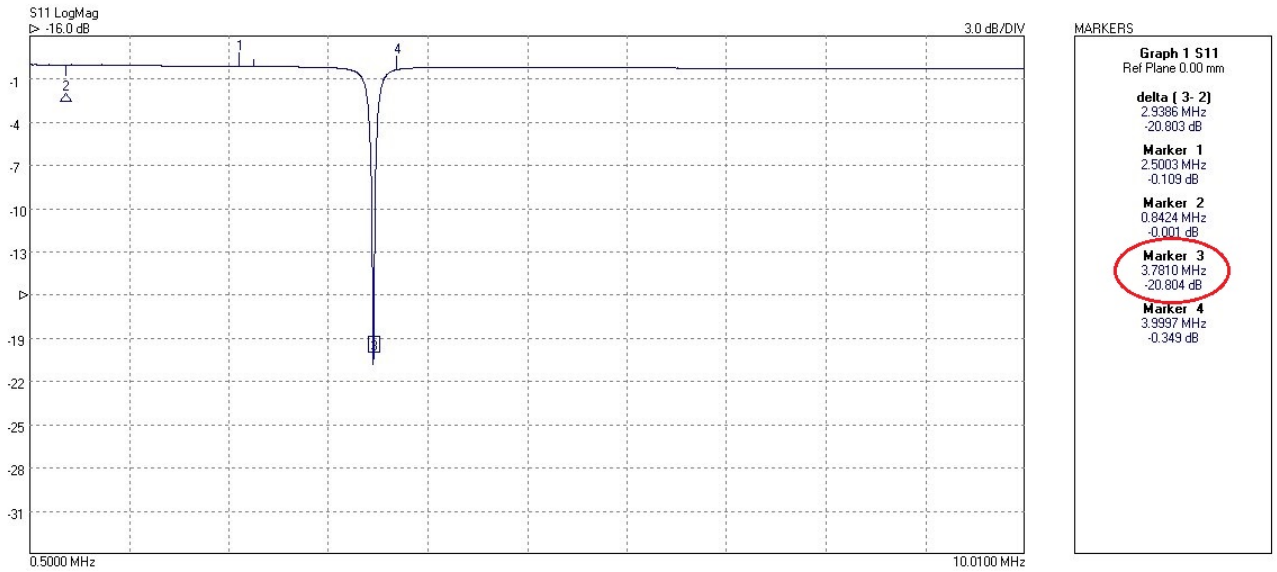


Figure 5.7: Electrical response of the circuit measured with the  $\text{\textcircled{R}}$ PicoVNA for different frequencies. The ordinate shows the S-parameter  $S_{11}$  in dB, which is the input port voltage reflection coefficient.  $S_{11}$  is the ratio of the reflected and incident signal. A low ratio (i.e. low reflections) of  $S_{11} = -20.8$  dB was found at  $f = 3.781$  MHz. For these measurements, the VNA is replacing the amplifier and the function generator in the circuit diagram, figure (4.4).

and also affect the circuit and the magnetic field. Finally, shorts appeared between the coil and the aluminium end plates, which are also grounded.

To avoid these electrical shorts different actions were taken to improve the isolation of the RF coil and lower the power demand.

- The material of the end plates was changed to PEEK, the same material the bobbin of the RF coil is made of
- The diameter of RF coil was decreased to 24 mm (formerly 26 mm) to increase the space between RF coil and box
- A thicker wire was used, with a diameter of 2 mm (formerly 1.3 mm) to decrease to resistance of the load
- The last to points make a change in the number of windings necessary, from 32 to 23
- The RF coil was isolated additionally with  $\text{\textcircled{R}}$ Kapton tape (see figure 5.5)
- The frequency was decreased to 1 MHz

The lower frequency affects the skin depth and the diminishes the resistance. Additionally, the impedance of the RF coil is decreased ( $|Z_l| = \omega L_l$ ), which results in a

frequency	$f$		1 MHz
diameter of RF coil	$d$		24 mm
number of windings	$N$		23
diameter of wire	$d_w$		2 mm
length of wire	$l_w$	$l_w = \pi d N$	1.73 m
skin depth	$\delta$	$\delta = \sqrt{\frac{2}{\mu_0(\chi+1)\sigma 2\pi f}}$	0.066 mm
effective cross section of wire	$A_w$	$A_w = (\frac{d_w}{2})^2 \pi - (\frac{d_w}{2} - \delta)^2 \pi$	0.4013 mm <sup>2</sup>
resistance of load	$R_l$	$R_l = \frac{\rho l_w}{A_w}$	0.0744 $\Omega$
effective cross section of add. wires	$A_{add}$	$A_{add} = (\frac{d_{add}}{2})^2 \pi - (\frac{d_{add}}{2} - \delta)^2 \pi$	0.1938 mm <sup>2</sup>
resistance of add. wires	$R_{add}$	$R_{add} = \frac{\rho l_{add}}{A_{add}}$	0.5329 $\Omega$
total resistance	$R$	$R = R_l + R_{add}$	0.6072 $\Omega$
inductance of load	$L_l$	$L_l = \frac{\mu_0 N^2}{l} (\frac{d}{2})^2$	3.377 $\mu\text{H}$
capacitance at impedance matching	$C_1$	$C_1 = \frac{1}{\omega(\omega L_l - \sqrt{R(Z_0 - R)})}$	10.11 nF
capacitance at impedance matching	$C_2$	$C_2 = \frac{1}{\omega Z_0} \sqrt{\frac{Z_0 - R}{R}}$	28.71 nF
amplitude of AC current at load	$I$	$I = \frac{B_1 L}{\mu_0 N}$	21.43 A
amplitude of voltage at $L_l$	$V_L$	$V_L = \omega L_l \cdot I$	454.77 V
amplitude of voltage at $C_1$	$V_1$	$V_1 = \frac{1}{2\pi f C_1} \cdot I$	337.4 V
magnitude of impedance of $C_1$ and $L_l$ and $R$	$Z_{tot}$	$Z_{tot} = \sqrt{(2\pi f L_l - \frac{1}{2\pi f C_1})^2 + R^2}$	5.51 $\Omega$
amplitude of voltage at $C_2$	$V_2$	$V_2 = Z_{tot} \cdot I$	118.1 V
amplitude of power at load	$P$	$P = I^2 \cdot R \propto k^2$	278.89 W

Table 5.2: New theoretical calculation of parameters for an adiabatic RF spin flipper. Here  $\mu_0$  is the permeability of vacuum,  $\chi$  the magnetic susceptibility of copper,  $\sigma$  the conductivity of copper and  $\rho$  the resistivity of copper. All quantities not mentioned here remained unchanged and are given in table (5.1).

smaller voltage at the load. This new starting point influences most other parameters. The altered quantities are summarized in table (5.2).

The total resistance decreased, whereas the required current increased due to the fewer windings of the RF coil. Nevertheless, the power demand could be diminished and is now 278.89 W instead of 325.42 W. Furthermore,  $C_1$  and  $C_2$  shifted significantly, thus more capacitors have to be added. Moreover,  $V_1 < 1$  kV and  $V_2 < 1$  kV allowing to use single additional static capacitors with a breakdown voltage of 1 kV. The two extra capacitances  $C_{24}$  and  $C_{12}$  are insert to the circuit of shown in figure (5.8). They consist of 13 and 9 identical capacitors respectively and are connected in parallel. The individual capacitors are the same as used for  $C_{21}$  therefore having a capacitance of 1 nF and a breakdown voltage of 1 kV, hence  $C_{24} = 13$  nF and  $C_{12} = 9$  nF. A photo of the inside of the newly connected capacitor box is shown in figure (5.9).

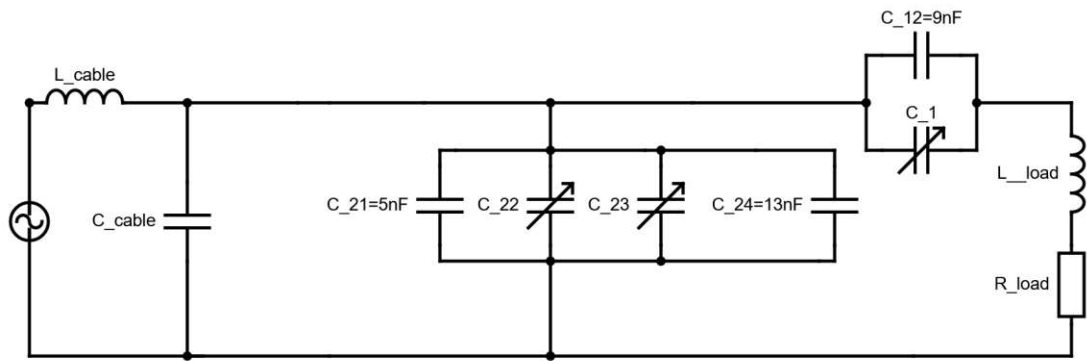


Figure 5.8: Circuit diagram of the adiabatic RF spin flipper. The RF coil has an inductance  $L_{load}$ . All resistances of additional cables are added to the resistance  $R_{load}$ . The source consists of the function generator and the power amplifier. The capacitors  $C_{12}$  and  $C_{24}$  have been added to the circuit to match the impedance.

With these new capacitors the resonance frequency was found at  $f = 1.0012$  MHz. The corresponding VNA measurement is given in figure (5.10).

Finally, with all these measures it was possible to obtain a forward power of 309 W with a reflected power of 11 W at  $V_{p-p} = 640$  mV from the function generator. More importantly, no shorts occurred between the windings or between the RF coil and the ground. It was even possible to go up 386 W forward power with 15 W reflected power without shorts for a very brief moment ( $\sim 1$  s). However, the wire of the coil gets very hot and such high powers are not suitable long-term operations.



Figure 5.9: Photo of the capacitors inside the aluminium box, which prevents the RF radiation to disturb the detector's amplifier electronics.

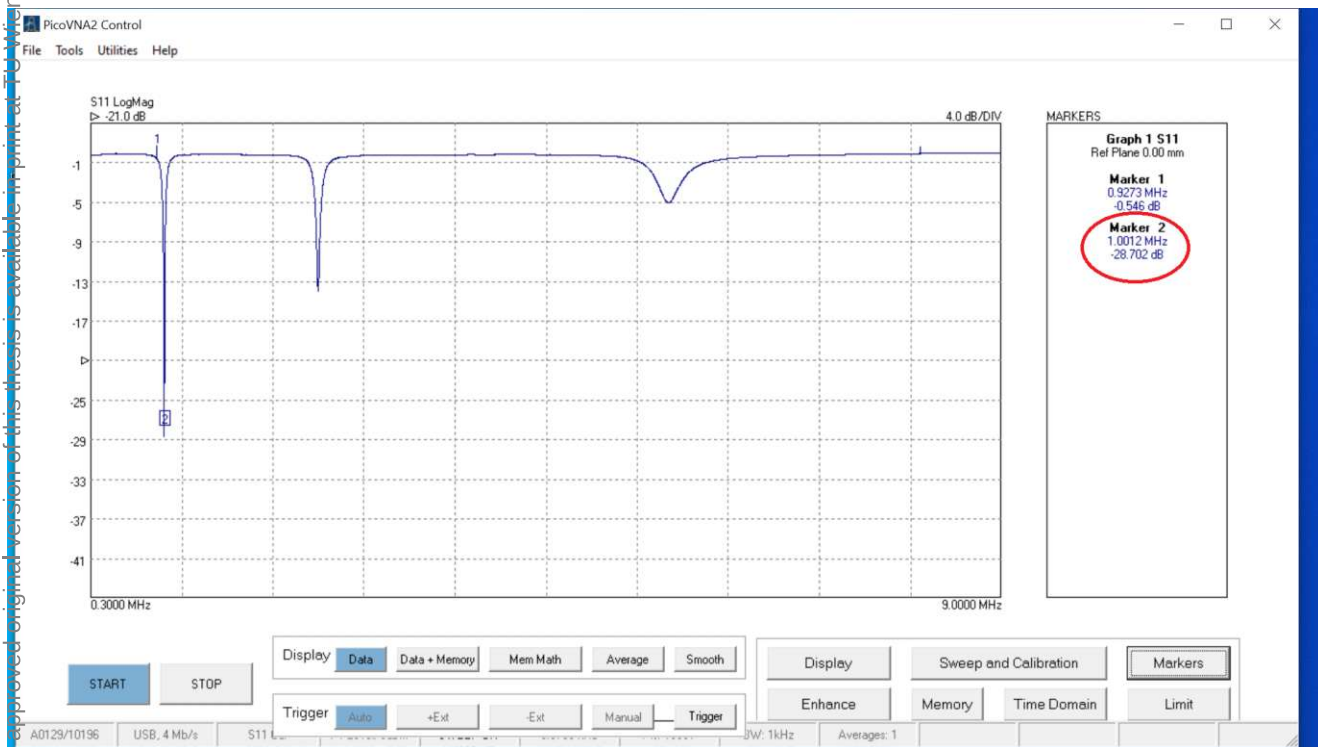


Figure 5.10: Electrical response of the circuit measured with the PicoVNA for different frequencies. The ordinate shows the S-parameter  $S_{11}$  in dB. A low ratio (i.e. low reflections) of  $S_{11} = -28.702$  dB was found at  $f = 1.0012$  MHz. For these measurements, the VNA is replacing the amplifier and the function generator in the circuit diagram, figure (5.8).

## 5.2 Results

For the measurements with the adiabatic RF flipper at the white beam line, the setup was similar to the one of the spin chopping system. The position of the detector and the supermirror was the same, but latter was flipped, such that the two supermirrors exhibit parallel magnetic fields. Furthermore, the field stepper was removed and instead of the short RF coil, the longer coil and the gradient coil were used (figure 5.5). The pole shoes of the  $B_0$  field remained unchanged, meaning square pole shoes, even though the final SESANS setup requires parallelogram-shaped pole shoes.

Since the adiabatic RF flipper has to be operated in frequency resonance ( $\omega = \gamma B_0$ ) the compatible  $B_0$  field needs to be found before each measurement. An exemplary measurement is given in figure (5.11). At a given frequency, the closer the magnetic field gets to  $B_0 = 2\pi f/\gamma$ , the more likely it becomes to rotate the spin of the neutrons. At the minimum intensity most of the spins are rotated and absorbed by the subsequent supermirror. Hence for this setup the goal is to obtain count rates as low as possible.

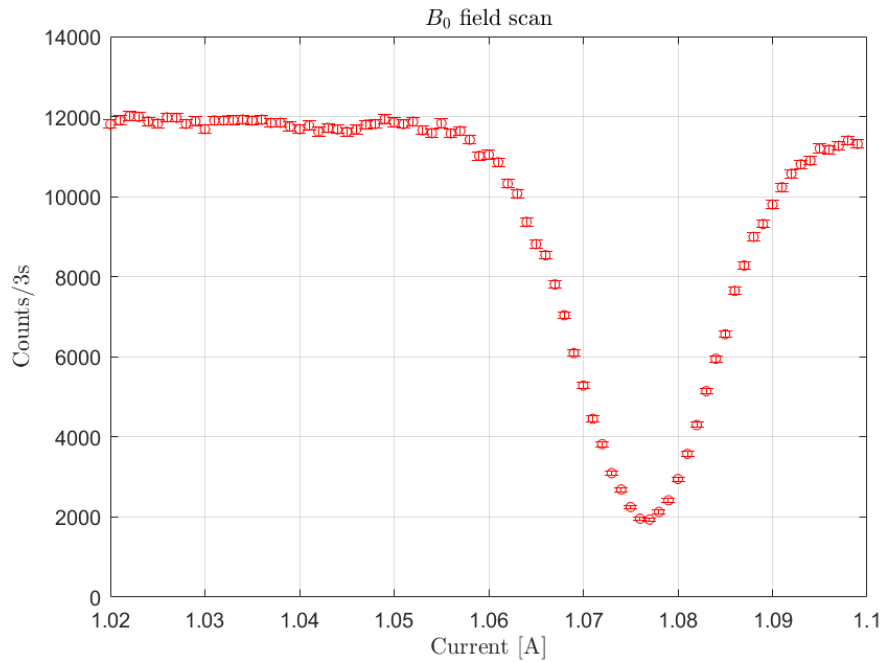


Figure 5.11: Intensity over current through the  $B_0$ -coil. The RF field was set to  $f = 1.0012$  MHz and  $V_{p-p} = 58$  mV, which is about 1 W power from the amplifier. The gradient coil was turned off. Frequency resonance condition in the resonant RF case was met at  $I = 1.077$  A. Due to the hysteresis of the iron core, the current was ultimately set to 1.07 A. Since the neutron beam is polychromatic, the flip efficiency under this conditions remains rather low at  $\epsilon = 0.7220$ .

Once the resonance is found, the gradient field is added to  $B_0$  and the corresponding RF amplitude  $B_1$  must be determined ( $B_{GR} = B_1/2$ ). This was done by scanning the current in the gradient coil for fixed oscillating field amplitudes and measuring the intensity (figure 5.12). At the minimum of each gradient field scan the condition  $B_1/2 =$

$B_{GR}$  is fulfilled. Furthermore, the higher  $B_1$  the higher the adiabaticity parameter  $k$ , which leads to lower count rates, i.e. higher flip efficiencies.

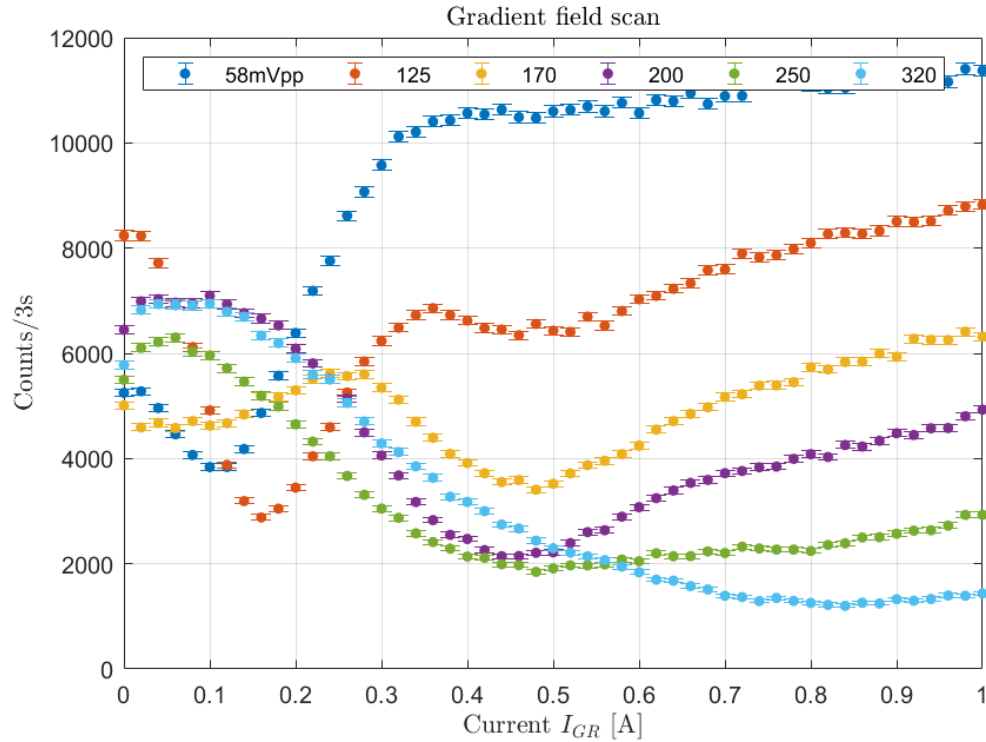


Figure 5.12: Selected results of a measurement series. Intensity versus current in the gradient coil  $I_{GR}$  for different strengths of the oscillating field. The higher the field of the RF coil, the higher  $I_{GR}$  has to be in order to find an intensity minimum, at which  $B_1/2 = B_{GR}$ . The voltage values provided by the function generator correspond to the following forward  $P_f$  and reflected power  $P_r$ :  $P_f/P_r = 1/0 \mid 7/0 \mid 15/0 \mid 22/0 \mid 37/0 \mid 66/1$ .

In figure (5.13) all intensities at the minimum and the according current in the gradient coil  $I_{GR}$  are plotted for the entire measurement series. As mentioned above, higher RF amplitudes demand stronger current  $I_{GR}$  in order to reach a minimum.

From these intensities at the minimum the flip efficiency  $\epsilon$  was calculated with

$$\epsilon = \frac{I_{max} - I_{min}}{I_{max} + I_{min}} \quad (5.1)$$

where  $I_{max}$  is the count rate without any magnetic fields or spin flipping and  $I_{min}$  is the minimum count rate obtained by switching on the adiabatic RF flipper. The calculated flip efficiency is plotted in figure (5.14). It increases with larger RF amplitudes, but remains rather low even at 320 mVpp. Hence higher  $k$  values have to be obtained.

Before raising the electrical power at the RF coil and the gradient coil, measurements with Cadmium were conducted. The goal was to ensure that all neutrons counted had previously passed through the flipper. The summary of these measurements is shown in table (5.3). Two different setups were tested: with cadmium at the flipper and with cadmium at the beamport. Latter is aiming to shape the beam dimension in such a way that it matches the cross-section of the flipper. Both setup were compared to the former



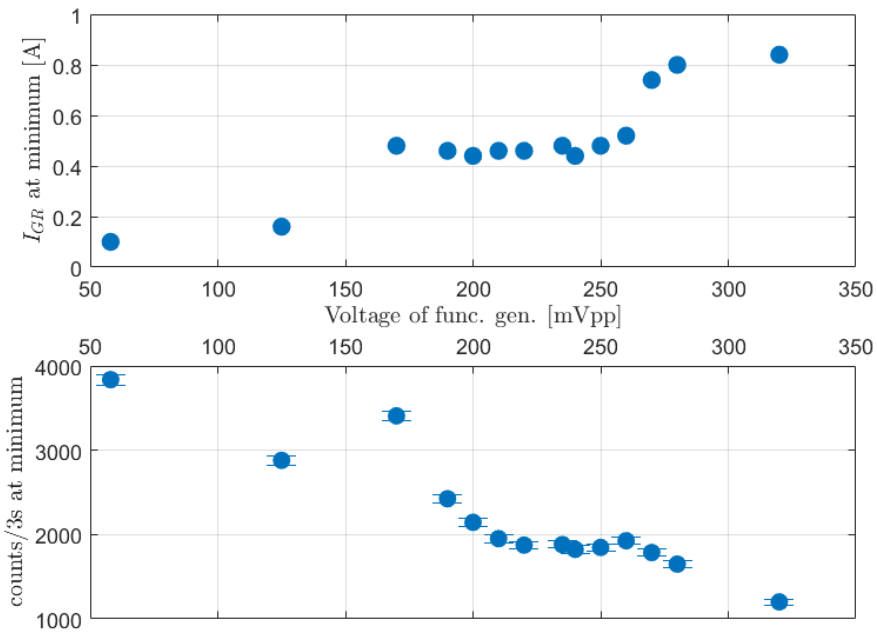


Figure 5.13: Position and value of the minimum intensity of the gradient field scans versus strength of the oscillating field. The required current  $I_{GR}$  increases with stronger RF fields, whereas the intensity decreases.

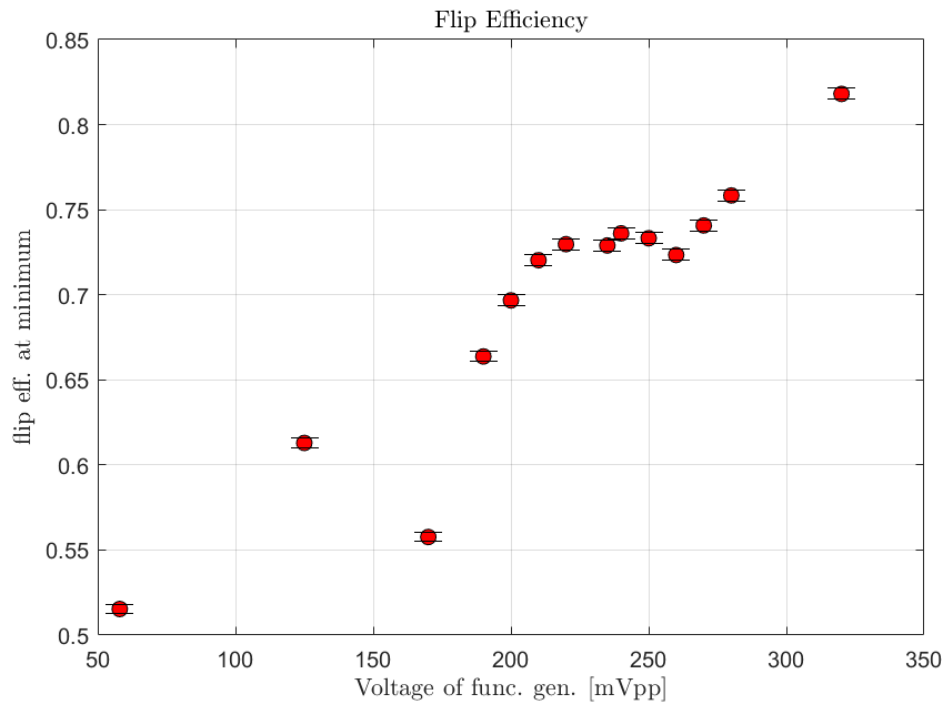


Figure 5.14: Calculated flip efficiency for different strengths of the oscillating field. The flip efficiency was calculated with equation (5.1), where the maximum intensity is  $I_{max} = 4000 \text{ s}^{-1}$  and the minimum intensity  $I_{min}$  given in figure (5.13). Overall, the efficiency increases with stronger oscillating fields.

	$I_{max}$ [s <sup>-1</sup> ]	$I_{min}$ [s <sup>-1</sup> ]	$I_{GR}$ [A]	flip efficiency
No Cadmium	5900	494	0.82	0.8454 (29)
Cadmium on flipper	3500	252	0.84	0.8658 (33)
Cadmium on beamport	3690	255	0.84	0.8706 (18)

Table 5.3: Three different tests with cadmium shielding at 350 mVpp, corresponds to  $P_f/P_r = 77/1$ . Highest efficiency was obtained with cadmium on the beamport, to match the beam dimension to the dimension of the adiabatic RF flipper.

setup without any cadmium shielding. All three gradient scans were done at 350 mVpp ( $P_f/P_r = 77/1$ ). The best flip efficiency was achieved with cadmium at the beamport where  $\epsilon = 0.8706$  (18). This enhanced the flip efficiency by  $0.8706$  (18)  $-$   $0.8454$  (29) =  $0.0252$  (34), compared to the previous setup. Therefore all subsequent measurements utilise this setup. The drawback of cadmium shielding is the reduced intensity, leading to longer measurement times to reach the same statistical precision.

The measurement series given in figure (5.15) investigates higher RF amplitudes. The necessary current in the gradient coil to reach the minimum and the corresponding intensity is depicted in figure (5.16). The calculated flip efficiency is given in figure (5.17). One can see that it was possible to increase the flip efficiency by increasing the power in the flipper. With 640 mVpp from the function generator a power of  $P_f/P_r = 309/11$  was obtained and the efficiency was  $\epsilon = 0.9231$  (15) at  $I_{GR} = 1.88$  A. A planned measurement at 660 mVpp ( $P_f/P_r = 335/12$ ) could not be concluded, because solder joints melted and the coax cable from the capacitor box to the RF coil broke.

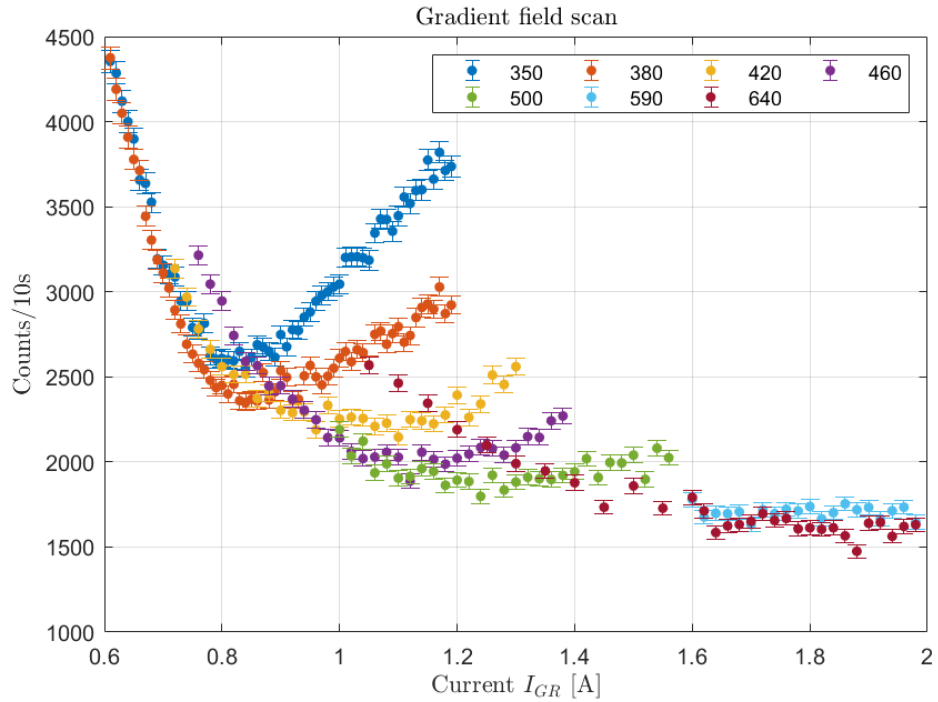


Figure 5.15: Select results of a measurement series. Intensity versus current in gradient coil  $I_{GR}$  for different strengths of the oscillating field. The higher the field of the RF coil, the higher  $I_{GR}$  has to be in order to find an intensity minimum, at which  $B_1/2 = B_{GR}$ . The voltage values provided by the function generator correspond to the following forward  $P_f$  and reflected power  $P_r$ :  $P_f/P_r = 77/1 \mid 94/2 \mid 119/3 \mid 147/4 \mid 179/5 \mid 262/8 \mid 309/11$ .

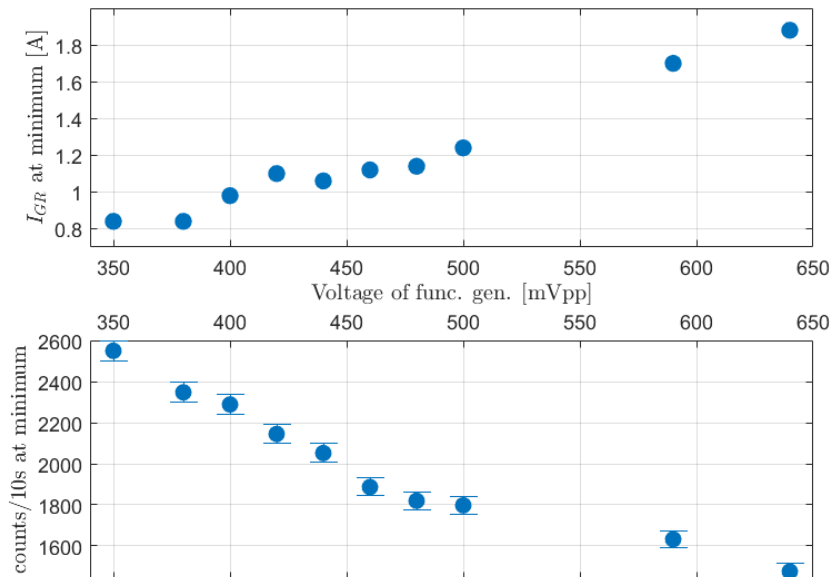


Figure 5.16: Position and value of the minimum intensity of the gradient field scans versus strength of the oscillating field. The required current  $I_{Gr}$  increases with stronger RF fields, whereas the intensity decreases.

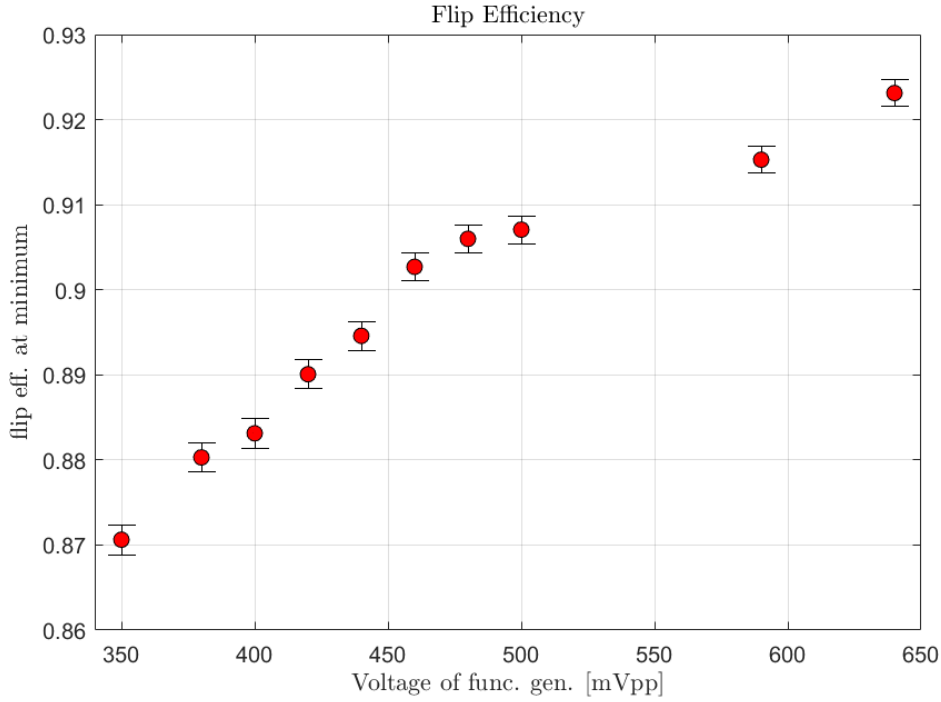


Figure 5.17: Calculated flip efficiency for different strength of the oscillating field. The flip efficiency was calculated with equation (5.1), where the maximum intensity is  $I_{max} = 3690 \text{ s}^{-1}$  and the minimum intensity  $I_{min}$  given in figure (5.16).

A scan of the  $B_1$  amplitude at  $I_{GR} = 1.8 \text{ A}$  is plotted in figure (5.18). This measurement is less precise than scans of the current in the gradient coil. A maximum flip efficiency of  $\epsilon = 0.9284$  (49) was obtained at 640 mVpp. This is a similar result as acquired with the aforementioned gradient scan given in figure (5.15), where the efficiency became  $\epsilon = 0.9231$  (15) at  $I_{GR} = 1.88 \text{ A}$  and 640 mVpp ( $P_f/P_r = 309/11$ ).

For another measurement the third magnetic field was scanned, namely  $B_0$ . In this measurement the detector and the supermirror had a different position than in the previous measurements but it remained the same for the following measurements given in table (5.4). Thus this results are not entirely comparable to the earlier ones. A first  $B_0$  scan at 57 mVpp to find the frequency resonance showed a minimum at  $I = 1.045 \text{ A}$  and a subsequent gradient field scan at 440 mVpp a minimum of  $I_{min} = 2351/10 \text{ s}$  at  $I_{GR} = 0.92 \text{ A}$ . Next another  $B_0$  scan was conducted with the previously determined values for the gradient field and RF field. The result is given in figure (5.19). One can see that the neutron count rate could not be reduced further by changing the  $B_0$  field.

The adiabaticity parameter is not constant throughout the flipper, but shows a space dependency due to the space dependency of the RF amplitude  $B_1$ . Outside the flipper box close to the entrance windows a weak RF field can arise. Therefore low  $k$ -values can occur at the beginning and end of the flipper, which lead to unwanted rotations of the polarization [Plo09]. To prevent this, aluminium foil was used to cover the windows of the aluminium box. The neutrons are now exposed to more material. Four different setups were compared at 440 mVpp ( $P_f/P_r = 133/3$ ). No aluminium foil (previous

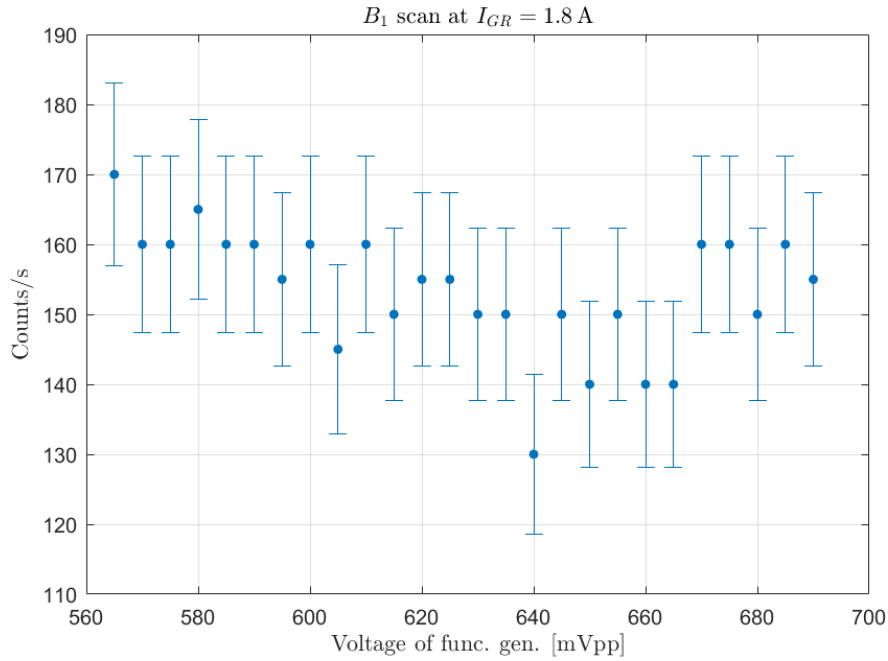


Figure 5.18: Scan of the RF amplitude at frequency resonance and  $I_{GR} = 1.8$  A. The highest flip efficiency was found at 640 mVpp and amounts to  $\epsilon = 0.9284$  (49). This is in agreement with the efficiency obtained by the gradient scan in figure (5.15).

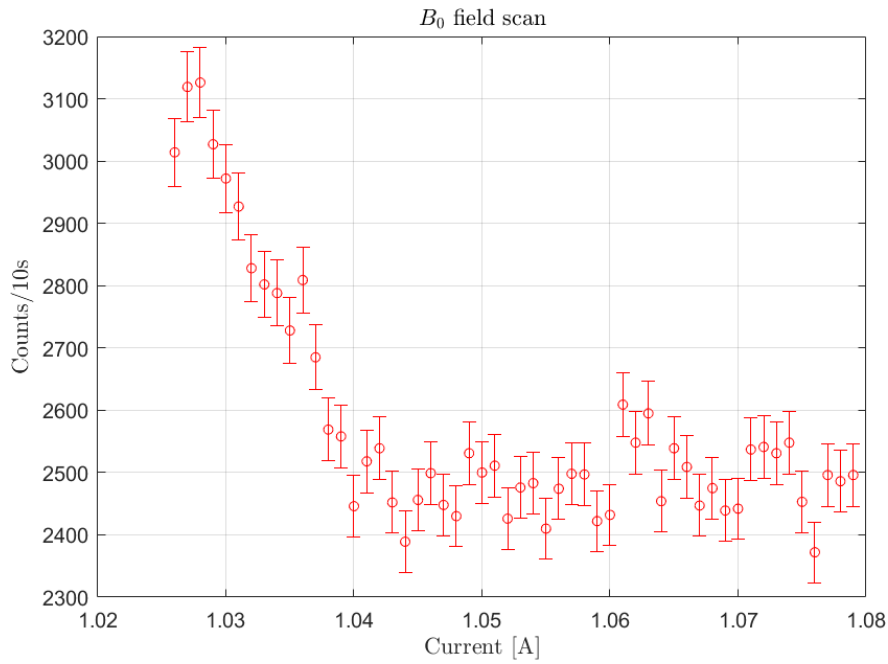


Figure 5.19: Scan of the  $B_0$  field with an active gradient of  $I_{GR} = 0.92$  A and an RF amplitude corresponding to 440 mVpp. The intensity minimum found in the gradient scan ( $I_{min} = 2351/10s$ ) could not be further reduced.

setup), covering the window at the side of the beamport, covering the window at the side of the second supermirror and covering both windows. The results are summarized in table (5.4). The intensity without flipping  $I_{max}$  is not influenced by the aluminium foil, contrary to the intensity with flipping  $I_{min}$ , which is decreased when applying foil.

	$I_{max}$ [s <sup>-1</sup> ]	$I_{min}$ [s <sup>-1</sup> ]	$I_{GR}$ [A]	flip efficiency
No aluminium foil	3413	240	0.98	0.8684 (18)
aluminium foil (beamport)	3423	191	0.96	0.8945 (17)
aluminium foil (supermirror)	3452	220	1	0.8791 (18)
both sides aluminium foil	3409	183	0.94	0.8986 (17)

Table 5.4: Tests of setups with different aluminium foil covering at an RF field strength corresponding to 440 mVpp ( $P_f/P_r = 133/3$ ). The intensity  $I_{max}$  does not change, indicating no absorption by the foil. The best results were obtained by covering both sides of the flipper, whereby foil at the beamport window proves to be more effective than on the side of the supermirror. Due to different positions of detector and supermirror, these measurements are only comparable among themselves and to figure (5.19).

Most effective is the covering of the beamport window and the highest flip efficiency was achieved by covering both sides, where the efficiency could be increased significantly by  $0.8986 (17) - 0.8684 (18) = 0.0302 (25)$ , compared to the measurement without any aluminium foil.

### 5.3 Discussion

After challenges with the high power demand at the load and the resulting short circuits the frequency was reduced from 4 MHz to 1 MHz and several changes were made to the dimension and material of the flipper. As a result it became possible to operate the flipper at high powers but only for short time periods. At 640 mVpp ( $P_f/P_r = 315/10$ ) the total measurement time numbered 200 s. Furthermore, the reduced frequency means a shorter spin echo length (see equation (3.41)). It decreases from  $\delta_{NSE} = 0.91 \mu\text{m}$  at 4 MHz to  $\delta_{NSE} = 0.267 \mu\text{m}$  at 1 MHz. This is still larger than the transversal coherence length of  $\sigma_T = 88 \text{ nm}$ , but one loses flexibility and becomes more vulnerable to uncertainties.

Scans of the amplitude  $B_1$  and the strong static field  $B_0$  with active gradients indicate that the procedure of  $B_0$ -scan (finding the freq. resonance) followed by scans of the gradient field at different amplitudes  $B_1$  is valid to determine the optimal flip efficiency achievable with these parameters at the setup. Such gradient field scans show that the current  $I_{GR}$  required to find the minimum intensity is increasing with the amplitude  $B_1$ . This is due to the requirement  $B_1/2 = B_{GR}$ , at which point the highest possible flip efficiency is found for a given RF field. Moreover, the flip efficiency could be elevated by stronger RF fields, which is increasing the adiabaticity parameter  $k$  and by utilising cadmium shielding. The latter absorbs all neutrons, which will not go through the flipper and therefore reduces the count rate of not properly flipped neutrons. This enhances

the flip efficiency by 0.0252 (34), when measured at 350 mVpp ( $P_f/P_r = 77/1$ ). The disadvantage is that the overall intensity is lowered, resulting in poorer statistical precision. This can be compensated by longer measurement times. The highest efficiency of  $\epsilon = 0.9231$  (15) was obtained at 640 mVpp ( $P_f/P_r = 309/11$ ) and  $I_{GR} = 1.88$  A. Measurements at higher powers could not be carried out due to heat-related problems and even RF amplitudes corresponding to 640 mVpp are not suitable for long-time operations of several hours. Furthermore, a flip efficiency of  $\epsilon = 0.9231$  of one adiabatic RF flipper is not sufficient if seen in the context of the entire SESANS experiment. Since four such flippers have to be implemented, the overall flip efficiency of the entire setup will be  $(0.9231)^4 = 0.7261$ . In order to achieve an overall efficiency of 0.9 one individual flipper must reach an efficiency of  $\sqrt[4]{0.9} = 0.9740$ . Lastly, it could be shown that the flip efficiency could be increased by adding aluminium foil, which ensures that the RF field is confined to the same area as the  $B_0$  field and the pole shoes. This increased the efficiency by 0.0302 (25) at 440 mVpp ( $P_f/P_r = 133/3$ ).

There are several reasons for the discrepancy between the theoretically calculated flip efficiency and the experimental data. The theoretical derivation assumes a cosine-shape gradient and a sinusoidal RF amplitude. In practice, we only have the best approximation to these shapes. In addition, the gradient along the flight direction is most likely different for different trajectories through the flipper, since the gradient coil is not in Helmholtz configuration. Therefore, the condition  $B_{GR} = B_1/2$  is not fulfilled for all neutrons in the flipper. Moreover, the power displayed at the RF amplifier is not equal to power at the load. The amplifier displays the power provided for the entire circuit. Due to additional losses in the circuit, part of this power is dissipated as heat or irradiated. Hence, the power at the load will be lower than displayed. Another reason is the rather low degree of polarization of 0.9, which is affecting the intensity measurements with supermirrors and therefore the determination of the flip efficiency.

# Chapter 6

## Outlook

This section is intended to provide an outlook on the next steps in the development of the adiabatic RF flipper. In order to achieve higher flip efficiencies the most reasonable approach is to increase the adiabaticity parameter  $k$ . This can be done by decreasing the velocity of the neutrons  $v$  or by increasing the length of the flipper  $L$  or the RF amplitude  $B_1$ . The first parameter can only be changed by rotating the supermirror inside the concrete shielding and therefore changing the grazing angle and the spectrum of the reflected and polarized neutron beam. Half the velocity of the fastest neutrons is approximately doubling  $k$ . From the TOF measurements of the spectrum (figure 5.2) one can see that the intensity at 6 Å is already insufficient. Therefore a significant decrease of  $v$  is not possible. To extend the region of the magnetic field  $L$  the pole shoes would have to be replaced by larger ones. Since  $k$  is linear in  $L$ , a doubling will yield  $2k$ . Due to the limited space at the experimental site this can not be done and would leave too little space for zero field precession between the flippers. This leaves the enhancement of the RF amplitude  $B_1$  and consequently the gradient field  $B_{GR}$ . The major problem at higher electrical powers in the coils is heat production. Cooling the wire will not only battle the aforementioned problem but would also reduce the resistance of the load and therefore the power demand. Another advantage of cooled RF coils is the possibility of ensuring long-time operation with stable magnetic fields.

The first idea to implement cooling with liquid nitrogen failed, because of the limited space in the aluminium box. It was not possible to pull a cylindrical storage for liquid nitrogen over the RF coil and add connectors for a cooling loop. A more elegant but not as effective solution is the usage of a copper tube as depicted in figure (6.1). A similar approach was utilized in [Plo09]. Its outside diameter is 2 mm and the inside diameter 1 mm. This tube is functioning as the RF coil and is part of the cooling system simultaneously. The cooling liquid is running through the inside, whereas the electrical current is transported in the copper. The reduced cross section area of the wire will not affect the resistance severely, since the skin depth at 1 MHz is 0.066 mm. Thus, most of the current is transported near the outer surface of the wire anyway.





Figure 6.1: Copper tube functioning as RF coil. Its outside diameter is 2 mm and the inside diameter 1 mm. Adapters for the water cooling circuit are welded onto the ends of the coil and are applicable for tubes with an outside diameter of 8 mm and an inside diameter of 5 mm. Connections for the electrical circuit have not yet been implemented.

For test purposes water was chosen as cooling medium, which is pumped by a **R**xylem Flojet Series R3811. This pump can deliver pressures up to 10 bar. Since the tube leading from the pump to the copper tube have an inner diameter of 5 mm, a high pressure builds up at the connection to the thinner copper pipe. Thus an overpressure valve must be installed in order to keep the pump running smoothly. With this setup a flow rate of about 250 mL/min was obtained. One needs to keep in mind the adequate scaling of the magnetic gradient field and the current in the coil, when increasing the RF amplitude. Moreover, an alternative to flip the spin by  $\pi$  it is possible to induce zero field precession by a  $\pi/2$  rotation. This also reduces the power requirements of the flipper, but has the drawback of halving the precession frequency, which reduces sensitivity of the SESANS instrument.

# Chapter 7

## Conclusion

The first neutron spin flipping approach requires an option for time-of-flight measurements. In order to obtain a pulsed neutron beam, the supermirror of the spin chopping system has to be flipped with respect to the polariser. The frequency of the RF flipper was set to  $f = 3.910933$  MHz. TOF measurements with different pulse durations and currents all yielded SNR values below 2 for all wavelengths. Measurements of the intensity with and without a field stepper showed that unwanted adiabatic magnetic field transitions between the two supermirrors were the major cause for low SNR values. Furthermore, it was not possible to generate a step in the magnetic field strong enough to increase the SNR significantly. The maximum SNR value of  $2.08 \pm 0.2$  at  $4.19 \text{ \AA}$  was obtained with  $t_p = 30$  cycles,  $V_{p-p} = 1.7 \text{ V}$  and  $t_f = 3.03 \text{ ms}$ .

The second approach for broadband spin flipping was utilizing an adiabatic RF flipper. In order to effectively flip spins of a white beam a high adiabaticity parameter  $k$  and thus strong RF amplitudes and gradients are necessary. A gradient coil was designed that is able to induce a magnetic field of  $B_{GR} = 2.52$  at  $I_{GR} = 1.8 \text{ A}$ , which proved to be just sufficient. More current in the gradient coil is not suitable for long term operation. Due to the high current demand at the RF flipper, it was not possible to put a device into operation at  $f = 4 \text{ MHz}$ . Problems were unwanted shorts between the wire and ground as well as heat generation. Hence, the frequency was lowered to  $f = 1 \text{ MHz}$ , which allowed for measurements to test the performance of the adiabatic RF flipper. Scans of the gradient field for different RF amplitudes at frequency resonance proved to be an appropriate procedure to determine the flip efficiency experimentally. Moreover, the performance of the flipper could be increased with cadmium shielding and aluminium foil by 0.0252 (34) and 0.0302 (25), respectively. The highest efficiency of  $\epsilon = 0.9231$  (15) was obtained at  $640 \text{ mVpp}$  ( $P_f/P_r = 309/11$ ) and  $I_{GR} = 1.88 \text{ A}$ . The efficiency may be improved by increasing the adiabaticity parameter, but this leads to an increase in power that was not possible to achieve with the present setup. The major limiting factor is the heat generation at the flipper and the cables. This problem is addressed by implementing a cooling system, that not only aims to increase the

maximal possible current in the coil but also aims to ensure stable long-term operation at high powers. First tests to run water through a copper tube for cooling while also using it as RF coil have already been conducted.

# Bibliography

- [ABR81] B. Alefeld, G. Badurek and H. Rauch. “Observation of the neutron magnetic resonance energy shift”. In: *Zeitschrift für Physik B Condensed Matter* 41 (1981). DOI: <https://doi.org/10.1007/BF01294428>.
- [Bak+11] C.A. Baker et al. “The search for the neutron electric dipole moment at the Paul Scherrer Institute”. In: *Physics Procedia* 17 (2011). 2nd International Workshop on the Physics of fundamental Symmetries and Interactions - PSI2010, pp. 159–167. ISSN: 1875-3892. DOI: <https://doi.org/10.1016/j.phpro.2011.06.032>.
- [Bal90] L.E. Ballentine. *Quantum Mechanics*. Prentice-Hall, 1990. ISBN: 0137479328.
- [Brü05] Thomas Brückel. *Neutron scattering: lectures of the laboratory course held at the Forschungszentrum Jülich*. eng. Schriften des Forschungszentrums Jülich : Reihe Materie und Material. Jülich: Forschungszentrum, 2005. ISBN: 3893363955.
- [BS40] F. Bloch and A. Siegert. “Magnetic Resonance for Nonrotating Fields”. In: *Phys. Rev.* 57.6 (Mar. 1940), pp. 522–527. DOI: 10.1103/PhysRev.57.522.
- [Cha32] J. Chadwick. “Possible Existence of a Neutron”. In: *Nature* 129 (1932), p. 312.
- [Col15] Ian R. Cole. “Modelling CPV”. PhD thesis. Loughborough University, June 2015. URL: [https://repository.lboro.ac.uk/articles/thesis/Modelling\\_CPV/9523520](https://repository.lboro.ac.uk/articles/thesis/Modelling_CPV/9523520).
- [Coo14] Jeremy C Cook. “Concepts and Engineering Aspects of a Neutron Resonance Spin-Echo Spectrometer for the National Institute of Standards and Technology Center for Neutron Research”. In: *Journal of research of the National Institute of Standards and Technology* 119 (2014). DOI: 10.6028/jres.119.005.
- [Dem08] W. Demtröder. *Experimentalphysik 2*. German. Springer Berlin Heidelberg, 2008. ISBN: 9783540682196.
- [Dem10] W. Demtröder. *Experimentalphysik 3*. German. 3rd ed. Springer Berlin Heidelberg, 2010. ISBN: 978-3-642-03910-2.

- [Dem13] Bülent Demirel. “Spin-rotation-coupling in neutron polarimetry”. Master’s Thesis. TU Wien, 2013.
- [Gäh+96] R. Gähler et al. “Space-time description of neutron spin echo spectrometry”. In: *Physica B: Condensed Matter* 229.1 (1996), pp. 1–17. DOI: [https://doi.org/10.1016/S0921-4526\(96\)00509-1](https://doi.org/10.1016/S0921-4526(96)00509-1).
- [Gee+19] N. Geerits et al. “Applying Resonant Spin Flippers with Poleshoes and Longitudinal Radio Frequency Fields to Time of Flight MIEZE”. In: *Journal of Physics: Conference Series* 1316.1 (Oct. 2019), p. 012011. DOI: [10.1088/1742-6596/1316/1/012011](https://doi.org/10.1088/1742-6596/1316/1/012011).
- [GG87] R. Gähler and R. Golub. “A high resolution neutron spectrometer for quasielastic scattering on the basis of spin-echo and magnetic resonance”. In: *Zeitschrift für Physik B Condensed Matter* 65 (1987).
- [GGK94] R. Golub, R. Gähler and T. Keller. “A plane wave approach to particle beam magnetic resonance”. In: *American Journal of Physics* 62.9 (1994), pp. 779–788. DOI: <https://doi.org/10.1119/1.17459>.
- [GOR97] S.V Grigoriev, A.I Okorokov and V.V Runov. “Peculiarities of the construction and application of a broadband adiabatic flipper of cold neutrons”. In: *Nuclear Instruments and Methods in Physics Research Section A: Accelerators, Spectrometers, Detectors and Associated Equipment* 384.2 (1997), pp. 451–456. ISSN: 0168-9002. DOI: [https://doi.org/10.1016/S0168-9002\(96\)00919-9](https://doi.org/10.1016/S0168-9002(96)00919-9).
- [Has+10] Yuji Hasegawa et al. “Engineering of triply entangled states in a single-neutron system”. In: *Physical Review A* 81.3 (Mar. 2010). DOI: [10.1103/physreva.81.032121](https://doi.org/10.1103/physreva.81.032121).
- [HR06] S. Haroche and J.M. Raimond. *Exploring the Quantum*. Ed. by S. Haroche and J.M. Raimond. Oxford University Press, Oxford. 2006.
- [Ima11] Toyoko Imae. *Neutrons in soft matter*. Hoboken, N.J.: J. Wiley, 2011. ISBN: 1283175258.
- [Kel+95] Thomas Keller et al. “Features and performance of an NRSE spectrometer at BENSC”. In: *Neutron News* 6 (1995), pp. 16–17.
- [Kno89] Glenn F Knoll. *Radiation detection and measurement*. 2. ed. New York, NY: Wiley, 1989. ISBN: 0471815047.
- [Kra+01] W.H. Kraan et al. “Zero-field precession induced by adiabatic RF spin flippers”. In: *Physica B: Condensed Matter* 297.1 (2001). Proceeding of the Third International Workshop on Polarised Neutrons, pp. 23–27. ISSN: 0921-4526. DOI: [https://doi.org/10.1016/S0921-4526\(00\)00832-2](https://doi.org/10.1016/S0921-4526(00)00832-2).

- [Kra+03] Wicher H. Kraan et al. “Test of adiabatic spin flippers for application at pulsed neutron sources”. In: *Nuclear Instruments & Methods in Physics Research Section A-accelerators Spectrometers Detectors and Associated Equipment* 510 (2003), pp. 334–345.
- [Kra04] Wicher Hooite Kraan. “Instrumentation to handle thermal polarized neutron beams”. PhD thesis. TU Delft, 2004.
- [KRP91] W.H. Kraan, M.Th. Rekveldt and P.T. Por. “Adiabatic rotators for 3-D neutron polarisation analysis”. In: *Nuclear Instruments and Methods in Physics Research Section A: Accelerators, Spectrometers, Detectors and Associated Equipment* 300.1 (1991), pp. 35–42. DOI: [https://doi.org/10.1016/0168-9002\(91\)90703-S](https://doi.org/10.1016/0168-9002(91)90703-S).
- [Lau] Institut Laue-Langevin. *IN15 Spin-echo spectrometer with time-of-flight option and focusing option*. URL: <https://www.ill.eu/users/instruments/instruments-list/in15/characteristics> (visited on 15/03/2023).
- [LT08] Shuangzhe Liu and Otz Trenkler. “Hadamard, Khatri-Rao, Kronecker and other matrix products”. In: *International Journal of Information and Systems Sciences* 4 (Jan. 2008).
- [Mac18] Wilfried Mach. “Installation of a neutron beam instrument at the TRIGA reactor in Vienna”. PhD thesis. Wien: TU Wien, 2018.
- [Mar+03] R. Maruyama et al. “A resonance neutron-spin flipper for neutron spin echo at pulsed sources”. In: *Physica B: Condensed Matter* 335.1 (2003). Proceedings of the Fourth International Workshop on Polarised Neutrons for Condensed Matter Investigations, pp. 238–242. ISSN: 0921-4526. DOI: [https://doi.org/10.1016/S0921-4526\(03\)00246-1](https://doi.org/10.1016/S0921-4526(03)00246-1).
- [Mez72] F. Mezei. “Neutron spin echo: A new concept in polarized thermal neutron techniques”. In: *Zeitschrift für Physik A Hadrons and nuclei* 255 (1972). DOI: 10.1007/BF01394523.
- [Mez76] F. Mezei. “Novel polarized neutron devices: supermirror and spin component amplifier”. In: *Communications on Physics* 1 (3 Jan. 1976).
- [Mez77] F. Mezei. “Corrigendum and first experimental evidence on neutron supermirrors”. In: *Communications on Physics* 2 (1977).
- [Mez80] Ferenc Mezei. *Neutron spin echo : proceedings of a Laue-Langevin Inst. workshop, Grenoble, October 15 - 16, 1979*. Lecture notes in physics. Berlin [u.a.]: Springer, 1980. ISBN: 0387100040.
- [Mez88] F. Mezei. “Zeeman energy, interference and Neutron Spin Echo: A minimal theory”. In: *Physica B+C* 151.1 (1988), pp. 74–81. ISSN: 0378-4363. DOI: [https://doi.org/10.1016/0378-4363\(88\)90148-9](https://doi.org/10.1016/0378-4363(88)90148-9).

- [Plo09] Jeroen Plomp. “Spin-echo development for a time-of-flight neutron reflectometer”. PhD thesis. TU Delft, 2009.
- [Rek+05] M. Theo Rekveldt et al. “Spin-echo small angle neutron scattering in Delft”. In: *Review of Scientific Instruments* 76.3 (2005), p. 033901. DOI: [10.1063/1.1858579](https://doi.org/10.1063/1.1858579).
- [Rek96] M.Theo Rekveldt. “Novel SANS instrument using Neutron Spin Echo”. In: *Nuclear Instruments and Methods in Physics Research Section B: Beam Interactions with Materials and Atoms* 114.3 (1996), pp. 366–370. DOI: [https://doi.org/10.1016/0168-583X\(96\)00213-3](https://doi.org/10.1016/0168-583X(96)00213-3).
- [RW15] H. Rauch and S. A. Werner. *Neutron Interferometry*. Clarendon Press, Oxford, 2015. ISBN: 978-0-19-871251-0.
- [Sch07] Franz Schwabl. *Quantenmechanik*. German. Springer Berlin, Heidelberg, 2007. ISBN: 978-3-540-73674-5.
- [Sea86] V.F. Sears. “Electromagnetic neutron-atom interactions”. In: *Physics Reports* 141.5 (1986), pp. 281–317. ISSN: 0370-1573. DOI: [https://doi.org/10.1016/0370-1573\(86\)90129-8](https://doi.org/10.1016/0370-1573(86)90129-8).
- [Spo+08] S. Sponar et al. “Zero-field and Larmor spinor precessions in a neutron polarimeter experiment”. In: *Physics Letters A* 372.18 (2008), pp. 3153–3156. DOI: <https://doi.org/10.1016/j.physleta.2008.01.070>.
- [Spo+10] S. Sponar et al. “Violation of a Bell-like inequality for spin-energy entanglement in neutron polarimetry”. In: *Physics Letters A* 374.3 (2010), pp. 431–434. DOI: <https://doi.org/10.1016/j.physleta.2009.11.017>.
- [Spo+12] S Sponar et al. “High-efficiency manipulations of triply entangled states in neutron polarimetry”. In: *New Journal of Physics* 14.5 (May 2012). DOI: [10.1088/1367-2630/14/5/053032](https://doi.org/10.1088/1367-2630/14/5/053032).
- [Sud05] Martin Suda. *Quantum Interferometry in Phase Space*. Springer Berlin, Heidelberg, 2005. ISBN: 978-3-540-26070-7.
- [Tak+11] K. Taketani et al. “A high S/N ratio spin flip chopper system for a pulsed neutron source”. In: *Nuclear Instruments and Methods in Physics Research Section A: Accelerators, Spectrometers, Detectors and Associated Equipment* 634.1 (2011). Proceedings of the International Workshop on Neutron Optics NOP2010, S134–S137. DOI: <https://doi.org/10.1016/j.nima.2010.06.357>.
- [UI10] Masahiko Utsuro and Vladimir K. Ignatovich. *Neutron Optics*. John Wiley and Sons, Ltd, 2010. ISBN: 978-3-527-40885-6.

- [Van54] Léon Van Hove. “Correlations in Space and Time and Born Approximation Scattering in Systems of Interacting Particles”. In: *Phys. Rev.* 95 (1 July 1954), pp. 249–262. DOI: 10.1103/PhysRev.95.249.
- [Wie20] TU Wien. *Der TRIGA Mark-II Reaktor*. German. 2020. URL: <https://www.tuwien.at/trigacenter/trigareaktor> (visited on 05/01/2023).
- [YuV75] Taran Yu.V. “Fast Adiabatic Neutron Spin Flip”. In: *Dubna Report JINR P3-8577* (1975).